THE UNIVERSITY OF QUEENSLAND

AUSTRALIA

Exploring the utility of GRE-MRI signal compartments for temporal susceptibility mapping and investigation of neural microstructure

Shrinath Kadamangudi

B.Sc. Neuroscience

A thesis submitted for the degree of Master of Philosophy at

The University of Queensland in 2017

Queensland Brain Institute

Centre for Advanced Imaging

Abstract

Magnetic resonance imaging (MRI) has played a key role in our understanding of the brain's anatomy and physiology. In particular, gradient recalled echo magnetic resonance imaging (GRE-MRI) at ultra-high field holds great promise for new contrast mechanisms to examine brain structure non-invasively. Multi-echo GRE-MRI is affected by signal compartments which may inform structural characterization. A number of studies have adopted the three water-pool compartment model to study white matter brain regions by associating individual compartments with myelin, axonal and extracellular water. Many key questions, however, remain unanswered in the context of GRE-MRI signal compartmentalization.

First, the number and identifiability of GRE-MRI signal compartments has not been fully explored. We examined these issues in the human brain using a data driven approach, as detailed in Ch. 1. Multiple echo time GRE-MRI data were acquired in five healthy participants, each brain was segmented into anatomical regions (substantia nigra, caudate, insula, putamen, thalamus, fornix, internal capsule, corpus callosum and cerebrospinal fluid) and the temporal signal fitted with models with one to six signal compartments. With the use of information criteria and cluster analysis methods we ascertained the number of distinct signal compartments within each region and established differences in their respective frequency shifts between the brain regions studied. We identified five dominant signal compartments; these contributed to the local signal frequency of each brain region differently. Maps of compartment volume fractions, resolved by fixing the respective compartment frequency shifts in each voxel, corresponded with commonly observed tissue properties.

Second, the influence of the scanner field strength on the temporal evolution of the multi-echo GRE-MRI signal is not known. Subsequently, the influence of scanner field strength on GRE-MRI signal compartments also remains uncharacterized. In Ch. 3, we evaluated variations in the signal frequency shifts due to changes in field strength within the putamen, CSF, and corpus callosum (representatives of gray matter, CSF, and white mater regions respectively). Multiple echo time GRE-MRI data at 3T and 7T were acquired in six healthy participants, and temporal frequency shift profiles were generated via the quantitative susceptibility pipeline. From a qualitative lens, we observed unique echo-time dependent frequency shift profiles for each brain region to broadly correspond between 3T and 7T measurements. Furthermore, inter-participant variability in frequency shifts were higher in

3T measurements than at 7T. In general, signal compartment frequency shifts correspond well between 3T and 7T data, and standard error estimates indicate an improved quality-of-fit within the putamen and CSF, when compared to the corpus callosum. Compartment frequency shifts mapped using multi-echo GRE-MRI signal compartment models may thus provide new insights into tissue composition and structure, holding particular value in generating biomarkers for neurodegenerative diseases and psychiatric disorders.

Declaration by author

This thesis is composed of my original work, and contains no material previously published or written by another person except where due reference has been made in the text. I have clearly stated the contribution by others to jointly-authored works that I have included in my thesis.

I have clearly stated the contribution of others to my thesis as a whole, including statistical assistance, survey design, data analysis, significant technical procedures, professional editorial advice, financial support and any other original research work used or reported in my thesis. The content of my thesis is the result of work I have carried out since the commencement of my higher degree by research candidature and does not include a substantial part of work that has been submitted to qualify for the award of any other degree or diploma in any university or other tertiary institution. I have clearly stated which parts of my thesis, if any, have been submitted to qualify for another award.

I acknowledge that an electronic copy of my thesis must be lodged with the University Library and, subject to the policy and procedures of The University of Queensland, the thesis be made available for research and study in accordance with the Copyright Act 1968 unless a period of embargo has been approved by the Dean of the Graduate School.

I acknowledge that copyright of all material contained in my thesis resides with the copyright holder(s) of that material. Where appropriate I have obtained copyright permission from the copyright holder to reproduce material in this thesis and have sought permission from co-authors for any jointly authored works included in the thesis.

Publications during candidature

Kadamangudi, S., Reutens, D., Sood, S., Vegh, V., 2017. Discrete frequency shifts explain GRE-MRI signal compartments., in Proc., ISMRM, 25th Annual Meeting and Exhibition, Honolulu, HI. Poster 3671.

Publications included in this thesis

Kadamangudi et al., 2017 – content form material and methods, and results incorporated within Ch. 3.

Contributor	Statement of contribution
Shrinath Kadamangudi	Conception and design (50%) Analysis and interpretation (60%) Drafting and production (60%)
Surabhi Sood	Conception and design (0%) Analysis and interpretation (20%) Drafting and production (0%)
David Reutens	Conception and design (10%) Analysis and interpretation (0%) Drafting and production (20%)
Viktor Vegh	Conception and design (40%) Analysis and interpretation (20%) Drafting and production (20%)

Manuscripts included in this thesis

Title: Signal compartments in ultra-high field multi-echo gradient echo MRI reflect underlying tissue microstructure in the brain. Submitted to Neuroimage (Elsevier; currently under review.

Contributor	Statement of contribution
Shrinath Kadamangudi	Conception and design (50%) Analysis and interpretation (60%) Drafting and production (60%)
Surabhi Sood	Conception and design (0%) Analysis and interpretation (20%) Drafting and production (0%)

David Reutens	Conception and design (10%) Analysis and interpretation (0%) Drafting and production (20%)
Viktor Vegh	Conception and design (40%) Analysis and interpretation (20%) Drafting and production (20%)

Contributions to others to this thesis

For the work contained in Ch. 2, data collection, signal pre-processing and quantitative susceptibility mapping were performed by Mrs. Surabhi Sood. Signal compartmentalization, model selection, and all further data analyses were performed by Mr. Shrinath Kadamangudi. The core interpretation of results and drafting were performed by Mr. Kadamangudi; assistance in interpretation of results, as well as drafting and editing were provided by Dr. Vegh and Dr. Reutens. *Note:* The content of this chapter was presented in the poster session for the International Society for Magnetic Resonance in Medicine (ISMRM) 2017 (Honolulu, HI, USA) meeting, and is currently in preparation for journal publication.

For the work contained in Ch. 3, data collection, signal pre-processing and quantitative susceptibility mapping were performed by Mrs. Sood. Signal compartmentalization and all further data analyses were performed by Mr. Kadamangudi. The core interpretation of results and drafting were performed by Mr. Kadamangudi; Mrs. Sood assisted in generating tables and figures, as well as drafting components of the introduction. Assistance in interpretation of results, as well as drafting and editing were also provided by Dr. Vegh and Dr. Reutens. *Note:* The content of this chapter has been submitted as an abstract for the International Society for Magnetic Resonance in Medicine (ISMRM) 2018 (Paris, FR) meeting, and is in preparation for journal publication.

Editing assistance was provided by Dr. Vegh for Chapters 1 and 4.

Statement of parts of the thesis submitted to qualify for the award of another degree

None.

Research involving human or animal subjects

The experiment was conducted after having been provided ethical clearance by the University of Queensland human ethics committee. Ethics approval number: 2015000838. Ethics approval form is provided in the Appendix section.

Acknowledgements

The authors extend their gratitude to Javier Urriola, Aiman Al-Najjar and Nicole Atcheson for assitance in data collection. We also sincerely thank Dr. Markus Barth for insightful discussions and Dr. Reza Bonyadi for providing key technical insights throughout the duration of both projects.

Financial support

Shrinath Kadamangudi received the University of Queensland International Scholarship MPhil scholarship, awarded by the Queensland Brain Institute, for this work. Viktor Vegh and David Reutens acknowledge the funding received from the Australian Research Council (DP140103593) in support of this project and from the National Health and Medical Research Council (AP1104933) in support of this project.

Key words

Magnetic Resonance Imaging (MRI), ultra-high field, gradient recalled echo (GRE) MRI, signal compartments, frequency shift, quantitative susceptibility mapping, tissue microstructure.

Australian and New Zealand Standard Research Classifications (ANZSRC)

1. ANZSRC code: 100402, Medical Biotechnology Diagnostics (50%)
2. ANZSRC code: 110903, Central Nervous System (30%)
3. ANZSRC code: 010406, Stochastic Analysis and Modelling (20%)3

Fields of Research (FoR) Classification

1. FoR code 1004, Medical Biotechnology (50%)
2. FoR code 1109, Neurosciences (30%)
3. FoR code: 0104, Statistics (20%)

Table of Contents

List of Abbreviations

GRE-MRI – Gradient recalled echo magnetic resonance imaging.

mGRE-MRI – multi-echo GRE-MRI.

MRI – Magnetic resonance imaging.

MWF – Myelin water fraction (imaging).

NMV – Net magnetization vector.

QSM – Quantitative susceptibility mapping.

T_1 – Spin-lattice (longitudinal) relaxation time constant.

T_2 – Spin-spin (transverse) relaxation time constant.

T_2' – A constant that describes the loss of transverse magnetization due to static magnetic field inhomogeneities.

T_2^* – Loss of transverse magnetization due to spin-spin relaxation and static magnetic field inhomogeneities.

Chapter 1: Background

1.1 Principles of signal behaviour in magnetic resonance imaging

1.1.1 Nuclear induction/magnetization & classical theory of relaxation in ^{1}H-nuclear magnetic resonance

Magnetic resonance imaging (MRI) allows for non-invasive imaging of tissue structure and quantification of tissue functions by exploiting the ^{1}H-proton nuclear magnetic resonance technique (^{1}H-NMR)[a] (Damadian, 1971; Lauterbur, 1973). The ^{1}H-NMR signal is generated from the nuclear motion of spinning protium (^{1}H) hydrogen nuclei (Bloch, 1946). The nuclear magnetic moment for the protium nucleus, and all other atomic nuclei, is governed by the spin state, or quantum angular momentum, of the atom's constitutive subatomic particles (e.g. protons and neutrons) (Rabi et al., 1934). In the presence of an external (artificially or naturally generated) magnetic field, the nanoscopic magnetic moments of protium nuclei experience a torque in the plane orthogonal to the external magnetic field direction (Bloch, 1946). In MRI, the primary external magnetic field is generated by a loop of current carried by superconducting metals and is commonly referred to as the B_0 field, or simply B_0. The frequency at which protium nuclei spin, or precess[b], about the external magnetic is linearly dependent on B_0 and gyromagnetic ratio[c] (γ); this fixed value is referred to as the Larmor frequency, denoted by the greek letter ω, and is described by the Larmor equation, $\omega_0 = \gamma B_0$ (Hahn, 1950; Lodge, 1897; Rabi, 1937). The

---

[a] The quantum principles (e.g. atomic mechanics, wave-particle properties, energy transition states, etc.) which underlie the nuclear magnetic resonance phenomenon reside outside the focus of the current work, thus will not be detailed; information regarding the quantum theory of NMR can be found within the relevant literature (Abragam, 1961; Hahn and Abragam, 1992; Poole, 2012; Slichter, 2013; White, 2013). Rather, a brief classical description of nuclear induction (generally referred to as nuclear magnetization) and the magnetic relaxation process will be provided to aid in contextualizing pertinent MRI signal behaviour in following sections.

[b] Adapted from the description contextualized using classical mechanics; a magnetic moment spinning as a top about a fixed axis (Levitt, 2001).

[c] A constant value, defined as the ratio of the magnetic moment magnitude to the angular momentum (Driscoll and Bender, 1958).

Larmor equation is a foundational concept in MRI and will be further discussed within different contexts throughout this work.

The nanoscopic magnetic moments are prevented from aligning fully to the external magnetic field, and terminating quantum precession, due to the interference of thermal energy (Bloch, 1946). This phenomenon permits the magnetic moments to assume only two possible alignments (also referred to as quantum spin states) with respect to the external magnetic; parallel or anti-parallel. If the protium nuclei were evenly distributed between the parallel and anti-parallel spin states, the net magnetic moments would effectively cancel. However, the thermal energy experienced by spins aligned parallel are notably higher than those aligned anti-parallel (Abragam, 1961). Consequently, a net 'excess' of magnetic moments precess in the parallel spin state in comparison to those aligned anti-parallel (Bloch, 1946). It is this net excess of mechanically active spins that form a detectable MRI signal.

The net excess of protium spin populations, however, exist in extremely sparse quantities (add value), and in its own accord does not guarantee a detectable MRI signal (even in macroscopic bodies). To compensate for this, energy in the form radiofrequency (r-f) waves is deposited into the system (or sample of interest), consequently inducing additional precession of the atomic nuclei (tipping the spins into an 'excited' state) around B_0. The r-f waves are merely magnetic fields which alternate in polarity; thus they are referred to commonly in MRI literature as the B_1 field (Hill and Richards, 1968). Importantly, the polarity of the magnetic fields must oscillate at the Larmor frequency in order to interact with and excite spin populations at equilibrium. As mentioned earlier, the Larmor frequency for protium nuclei is solely governed by the magnetic field strength. Thus, by manipulating the magnetic field strength at various spatial location, specific populations of protium nuclei within a sample (or tissue) of interest are excited. To achieve this, additional magnetic fields, known as gradient magnetic fields, are applied in conjunction with the main magnetic field

(B_0) to induce spatial variation in the magnetic field strength (Lauterbur, 1973); in this way, the magnetic properties of tissue are measured, encoded and used to form an image in a highly specific and targeted manner.

An over population of protium spin populations (precessing specifically at the Larmor frequency) in the excited state initiates a net (or bulk) magnetic signal (formally referred to as the net magnetization vector); this temporally oscillating bulk magnetic moment induces a changing voltage and induces a current within electro-sensitive receiver coils (Bloch, 1946). This process was coined by Bloch (1946) as nuclear induction. After switching off the B_1 field, these excited protium spin populations equilibrate back to their 'normal' energetic state and discharge energy out of the system, resulting in the net magnetization vector to also diminish simultaneously; in NMR and MRI literature, this process is referred to as 'relaxation'(Bloch, 1957). In simpler terms, in the absence of the B_1 field, the bulk magnetization vector produced by protium spin populations relax back towards the direction of B_0. As the name suggests, the net magnetization vector can be characterized and measured according to its vector components; a longitudinal and transverse component (Abragam, 1961). The longitudinal magnetization represents the net magnetization along the direction of B_0 (along the z-axis in Fig. 1A and B), whereas the transverse magnetization represents the net magnetization orthogonal to both the longitudinal magnetization and B_0 (along the x-axis in Fig. 1A and B).

After exciting the spin populations and transferring the net magnetization vector from the longitudinal to transverse position, the net magnetization relaxes back towards the longitudinal position over a specific time interval. This relaxation process is commonly modelled as a first-order exponential decay, introduced by Bloch (1946), and is referred to as

T_1 (or spin-lattice[d]) relaxation (Fig. 1A) (Bloch, 1946). Conversely, a time dependent relaxation, or loss, of the transverse magnetization is referred to as T_2 (or spin-spin[e]) relaxation (Fig. 1B).

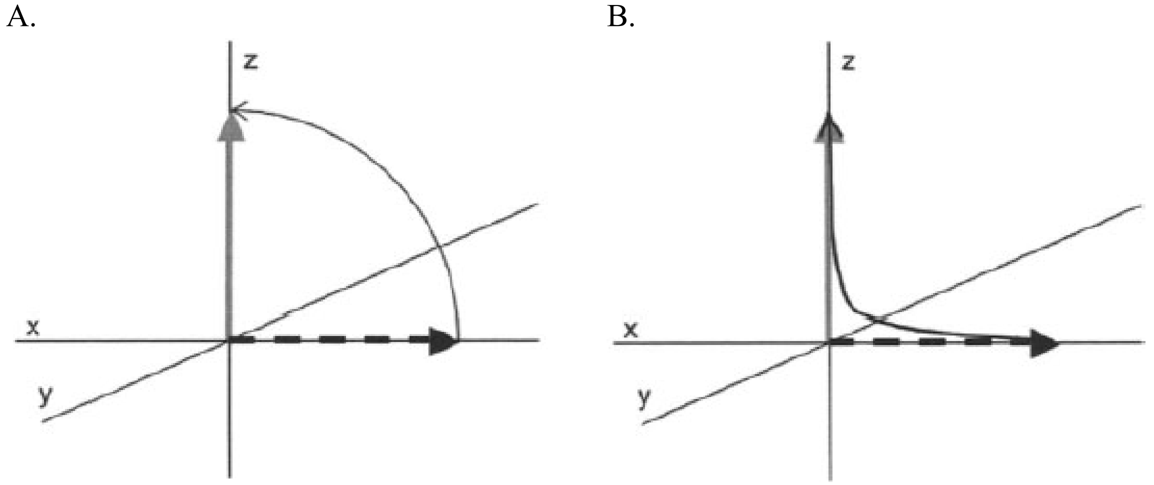

Fig. 1. Longitudinal and transverse magnetization in Cartesian coordinates. (A) T_1 recovery is depicted as the net magnetization vector relaxing towards longitudinal magnetization (bold arrow along z-axis). Whereas in (B) T_2 relaxation is depicted as the net magnetization vector receding away from transverse magnetization (dashed arrow along xy-axis). Further, the temporal relationship between T_1 and T_2 can observed; T_1 is a longer process than T_2. Adapted from Lipton, 2010.

1.1.2 MRI signal behaviour in non-homogenous samples

It is important to note that the electromagnetic signal measured using conventional MRI techniques is observed at the macroscopic spatial scale (≥ 1 mm); the net magnetization vector is in fact a sum of the component magnetization vectors generated by each ^{1}H-proton's magnetic moment. A consequence of acquiring the signal in this fashion results in an additional mechanism which contributes to transverse relaxation known as spin dephasing (Bloch, 1946). Initially, energy deposited in the form of radiofrequency waves establishes coherence between the individual magnetic moments, giving rise to the observable net, or bulk, magnetic signal. Over time, these individual magnetic moments lose coherence and accumulate phase, or angular distance, between one another. The phase is expected to

---

[d] This process is often referred to as T_1 recovery, as the T_1 signal increases throughout the time of signal acquisition. More specifically, T_1 is defined as the amount of time it takes to recover 63% of the net magnetization signal (Bloch, 1946; Goldman, 2001).

[e] T_2 is defined as the amount of time it takes to lose 63% of the net magnetization signal (Lipton, 2010).

accumulate linearly (or a linear loss of spin coherence) when measuring the MRI signal within a magnetically homogenous[f] sample. However, this is not the case in samples which contain or experience non-homogenous magnetic fields (Yablonskiy and Haacke, 1994). Magnetic field inhomogeneities can be classified broadly into two categories; (1) as 'local' field effects, arising from tissue related properties of a region or structure of interest, or (2) as 'non-local' field effects, such as magnetic interference from tissues of non-interest, hardware related deficiencies (e.g. primary magnet defects), or thermal noise. These magnetic field inhomogeneities, alongside spin-spin (T_2) relaxation, contribute in adjunct to the overall transverse relaxation of the bulk MRI signal measured, and can result in non-intuitive (deviations from mono-exponential decay and non-linear phase evolution) signal behaviour (Cronin et al., 2017; Schweser et al., 2011a; van Gelderen et al., 2012). For this reason, the dephasing effects of magnetic field inhomogeneities are conveniently labelled as $T_2^{'}$. Unless refocusing radiofrequency pulses are utilized to re-establish spin coherence, the measured transverse relaxation comprises the influence of both spin-spin relaxation and magnetic field inhomogeneities; the combined effect is referred to as T_2^* relaxation. The analytical relationship between T_2^*, T_2, $T_2^{'}$ is described below;

$$\frac{1}{T_2^*} = \frac{1}{T_2} + \frac{1}{T_2'}$$

Thus, by measuring T_2^*, we gain the benefit of two tissue related MRI signal parameters (spin-spin relaxation and magnetic field inhomogeneities), instead of merely one or the other (Markl and Leupold, 2012). The utility of these unique relaxation mechanisms for magnetic resonance imaging will be discussed in the following sections.

---

[f] A uniform spatial distribution of the magnetic field.

1.2 Establishing signal acquisition – gradient recalled echo magnetic resonance imaging

1.2.2 The Gradient Echo Sequence

Image contrast between different tissue types, also collectively referred to as tissue contrast, is the cornerstone of magnetic resonance imaging’s utility. By exploiting differences in the relaxation properties[g] (T_1, T_2, and T_2^*) of tissues, MRI signal acquisition sequences modulate image contrast between different types of tissue in the brain[h]. Recent studies have demonstrated substantially improved tissue contrast gained from a particular sequence known as gradient recalled echo, commonly abbreviated as GRE (Duyn et al., 2007; Liu, 2010; Liu et al., 2015; Reichenbach et al., 1997). By using alternating magnetic field gradients (in contrast to a spin-refocusing[i] radiofrequency pulse) to temporally propagate the MRI signal, the GRE sequence preserves the signal’s sensitivity to inhomogeneities in the static magnetic field (B_0) (Fig. 2) (Markl and Leupold, 2012).

---

[g] The longitudinal (T_1) and transverse (T_2) relaxation times depend upon a given sample’s composition and spatial distribution of hydrogen at the microscopic (< 0.1mm) and mesoscopic (0.1mm—1mm) scales. Since our work pertains to brain tissue, this would correspond broadly to the type, density, and size of organic (e.g. cells) and inorganic (e.g. minerals and metals) units, and how they are arranged within the structure of interest. But tissue microstructure (and subsequently composition and spatial distribution of micro-scale components) is relatively generalizable (consistent across multiple samples) at the macroscopic scale, thus we ascribe specific relaxation time constants for tissues. This property permits control over the signal measured from certain tissues over others, serving as the basis for image contrast in MRI.

[h] A detailed explanation of MRI sequences, and their principles, implementations, and applications can be found in (Mangrum et al., 2012).

[i] Commonly referred to as spin-echo.

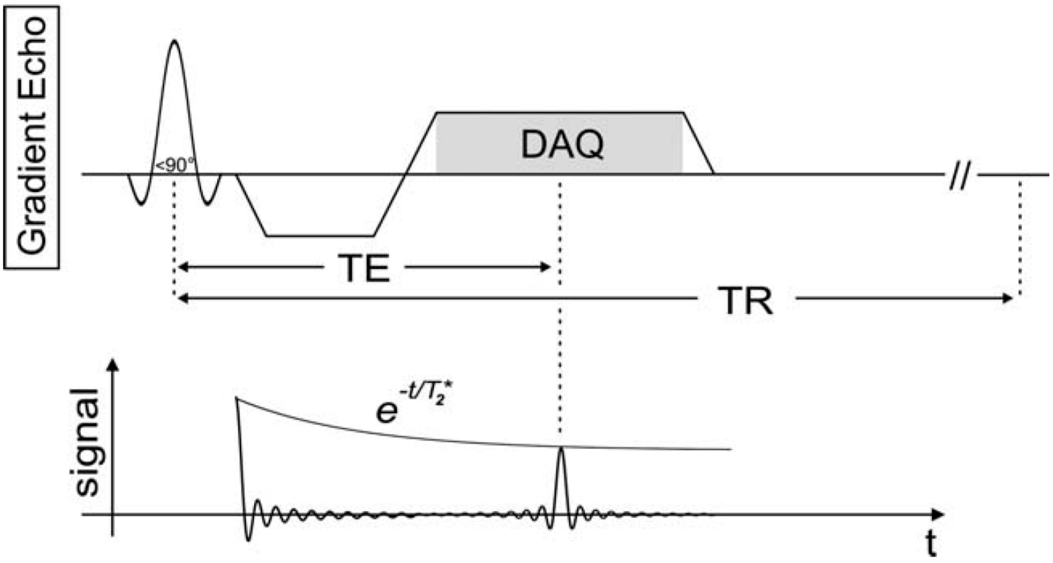

Fig. 2. A conventional GRE-MRI sequence. The signal in GRE-MRI is initiated by a 90° (or < 90°) radiofrequency pulse, tipping the net magnetization vector into the transverse plane. The unique facet of GRE-MRI lies in the formation of echoes (or recovery of spin coherence) through a reversal of the gradient magnetic field. As a result, the gradient echo signal intensity is determined by T_2^* decay and field inhomogeneity effects are not refocused at the time of signal formation. DAQ reflects the period of data acquisition. Adapted from Markl and Leupold, 2012.

1.2.2 Properties of the GRE-MRI signal

The net magnetization vector generated by the precessing ^{1}H-proton spin populations are observed by the signal receiver coils[j] as a temporally oscillating electrical signal, commonly referred to as the free indication decay (FID) (Bloch, 1946). The FID signal is encoded as a periodic function and undergoes a Fourier transform, yielding a complex valued signal that bears a magnitude (real component) and phase (imaginary component); both the signal magnitude and signal phase can be used uniquely to reconstruct the MRI image, as will be discussed in later sections. A defining property of the GRE-MRI signal is the benefit of signal phase (Schweser et al., 2016). The signal phase is largely absent in spin-echo MRI (SE-MRI), which relies on a refocusing radiofrequency pulse to propagate the temporal signal, thus eliminating inherent phase offsets.

The sensitivity of GRE-MRI signal phase to static field inhomogeneities is derived directly by measuring the local frequency offset ($\Delta\omega$) of ^{1}H-proton spin populations relative

---

[j] Electromagnetic sensors of the MRI machine.

to the Larmor frequency (ω), or the frequency at which a ^{1}H-proton precesses around an externally applied magnetic field (Duyn and Schenck, 2017; Reichenbach et al., 1997; Yablonskiy and Haacke, 1994). These frequency offsets reflect the mean magnetic field perturbation seen by spins within a voxel[k]. This relationship can be described in the laboratory frame[l] of reference as,

$$\Delta f_{MR}(\vec{r}) = -\frac{\gamma}{2\pi}(B_{inhom} + B_{demag})$$

in a right-hand coordinate system (Schweser et al., 2016), wherein γ represents the gyromagnetic ratio ($2.67 * 10^6 \frac{rad}{s \cdot T}$ or $42.57 \frac{MHz}{T}$) for the ^{1}H-nucleus, B_{inhom} representing field inhomogeneities arising from non-local and non-tissue related effects (e.g. shimming and main magnetic field variations), and B_{demag} representing the tissue-related demagnetizing effects on the local magnetic field. These demagnetizing effects comprise of both diamagnetic (an induced magnetic field anti-parallel to the static magnetic field) and paramagnetic (an induced magnetic field parallel to the static magnetic field) constituents (Schweser et al., 2016). Both, diamagnetic and paramagnetic, substances would induce localized variations in the static magnetic field strength, and consequently result in protons to precess outside the Larmor frequency bandwidth and a net loss in overall signal magnitude. Recent studies in MR neuroimaging have elucidated the substantial utility of signal phase in enhancing observable contrast between different tissue types (Fig. 1) (Deistung et al., 2008; Duyn et al., 2007; Reichenbach, 2012; Reichenbach et al., 2015, 1997; Schenck and Zimmerman, 2004).

---

[k] A volumetric pixel.

[l] Also referred to as the 'real-life viewpoint', wherein precession of the NMV about B_0 is observed in 3-D as a function of time.

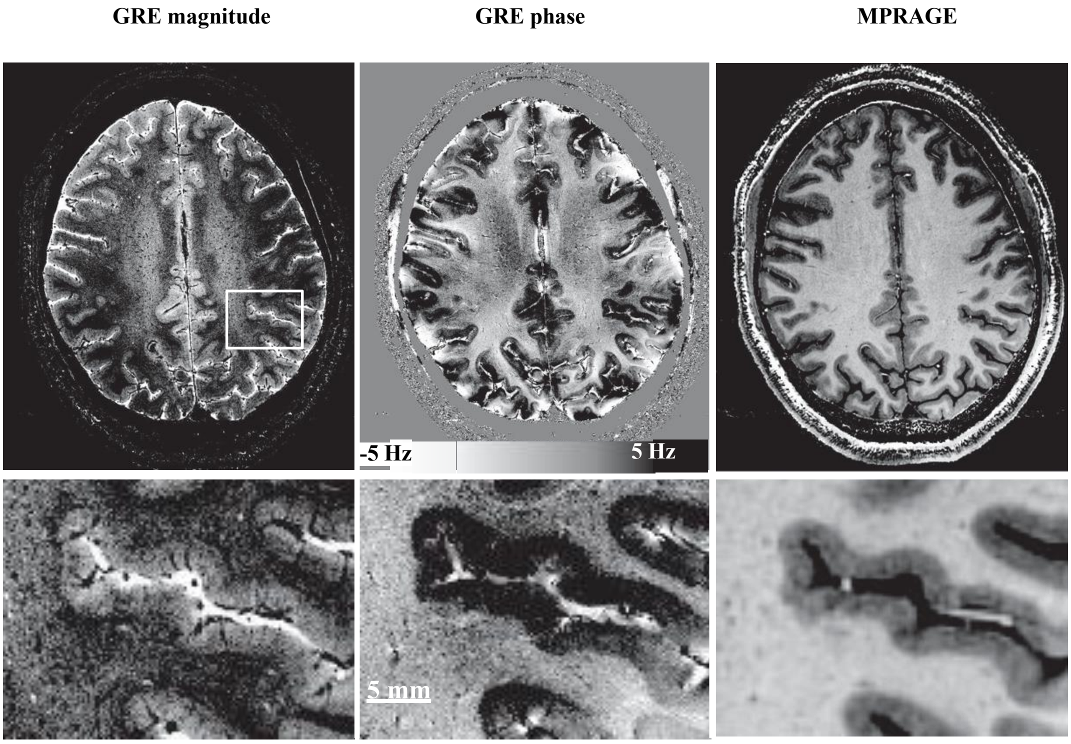

Fig. 3. Comparing image quality and tissue contrast based from in different MR sequences. Tissue contrast in GRE magnitude, GRE phase, and MP-RAGE images allow for discrimination between gray and white matter regions in the brain. Duyn et al. report nearly 10x increased contrast between gray and white matter using GRE phase data acquired at 7T (Courtesy of Duyn et al., 2007).

1.2.3 The utility of GRE-MRI in susceptibility imaging

Tissue related effects on the local magnetic field can provide valuable information about the composition and abundance of different cellular and molecular species in that particular region of interest (He and Yablonskiy, 2009; Marques et al., 2009; Reichenbach et al., 1997). These include, but are not limited to effects, such as chemical exchange (Luo et al., 2010; Shmueli et al., 2017, 2011; Zhong et al., 2008) and magnetic susceptibility (Duyn and Schenck, 2017; Haacke et al., 2015; Langkammer et al., 2012; Lee et al., 2012; Schweser et al., 2012, 2012; Wang and Liu, 2015). T_2^*-weighted GRE-MRI has gained recent prominence in mapping the magnetic susceptibility of tissues in the brain (Argyridis et al., 2014; Kim et al., 2017; Li et al., 2011; Schweser et al., 2011b, 2012). GRE-MRI based susceptibility-processing techniques, such as susceptibility-weighted imaging (SWI) and quantitative susceptibility mapping (QSM), allow for enhanced visualization of unique neural tissue types (e.g. white matter, gray matter and CSF) at a high spatial resolution (Duyn, 2017; Liu et al., 2015, 2015; Reichenbach et al., 2015; Schweser et al., 2016). SWI enhances susceptibility-induced contrast by merging the T_2^* weighted magnitude image with a filtered phase map in a multiplicative fashion (de Crispgny et al., 1993; Liu et al., 2015). However, SWI images can only provide qualitative information about an anatomical region because the individual voxels do not reflect a physical quantity. Quantitative susceptibility mapping (QSM) on the other hand is an emerging post-processing tool that isolates the local tissue magnetic susceptibility (*source*) from the measured magnetic field distribution (*effect)* (Li et al., 2014; Liu et al., 2009; Marques and Bowtell, 2005; Reichenbach et al., 2015; Sun and Wilman, 2014). SWI and QSM share similar parameters with regards to data acquisition, as well as certain data processing procedures, such as phase unwrapping, background field removal, and mask generation. QSM deviates from SWI by how it proceeds to utilize the unwrapped and filtered phase data; instead of multiplying the phase by the magnitude, the phase is numerically processed to solve for magnetic susceptibility.

QSM has been extensively utilized to study the magnetic properties of brain and nervous tissue in healthy, aging, and disease conditions. Mean susceptibilities of bulk tissue in white matter and deep gray matter regions have also been measured using QSM (Langkammer et al., 2012). QSM is commonly used to quantify iron content in the brain. Iron deposition in the brain increases with normal aging and has been implicated in age-related motor and cognitive impairment (Bartzokis et al., 2010; Sullivan et al., 2009; Koopmans et al., 2008). QSM has been successfully utilized to quantify iron content in the basal ganglia, midbrain, and iron tagged stem cells (Reichenbach et al., 2015). Due to an age-dependent effect of iron on magnetic susceptibility, however, a normalized range and variation of susceptibility values must first be established prior to drawing any conclusions based on iron content (Hallgren et al., 1958). QSM's sensitivity in detecting (micro-) hemmorhages has increased its utility for traumatic brain injury (TBI) imaging, and extending its application so far as to distinguish mild and severe cases (Li et al., 2014; Liu et al., 2015b). By enabling quantitative detection of longitudinal lesion changes, QSM's role as a biomarker for MS is being investigated (Blazejewska et al., 2014; Chen et al., 2014; Langkammer et al., 2013). QSM has also been validated as a highly robust means of differentiating paramagnetic and diamagnetic blood. This has key implications in studying tumoral calcification and architecture (Reichenbach et al. 2015; Sehgal et al., 2006).

Beyond the spatial influence of magnetic susceptibility, non-linear variations in the temporal GRE-MRI signal have also been attributed to tissue-specific susceptibility effects (Cronin et al., 2017; Schweser et al., 2011; Schweser et al., 2016; Sood et al., 2017; van Gelderen et al., 2012). For this reason, the multi-echo GRE-MRI (mGRE-MRI) sequence has increasingly been used to visualize and quantify magnetic susceptibility in brain tissue from echo-time dependent data. The use of temporal susceptibility mapping will be further discussed in the following section.

1.3 Decoding the mGRE-MRI signal through compartmentalization

Early nuclear magnetic resonance (NMR) studies have already demonstrated shifts in the resonant frequency induced as a direct result of "bulk (magnetic) susceptibility", or a sum of discrete microscopic signal influences (Chu et al., 1990; Hopkins and Wehrli, 1997; Kubo et al., 1998; Szczepaniak et al., 2002). An increasing number of studies have aimed to spatially map, characterize and quantify susceptibility effects and represent them as unique intra-voxel signal compartments (Chen et al., 2013; Hernando et al., 2008; Wu et al., 2017; Xu et al., 2015). For example, a technique known as myelin water fraction (MWF) imaging has greatly benefitted from the use of mGRE-MRI. The original MWF imaging technique developed by Mckay et al. (1994) introduced a novel method of visualizing (in-vivo) white matter based on the multi-exponential decomposition of T_2 relaxation. Through a least-squares fitting approach of the T_2 signal, two distinct signal components were identified; a fast relaxing (or short) component ascribed to water trapped between the myelin layers, and a slow relaxing (or long) component designated to mobile intra— and extra—axonal water (Mackay et al., 1994). Utilizing these differential T_2 values, the fractional occupancy of myelin water was mapped in a pixel-wise manner. Histopathological studies have validated a strong correlation between myelin water fraction and myelin content (Kozlowski et al., 2008; Lancaster et al., 2003; Laule et al., 2008, 2008; Moore et al., 2000; Webb et al., 2003).

The multi-parametric fitting approach aims to discretize the magnetic field changes contained within a millimeter-scale voxel. These micro-scale (< 1.0mm) effects are commonly referred to as ‘signal compartments’(Chen et al., 2013; Du et al., 2007; Duyn and Schenck, 2017; Sati et al., 2013). The signal compartmentalization approach was adapted and further optimized, using mGRE-MRI magnitude data, to characterize water micro-environments (the myelin water pool (*my*), axonal water pool (*ax*) and extracellular water pool (*ex*)) and investigate myelin integrity in white matter structures (Du et al., 2007; Hwang et al., 2010). MWF mapping via T_2^* compartmentalization has also been validated through post-mortem histopathological analysis (Du et al., 2007). MGRE-MRI based MWI presents numerous technical advantages over the conventional multi-echo SE-MRI; namely, larger volume coverage, faster scan time, lower specific absorption rate, and insensitivity to B1 inhomogeneity. Furthermore, mGRE-MRI data provides the opportunity to gain additional information about myelin integrity through susceptibility related contrasts derived from T_2^*, phase and susceptibility maps (Baxan et al., 2010; Duyn et al., 2007; Lee et al., 2012; Li et al., 2006; C. Liu et al., 2011; Shmueli et al., 2009; Wu et al., 2017).

Recent works extend the use of multi-exponential models to mGRE-MRI signal compartments through the incorporation of signal phase information (e.g. using complex terms to define signal compartments (Hernando et al., 2008; Li et al., 2015; Nam et al., 2015; Sati et al., 2013, 2013; van Gelderen et al., 2012). When examining the T_2^* signal behaviour in white matter, Van Gelderen et al. (2012) report higher residual errors in areas exhibiting greater structural order (e.g. densely myelinated anisotropic nerve fibers) compared to areas with less structural coherence (e.g. interstitial space with isotropic inclusions). Further, these residual errors were enhanced at higher field strengths. The authors ascribe these effects to susceptibility induced shifts in the signal phase, and improve the quality of signal fit through the addition of a complex-valued frequency offset term in two signal compartments (van Gelderen et al., 2012). This model, however, proved less robust in explaining white matter signal behaviour when compared to a more advanced signal model which assigns three distinct frequency shift parameters to three different signal compartments (myelin water, axonal water, and extracellular water/cerebrospinal fluid) (Alonso-Ortiz et al., 2017; Li et al., 2015; Nam et al., 2015; Sati et al., 2013; Wu et al., 2017). By defining a frequency shift parameter through the phase component of each signal compartment, the complex model fitting approach has benefited from a reduction in structured residual errors and the generation of frequency shift maps (Alonso-Ortiz et al., 2017; Nam et al., 2015). This advance has played an important role in improving stability of myelin water fraction estimation (Nam et al., 2015; Wu et al., 2017).

The utility of GRE-MRI signal compartmentalization extends beyond the domain of MWF imaging. For example, a two-compartment complex-valued model was used to enhance contrast between water and fat in dixon-type mGRE-MRI acquisitions (Hernando et al., 2008). A recent simulation study utilizes the multi-compartment complex-valued plane wave model to investigate the susceptibility effects iron-rich oligodendrocytes in white matter (Xu et al., 2015). Signal compartments have also been recently identified in gray matter regions by utilizing a three-compartment susceptibility model to explain temporal trends in magnetic susceptibility (Sood et al., 2017). At large, however, the utility of signal compartments to study tissue properties in non-white matter regions remains largely unexplored.

1.4 Decoding the mGRE-MRI signal through compartmentalization

1.4.2 *The challenges of tissue phase*

Although the inclusion of phase information has benefitted signal compartmentalization, this approach presents a new set of signal processing challenges. These issues relate to the removal of non-local, or background phase offsets, and therein having to deal with phase wraps (folding of signals into the $-\pi$ to π range) (Li et al., 2014; Liu et al., 2015; Schweser et al., 2016). Removal of macroscopic susceptibility effects has been attempted through shimming (van Gelderen et al., 2012), filtering (e.g. high-pass, low-pass, and Gaussian) (Chen et al., 2013; Li et al., 2015; Sati et al., 2013), and by incorporating a parameter for background phase into the model for data which has not been background field filtered (Li et al., 2015; Nam et al., 2015; Wu et al., 2017). In addition to the aforementioned techniques, more sophisticated phase unwrapping and background field removal techniques have emerged for voxel-wise quantification of tissue susceptibility. For example, the sophisticated harmonic artefact reduction for phase data (SHARP) method (Sun and Wilman, 2014) and its variants (Li et al., 2011; Schweser et al., 2011b; Wu et al., 2012) the projection onto dipole fields (PDF) method (Liu et al., 2011), and harmonic phase removal using the Laplacian operator (HARPERELLA) (Li et al., 2014; Sood et al., 2017).

Phase unwrapping techniques can be classified broadly into two categories; algorithms that unwrap in the spatial domain and temporal domain (Haacke et al., 2015).

Both approaches aim to estimate the integer number of phase cycles necessary to correct measured phase values that extend beyond the –π to π polar boundary (Schweser et al., 2016). Phase unwrapping for individual voxels in the spatial domain uses neighboring voxels to estimate the true phase, while temporal unwrapping utilizes changes in the temporal signal phase of each voxel. For this reason, temporal unwrapping techniques can only be applied to multi-echo data. Recent attempts at phase unwrapping within signal compartmentalization works include frequency offset subtraction from a linear fitting procedure in the temporal domain (Li et al., 2015; Sati et al., 2013) and cost-function based integer programming approaches (Hammond et al., 2008; Nam et al., 2015). A comprehensive review about phase unwrapping, as well as other methods, underlying principles, and applications related to signal phase processing can be found in a recent review article authored by Schweser et al., (2016).

1.4.3 *The benefits of tissue susceptibility*

As detailed in section *1.2.3,* an entire field of research, namely QSM, has emerged with the sole aim of isolating the local tissue magnetic susceptibility (Haacke et al., 2015; Kee et al., 2017; Li et al., 2011; Liu et al., 2015; Reichenbach et al., 2015; Schweser et al., 2012). A recent study adopted this approach within the context of myelin water fraction imaging, and reported more robust parameter estimations and reduced signal artifacts after replacing unfiltered phase data with local susceptibility information (Fig. 4; Wu et al., 2017). Thus, incorporating susceptibility-induced frequency shifts into the signal compartmentalization process would serve as a rational means of investigating tissue properties at the voxel-level.

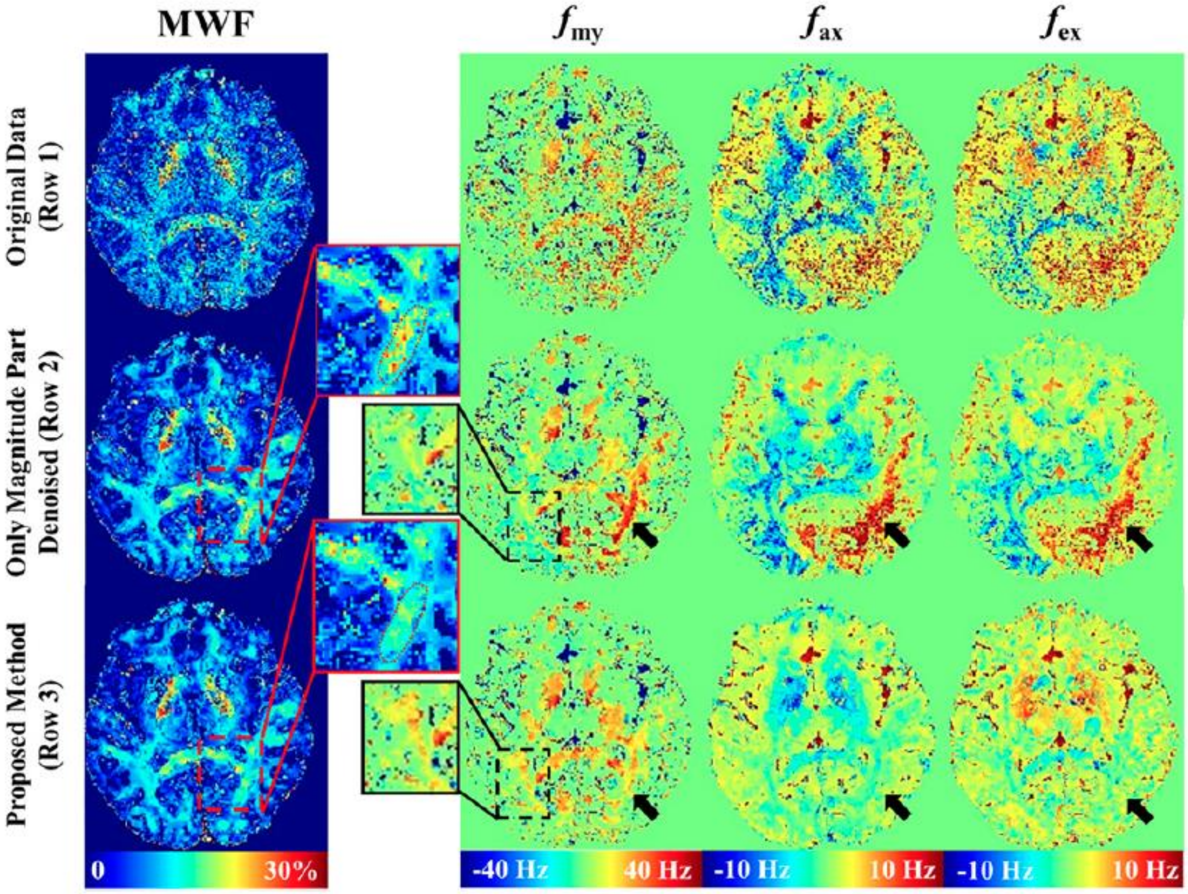

Fig. 4. Myelin water fraction imaging by incorporating tissue susceptibility (Adapted from Wu et al., 2017). MWF maps were generated by fitting the mGRE-MRI signal via three different methods; in Row 1 the complex data comprised of magnitude and tissue phase; in Row 2, only the magnitude data was used; and in Row 3, the complex data was also incorporated magnitude information, but with phase data after being processed using QSM. In Row 3, a clear reduction of image artefacts can be observed through the use of local susceptibility information in place of tissue phase.

Chapter 2: Frequency shifts in multi-echo GRE-MRI signal compartments reflect underlying tissue microstructure in the brain

2.1 Introduction and Aims

Though signal compartments have been identified in white matter regions, a recent study explains non-linear trends in echo-time dependent magnetic susceptibility using a three-compartment model (Sood et al., 2017). These findings promote further investigation into echo time dependent non-linear frequency shift effects due to a lack of ordered microstructures, namely myelin, to give rise to distinct water micro-environments, the traditionally proposed source of signal compartments in gray matter brain regions (Duyn et al., 2007; Koenig, 1991; Lee et al., 2012; O'Brien and Sampson, 1965). For example, the signal frequency is influenced by local susceptibility inclusions such as iron (Abduljalil et al., 2003; Drayer et al., 1986; Fukunaga et al., 2010; Schenck and Zimmerman, 2004; Todorich et al., 2009), calcium (Li et al., 2011; Liu et al., 2009; Schweser et al., 2011), neurofilaments (He and Yablonskiy, 2009; Luo et al., 2010; Yablonskiy et al., 2012), tissue anisotropy (Hong et al., 1971; Lee et al., 2017; W. Li et al., 2012; X. Li et al., 2012; Yablonskiy and Sukstanskii, 2017), and dynamic proton interactions (e.g. dipolar coupling, chemical exchange, slow diffusion, etc.) (Leutritz et al., 2013; Ruh et al., 2017; Shmueli et al., 2011; van Zijl et al., 2017; Yablonskiy and Haacke, 1994) throughout the brain. Such effects could contribute to an outcome which mimic changes due to magnetic susceptibility with a subsequent influence on signal compartment parameters. Signal compartmentalization using parameters influenced by magnetic susceptibility variations would additionally allow for a more acute and less confounded analysis of tissue properties, herein defined as the composition and spatial arrangement of the primary components, at the meso-microscopic interface (0.1 – 0.5mm).

Taken together, GRE-MRI signal compartments in non-white matter regions, and effectively outside the context of myelin water fraction (MWF) imaging, remain largely unexplored. In white matter the geometry of fibre bundles and the distinctly different magnetic susceptibility of myelin from its surroundings underpins the three-water pool model. However, the number of complex-valued signal compartments across other brain regions remains. To this end, we investigated the number of signal compartments in a range of human brain regions (including gray matter, white matter and CSF) using a data driven approach in selecting appropriate multi-compartment models. We maximized our sensitivity to local signal influences by working with magnetic susceptibility prior to complex signal fitting in the multi-echo GRE-MRI regime. We aimed to establish how the number of signal compartments vary across brain regions and whether they are shared across brain regions which exhibit microstructural diversity.

2.2 Methods

2.2.1 *Data acquisition*

The experiment was conducted after having been provided ethical clearance by the University of Queensland human ethics committee. In vivo brain imaging (consent was provided by five healthy adult volunteers with a mean age of 34 ± 4 years) sessions were conducted on a 7T whole-body MRI research scanner (Siemens Healthcare, Erlangen, Germany) equipped with a 32-channel head coil (Nova Medical, Wilmington, Massachusetts). Thirty echo 3D gradient recalled echo scan was acquired with the following acquisition settings: $TE_1 = 2.04$ ms and echo spacing of 1.53 ms, TR = 51 ms, flip angle = 15^o, voxel size = $1 \times 1 \times 1$ mm^3 and matrix size = $210 \times 168 \times 144$.

2.2.2 *Signal processing and quantitative susceptibility mapping*

The magnitude image of each channel was used to form a channel mask using the BET tool provided as part of MIPAV 7.3.0 (http://mipav.cit.nih.gov/). The result was read into MATLAB 2015b (The MathWorks, Natick, Massachusetts) from which a binary mask was created. STI Suite V2.2 (http://people.duke.edu/_cl160/) was used to process susceptibility maps in a channel-by-channel manner, as described previously (Bollmann et al., 2015). iHARPERELLA (background phase removal) and iLSQR (solving for susceptibility based on background field corrected tissue phase) in STI Suite were used to generate 3D susceptibility maps for each echo time.

2.2.3 *Region-of-interest selection*

We considered nine brain regions, namely the caudate, putamen, fornix, corpus callosum, internal capsule, insula, substantia nigra, thalamus, and cerebrospinal fluid (CSF). Three sub-cortical white matter regions, namely the corpus callosum, internal capsule, and fornix were chosen for comparison of signal compartment parameters to those identified previously in MWF imaging studies. Five sub-cortical gray matter regions, namely the caudate, putamen, insula, substantia nigra, and thalamus were selected as a representative sample of overall sub-cortical gray matter structures. Although the spatial arrangement of tissue microstructure would differ across these regions, the underlying composition (e.g. neurons, glia, biometals, etc.) of these structures can assumedly be conserved at the meso-microscopic spatial interface. Consequently, trends in signal-specific signatures of these tissue components, encoded as shifts in the Larmor frequency, can be probed systematically across specific regions to reveal underlying similarities and differences in tissue microstructure. Manual segmentation guided by a human brain atlas (Leutritz et al., 2013) was performed in MIPAV using a number of different echo time 7T magnitude images based on the clarity of structural contrast (Fig. 1). Segmentation boundaries for all regions-of-interest (ROI) were avoided by a distance of approximately two voxel lengths from adjacent regions in order to minimize partial volume effects. This approach allowed us to produce brain region masks corresponding to brain regions with a high level of confidence.

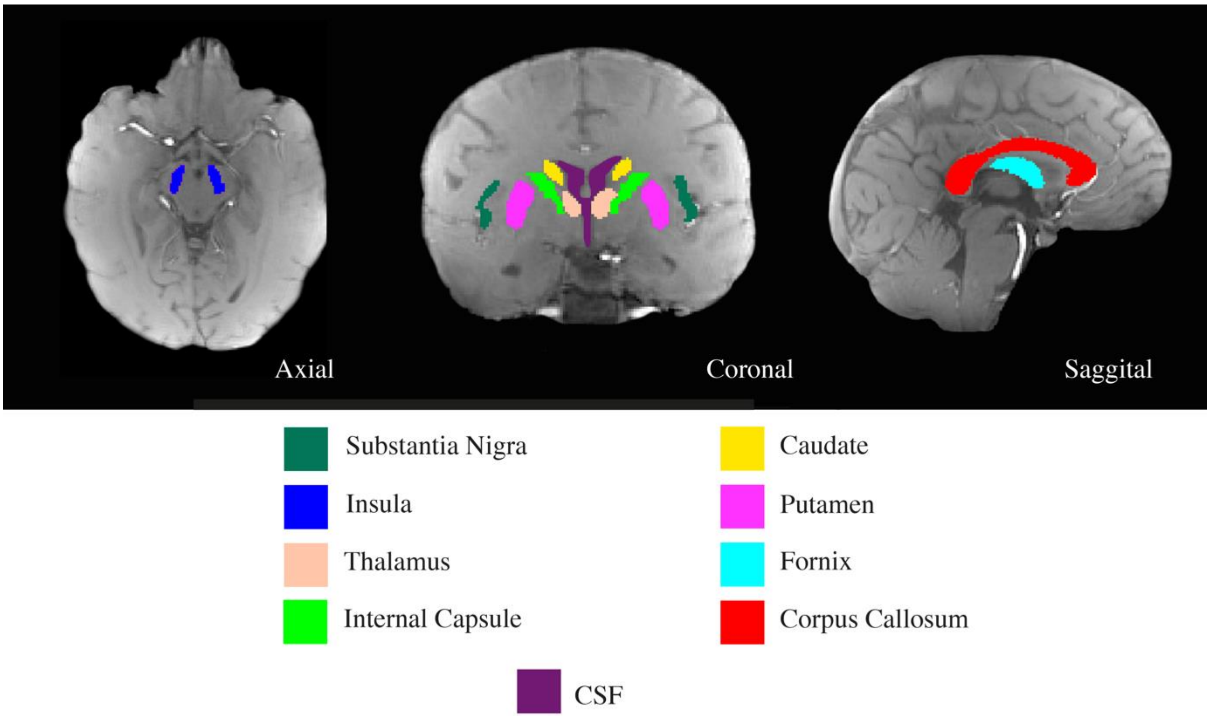

Fig. 1. Illustration of the brain regions investigated.

2.2.4 *Complex signal generation*

Previous studies generate the temporal complex signal by combining the signal magnitude and tissue phase (unwrapped raw phase) data for each echo-time (Hernando et al., 2008; Li et al., 2015; Nam et al., 2015; Sati et al., 2013). This method, however, suffers from signal influences arising from non-local magnetic fields. Instead, we converted tissue phase to quantitative susceptibility maps from which we then computed the frequency shift to overcome drawbacks of working with tissue phase directly (Wu et al., 2017).

First, the raw phase data was processed using HARPARELLA, or harmonic phase removal using the Laplacian operator. HARPERELLA shows particular promise in providing simultaneous processing capability for both phase unwrapping and background removal (Liu et al., 2015). This method has also proved to be robust in preserving tissue phase integrity across gray and white matter regions, as well as cerebrospinal fluid (Li et al., 2014). Signal phase values were averaged across hemispheres and repeated for each echo time (Sood et al., 2017). This formed the temporal phase, which was subsequently fed into the STI Suite pipeline for calculation of temporal susceptibility data for each participant. The sparse linear equation and least-squares (iLSQR) method implemented within the STI Suite package has been shown to be a robust and unbiased method of quantifying local magnetic susceptibility, thus qualifying its use for our work (Liu et al., 2015; Sood et al., 2017; Sukstanskii and Yablonskiy, 2014). Prior to complex signal generation, the regional magnitude and susceptibility signal were averaged across all participants. The susceptibility values for each echo-time were converted to frequency shifts by a modification of the Larmor equation,

$$\omega = \gamma B_0$$

$$\Delta\omega = \gamma \Delta B_0$$

where $\Delta\omega$ represents the angular shift in the Larmor frequency due to the induced field change, denoted as ΔB_0, and γ representing the gyromagnetic ratio of hydrogen. Further, changes in the local static field arise from magnetic susceptibility induced influences, denoted as χ,

$$\Delta B_0 = \chi B_0$$

This allows for a substitution of magnetic susceptibility into the Larmor equation, yielding,

$$\Delta\omega = \gamma \chi B_0$$

The angular frequency shift, $\Delta\omega$, can be mapped on to the Cartesian plane via the periodic convolution $\Delta\omega = 2\pi\Delta f$. Finally, a solution for Δf can be derived from a re-arrangement of the susceptibility-substituted Larmor equation. The conversion took the form (in a right-handed coordinate system):

$$\Delta f = \chi \frac{\gamma B_0}{2\pi},$$

where χ is the magnetic susceptibility value generated using the STI Suite pipeline, γ is the gyromagnetic ratio of hydrogen and B_0 = 7T (Reichenbach et al., 1997; Schweser et al., 2011; 2016). Prior to generating a complex signal based on signal magnitude and frequency shift, voxel values within each region were averaged. The temporal measured complex signal (S_m) for each region was then generated as a function of the measured signal magnitude (A_m) and measured frequency shift (Δf_m) at each echo-time (t):

$$S_m(t) = A_m(t)e^{-i2\pi\Delta f_m t}.$$

2.2.5 *Signal compartmentalization*

GRE-MRI signal compartment models have evolved over the years. Du *et al.* (2007) introduced the "three-pool model" for temporal GRE-MRI data, with the purpose of characterizing water micro-environments and investigating myelin integrity in white matter at the 3T MRI field strength. This was a real-valued model and contributions from the myelin (*my*), axonal (*ax*) and extracellular (*ex*) water pools were estimated through model parameters. Thereafter, GRE-MRI signal compartments were investigated at both 3T and 7T field strengths (Hernando et al., 2008; Li et al., 2015; Nam et al., 2015; Sati et al., 2013, 2013; van Gelderen et al., 2012) and, it was concluded that fitting quality improves with the addition of signal phase in the model. Nam et al. compared various models and showed spatially resolved maps of model parameters based on a model in which all three signal compartments were complex valued. Subsequently, Wu et al. proposed a pipeline for compartmentalizing temporal GRE-MRI data, which uses the QSM pipeline instead of directly computing frequency shifts from signal phase. This pipeline is less sensitive to noise in the data and has been applied to high resolution GRE-MRI data.

In accordance with previous studies (Li et al., 2015; Nam et al., 2015; Sati et al., 2013; Wu et al., 2017), compartments of the complex GRE-MRI signal were formulated using the amplitude modulated plane wave formulation:

$$S_n(t) = A_n(t)e^{-i(2\pi\Delta f_n t+\phi_n)}$$

where n is the signal compartment number, A_n denotes the signal magnitude, Δf_n defines the compartment frequency shift, and ϕ_n is an induced phase shift. We omitted the phase shift in our work since calculations used local magnetic susceptibility derived having performed background field removal (Li et al., 2014). Magnetic field changes introduced by micro-scale (< 100μm) effects were assumed to be confined to millimeter-scale (100μm – 1000μm) voxels; a dipole representation for individual voxel signal compartments can thus be avoided (Chen et al., 2013; Sood et al., 2017). This allows us to express each signal compartment of an image voxel as a relaxation modulated complex-valued plane wave:

$$S(t) = \sum_{i=1}^{N} A_i(t) e^{-\frac{t}{T_{2,i}^*} - i2\pi\Delta f_i t},$$

where N is the total number of signal compartments used to fit the measured signal, A_i denotes the volume fraction, $T^*_{2,i}$ defines the compartment spin-spin relaxation time in the presence of field inhomogeneities, and Δf_n signifies the frequency shift for each signal compartment. We considered the cases of $N = 1$ to 6. We implemented a non-linear least squares fitting algorithm in MATLAB (Mathworks, Natick, MA, USA) and solved for model parameters (A_i, $T^*_{2,i}$, and Δf_i). Initial values and optimization search ranges are summarized in Table 1. Initial values for the volume fraction were varied for the six compartment models tested; volume fractions for each compartment were set to $\frac{|S(TE_1)|}{N}$, for compartments $N = 1 \; to \; 6$; T_2^* values were set within realistic ranges as reported previously by Peters et al. (2007); and Δf in view of previous studies on GRE-MRI signal compartments (Alonso-Ortiz et al., 2017; Li et al., 2015; Sati et al., 2013; van Gelderen et al., 2012; Wu et al., 2017). Besides the fixed upper and lower bounds, no other optimization constraint, penalty function, or weighting was used for signal fitting. This was performed to reduce parameter estimation bias and ensure a data-driven analysis. Modifications to the initial values did not result in different fitted parameter values; provided in Appendix Table 1 are parameter estimates for three different initializations. We ran 40,000 iterations when a 1 compartment model was used, and doubled the number of iterations for every additional compartment to account for increases in search space dimensionality (e.g. three search dimensions introduced through the addition of each compartment).

Table 1
Initial values and search range used to estimate parameters of one to six compartment signal models. $S(TE_1)$ denotes the magnitude of the first-echo signal. $N = 1\ to\ 6$ (number of compartments).

	A (a.u.)	T_2^* (ms)	Δf (Hz)
Initial value	$\frac{\lvert S(TE_1)\rvert}{N}$	30	0
Lower bound	0	0	-150
Upper bound	$2 \times \lvert S(TE_1)\rvert$	200	150

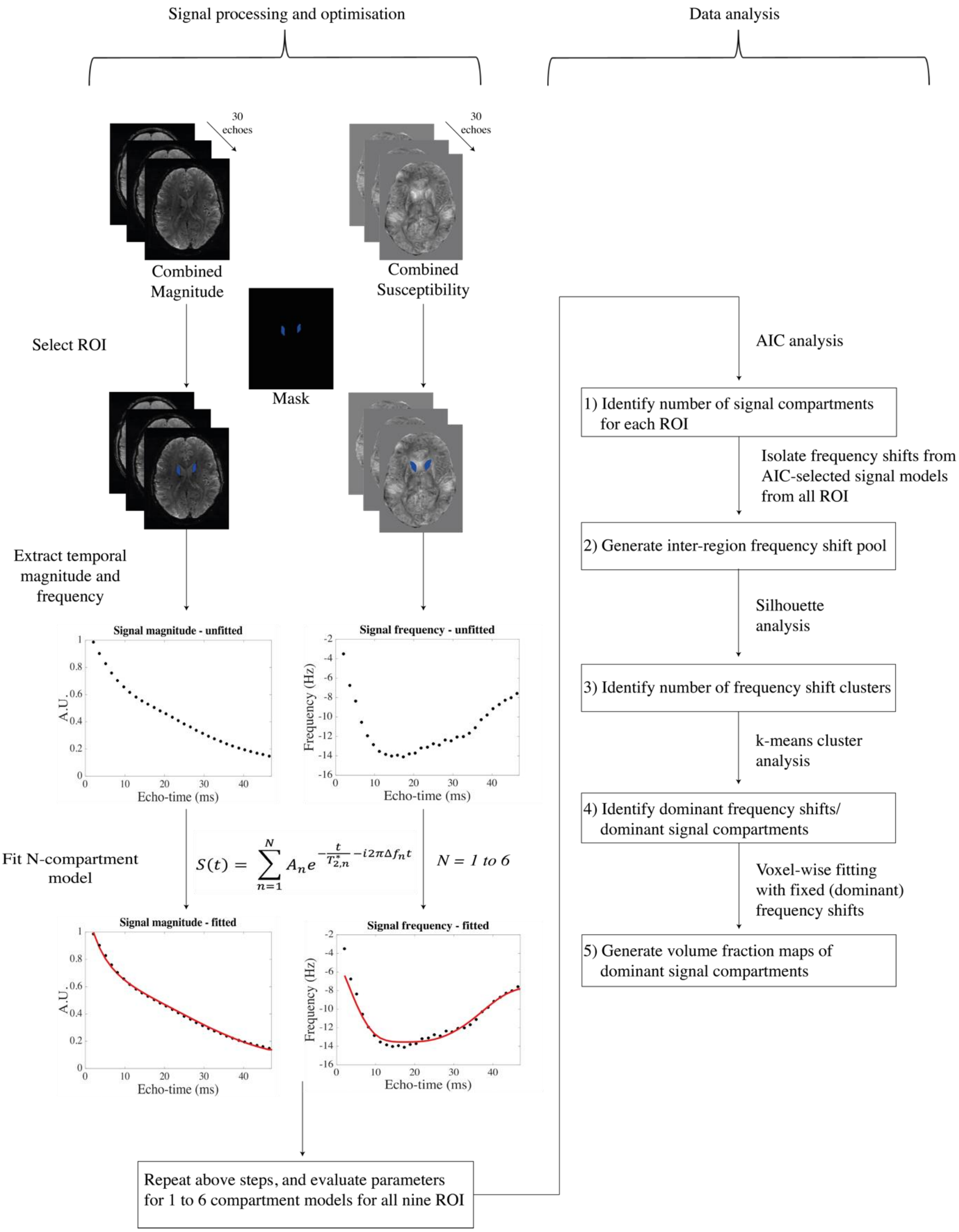

Fig. 1. Data processing and analysis pipeline—example given for the caudate in one participant. (a) ROIs were selected from combined magnitude and combined susceptibility data (mask manually generated via magnitude images). (b) Averaged magnitude and susceptibility values were calculated for each ROI; averaged susceptibility values were converted to frequency shifts at each echo time. (c) The complex signal was generated using as a function of magnitude, frequency shift, and echo-time, and fitted to a multi-compartment (1 to 6) model. (d) The most parsimonious compartment models were selected via the AIC for further analysis.

2.2.6 *Model selection and cluster analysis*

Achieving model parsimony, or the ideal balance between bias and variance, requires a model to exhibit accuracy and simplicity in describing the measured data (Vandekerckhove et al., 2014). We implemented the Akaike Information Criteria (AIC) to be able to accurately assess features in the data without overfitting (Akaike, 2011; Naik et al., 2007). The AIC fine tunes model parsimony by reinforcing improvements in quality-of-fit and penalising an increasing number of parameters. Further, the AIC allows for comparison of two or more models to the unknown true distribution via a maximum likelihood estimation. When fitting a model using least squares regression, the likelihood function can be estimated by the residual sum of squares (RSS) returned by the least squares fit, yielding;

$$AIC = n\log\left(\frac{RSS}{n}\right) + 2k,$$

wherein n is the number of independent measurements, and k represents the number of unknown parameters. When implementing the AIC for a small sample, or measurement (e.g. $n/k < 40$), size, an additional bias correction penalty term is required (Bedrick and Tsai, 1994; Burnham and Anderson, 2004); this yields a 'corrected' AIC (AIC_C) metric, formulated as,

$$AIC_c = AIC + \frac{2k(k+1)}{n-k-1}.$$

Taken together, we used the AIC_C metric to identify the number of signal compartments within each ROI. The model exhibiting the lowest AIC_C value, considered as the most parsimonious, was selected for inter-region comparison of compartment frequency shifts (labelled as 'AIC-selected models'). We performed a k-means cluster analysis of the AIC-selected compartment frequency shifts between all nine brain regions to ascertain the 'dominant' underlying signal influences shared across the regions investigated. k-means clustering is a vector quantization method which aims to partition a data set into subcomponents with optimally shared features (Lloyd, 1982). k-means clustering is typically implemented as an iterative optimization method, wherein a sample with *n* observations are partitioned into *k* clusters (Kaufman and Rousseeuw, 2009; Lloyd, 1982). Moreover, the individual observations (n) are assigned to a specific cluster (k) with the nearest mean (minimized by a distance measure or cost function), or centroid value; these values serve as the representative quantitative feature of the respective clusters. Different heuristics have been proposed in order to identify representative seeds for the centroid values (Arthur and Vassilvitskii, 2007; Ertöz et al., 2003; Kaufman and Rousseeuw, 2009). Through simulation results, the k-means^{++} seeding approach has been shown to yield smaller net distance measures (or cost-function errors) at a substantially improved convergence rate in comparison to traditional methods (Arthur and Vassilvitskii, 2007). The value of *k* is chosen prior to the optimization process; optimal number of frequency shift clusters were determined using a silhouette (SI) analysis. The mean silhouette (SI) value quantifies how close each point in one cluster is to points in the neighbouring clusters. The silhouette value for the ***i***th point, SI, is defined as;

$$SI = \frac{(bi - ai)}{max(ai, bi)},$$

where *ai* is the average distance from the ***i***th point to the other points in the same cluster as ***i***, and *bi* is the minimum average distance from the ***i***th point to points in a different cluster, minimized over clusters (Kaufman and Rousseeuw, 2009). A high SI value indicates that ***i*** is well-matched to its own cluster, and poorly-matched to neighbouring clusters; thus, a high SI mean indicates better clustering. All analyses within this section were performed in MATLAB, and built-in functions were utilized for k-means clustering (inclusive of k-means^{++} seeding) and SI analysis.

2.2.7 *Analytical connection map*

An analytical connection map was created to visualize how frequency shifts of within-region signal compartments linked to dominant signal compartments. This was performed by (1) arranging the dominant compartment frequency shifts on a frequency spectrum (set to a loose range so as to include all values), (2) plotting volume fraction weighted circles of within-region compartment frequency shifts on the frequency spectrum, (3) linking the within-region compartment frequency shifts to their respective brain regions, and (4) ordering the brain regions by minimizing the path length of their connections. This analysis was performed using Adobe Illustrator® CC 2015 (Adobe Systems, San Jose, CA, USA).

2.2.8 *Generating volume fraction maps based on compartment frequency shifts*

We aimed to validate the results of our data driven analysis (e.g. AIC model selection and k-means clustering) by mapping the voxel occupancies of the dominant signal compartments. The dominant compartment frequency shifts were chosen because they represent the broad underlying signal features of within-region signal compartments. A five-compartment complex-valued signal model, with fixed frequency shifts corresponding the five dominant frequency shifts (Fig. 2), was fitted to each complex valued voxel signal. Formulation of signal compartments and the optimization procedures remained the same as outlined in the previous section. For the ease of data presentation and utilizing this analysis primarily as a validation measure, representative image slices for each ROI were chosen from only one participant. Choosing slices from only one participant also demonstrates the practical utility, potentially for clinical use, of signal compartments in probing tissue properties on a case-by-case basis.

2.3 Results

2.3.1 *Evaluating temporal trends in the mGRE signal*

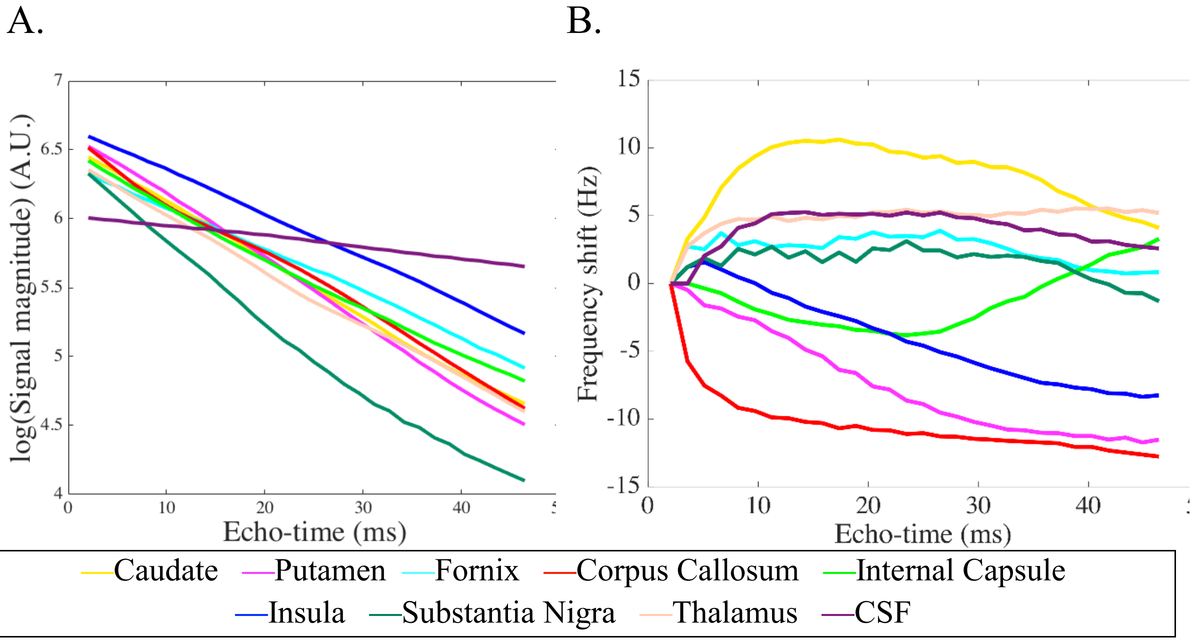

Fig. 2. Shown are (A) signal magnitude and (B) frequency shift as a function of echo time for the nine brain regions investigated. Values shown are based on averaging voxel signals in each region-of-interest and then averaging across participants. For each region, the first echo frequency shift value was subtracted to aid interpretation of results.

Fig. 2A shows the signal magnitude as a function of echo time for the nine regions investigated. Results are shown when voxel values, within respective regions, have been averaged for each individual and averaged across participants. Signal magnitude values have been plotted on a log scale, implying that in the case of mono-exponential signal magnitude decay governed by the T_2^* of individual regions, the curves should be linear. The best level of linearity was achieved for the CSF (residual of linear fit = 0.034), whilst other regions depict a level of non-linearity (residual of linear fit for caudate = 0.083, putamen = 0.071, fornix = 0.076, corpus callosum = 0.17, internal capsule = 0.13, insula = 0.047, substantia nigra = 0.38, thalamus = 0.094). These results suggest the presence of multiple signal effects which lead to a deviation from mono-exponential signal magnitude decay. Notably as well, the shape of the curves differ as a function of brain region, implying different effects are likely contributing to the signal in different brain regions.

In Fig. 2B the computed temporal frequency shifts for each brain region are depicted. The variability in the frequency shift curves as a function of echo time is larger than what can be observed in the signal magnitude (compare to Fig. 2A). For example, the substantia nigra had the highest amount of deviation from linearity for the signal magnitude, whereas its frequency shift does not vary as much in comparison to other regions. This observation suggests different underlying signal influences may potentially be influencing temporal trends in signal magnitude and frequency shift.

2.3.2 *Quality of fit measures and information criteria indicate unique multi-compartment models for different brain regions*

Table 2
ROI fitting results for one to six compartment models assessed via the standard error of regression (SER). Normalized SER plateau points for the complex signal, in bold, were utilized to informally assess the maximum number of signal compartments within each ROI. SER metrics for the magnitude and phase, in italics, are presented to elucidate the effects of increasing model complexity on quality-of-fit for respective GRE-MRI signal compartments.

	SER (%)					
No. of compartments	1C	2C	3C	4C	5C	6C
Caudate	19.3	12.7	**7.4**	6.6	6.3	5.0
Putamen	28.6	12.9	9.6	**7.9**	7.4	6.4
Fornix	12.2	6.8	6.8	**3.8**	3.8	3.7
CC	12.3	7.8	**3.9**	3.2	3.0	2.9
IC	22.7	13.1	**3.7**	3.7	2.4	3.3
Insula	28.9	13.2	11.3	9.1	8.6	7.6
SN	8.5	7.1	**4.6**	3.8	3.6	2.9
Thalamus	4.4	3.6	3.2	**2.2**	2.1	1.9
CSF	15.0	**10.3**	9.2	9.1	9.1	9.1

The temporal complex signal for each region was fitted using one to six compartment models, and the standard error of regression (SER) was calculated respectively (referred to as ‘Complex’) (see Table 2). By increasing the number of signal compartments, the quality-of-fit improved, as indicated by the ‘Complex’ SER values for each compartment model; of note, the SER for the complex signal was set as the cost function in the optimization algorithm. The bold face values indicate the compartment model where less than 5% improvement was achieved with respect to the SER value obtained for one compartment. Nonetheless, SER values decrease with the use of a larger number of signal compartments.

Table 3
Results from the one (1C) to six (6C) compartment model AIC analysis for each brain region-of-interest investigated. The smallest AIC value, used for model selection, is in bold face.

	Number of compartments					
	1C	**2C**	**3C**	**4C**	**5C**	**6C**
Caudate	110	103	**95**	103	121	149
Putamen	121	104	**103**	109	126	157
Fornix	98	**86**	93	89	108	141
CC	99	90	**79**	85	103	134
IC	114	103	**77**	88	96	127
Insula	127	**110**	113	118	136	168
SN	81	80	**75**	81	99	127
Thalamus	69	**67**	71	72	90	121
CSF	105	**98**	102	113	132	166

In Table 2 we used an arbitrary cut-off, related solely to improvements in the quality-of-fit measure, from which the likely number of signal compartments was estimated; in Table 3, however, the AIC was used to reduce the bias introduced through increased model complexity. The AIC analysis suggests the presence of more than one signal compartment for all regions investigated (see Table 3). Two signal compartments were identified for the fornix, CSF, insula and thalamus regions. Three signal compartments were selected for the caudate, putamen, corpus callosum, internal capsule and substantia nigra. Overall, the AIC selection process led to a more stringent cutoff for model selection than the SER selection process. In the fornix, for example, the SER plateau value suggests the presence of four signal compartments, whereas the AIC analysis suggests two. Overall, it is interesting to note how the quality-of-fit parameters vary as a function of number of compartments fitted and the differences in regional compartmentalization which arise when different model selection criteria are implemented.

2.3.3 *Cluster analyses reveal dominant inter-region signal compartments*

Within the sample of AIC-selected signal compartment models, we were able to identify five compartment frequency shift clusters across all brain regions considered. Results from the SI analysis indicated the presence of five clusters within the AIC-selected compartment frequency shift pool (Table 4). Fig. 3 elucidates the clustering of compartment frequency shifts, wherein the coloured points correspond to the frequency shifts extracted from all AIC-selected models and the thick line identifies their respective cluster centroids. Overall, the compartment frequency shift clusters within the AIC-selected signal models represent the "dominant" components of the mGRE-MRI signal phase across the nine regions considered; as such, these clusters are herein referred to as 'dominant frequency shifts', each of which correspond to a 'dominant signal compartment'.

Table 4
Mean Silhouette (SI) values for AIC-selected compartment models.

No. of clusters	Mean SI
1	N/A
2	0.77
3	0.76
4	0.83
5	**0.84**
6	0.81
7	0.84
8	0.82
9	0.86
10	0.83

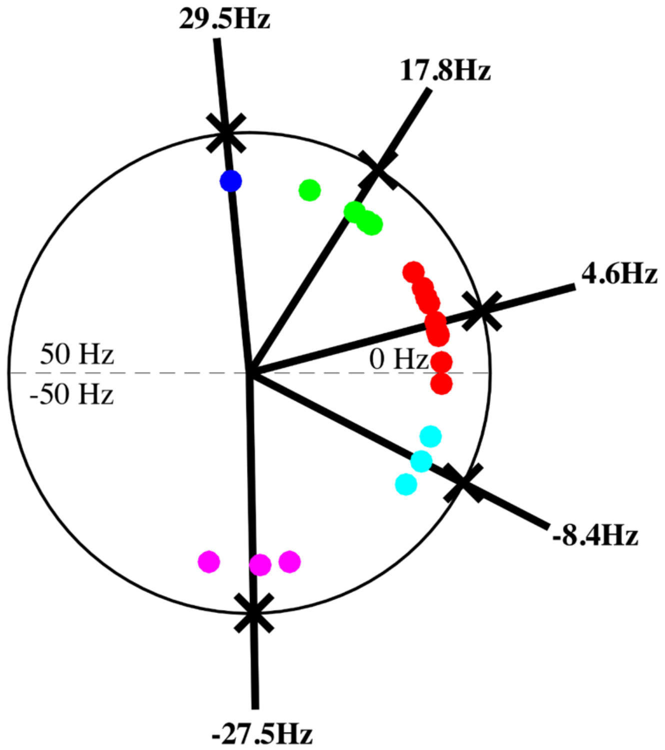

Fig. 3. Clustering results obtained using the AIC-selected signal compartment frequency shifts. Distinct frequency shift clusters are identified using different colours, and cluster centroid values are displayed as radial lines intersecting the circle at points marked by the cross.

Table 5 provides individual parameter values obtained using the AIC-selected compartment models. These results are illustrated in Fig. 4 to help understand how region-specific signal compartments distribute across other brain regions as a function of frequency shift and respective volume fraction. The location of the circles along the abscissa show how closely each region's compartments overlap with compartments from other brain regions. The ordinate is used to show the volume fraction, or size occupied by the compartment within a given region. Furthermore, the brain regions are arranged from left to right by minimizing the total path length of each regions' horizontal (weighted by frequency) and vertical (weighted by volume fraction) compartment linkage arbors. For example, two compartments have been identified for the CSF, the primary compartment (86%) near 4.6Hz dominant frequency shift, accompanied by a smaller compartment (14%) near -17.8Hz dominant frequency shift. In certain brain regions, such as the substantia nigra, multiple signal compartments co-localize around the same dominant frequency shift (36% at 5.0Hz and 32% 7.0Hz, both around the 4.6Hz centroid). For other regions, such as the caudate, individual signal compartments were associated with unique dominant frequency shifts (25% near -17.8Hz, 56% near -4.6Hz, and 19% near 29.5Hz; refer to Table 5).

Table 5
Estimated parameters for AIC-selected signal compartment models for each brain region. Frequency shifts have been highlighted using bold face, and volume fraction of each compartment is expressed as a percentage. Compartments are ordered from largest to smallest volume fraction occupied.

	A_1	ΔF_1 (Hz)	A_2	ΔF_2 (Hz)	A_3	ΔF_3 (Hz)
IC	71%	**-11.0**	22%	**-24.1**	7%	**17.8**
CC	37%	**1.0**	32%	**8.1**	31%	**-31.5**
Fornix	86%	**-5.9**	14%	**6.6**		
Insula	52%	**-8.4**	48%	**4.7**		
Thalamus	51%	**3.5**	49%	**-1.0**		
CSF	87%	**3.6**	13%	**16.1**		
Caudate	56%	**9.7**	25%	**22.1**	19%	**-26.8**
SN	36%	**3.4**	33%	**17.5**	32%	**7.2**
Putamen	48%	**3.9**	27%	**15.6**	25%	**29.5**

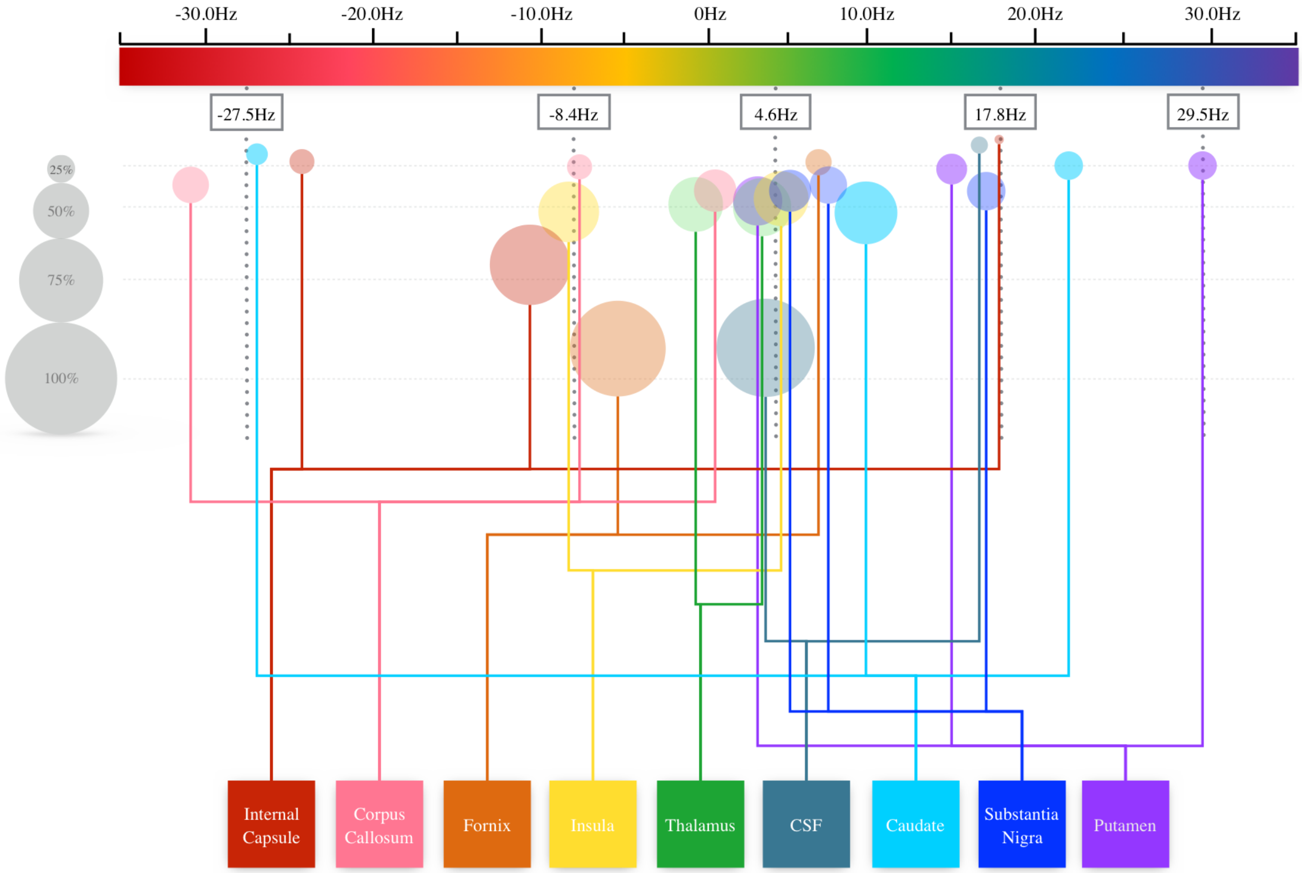

Fig. 4. A connection map of compartment frequency shifts and volume fractions for the nine brain regions studied. The AIC-based centroids identified using cluster analysis are shown on the frequency axis, and the size of the compartments represented using different sized circles are presented vertically; the size of all circles directly correlate to the respective volume fraction values (‘A’ value) for each region from Table 5. Each region has been connected to their respective compartment frequency shift values. The regions have been arranged in order to minimize the number of overlapping lines, only to help with the visualization of signal compartment volume fractions and their frequency shifts.

2.3.4 *Volume fraction maps of dominant signal compartments*

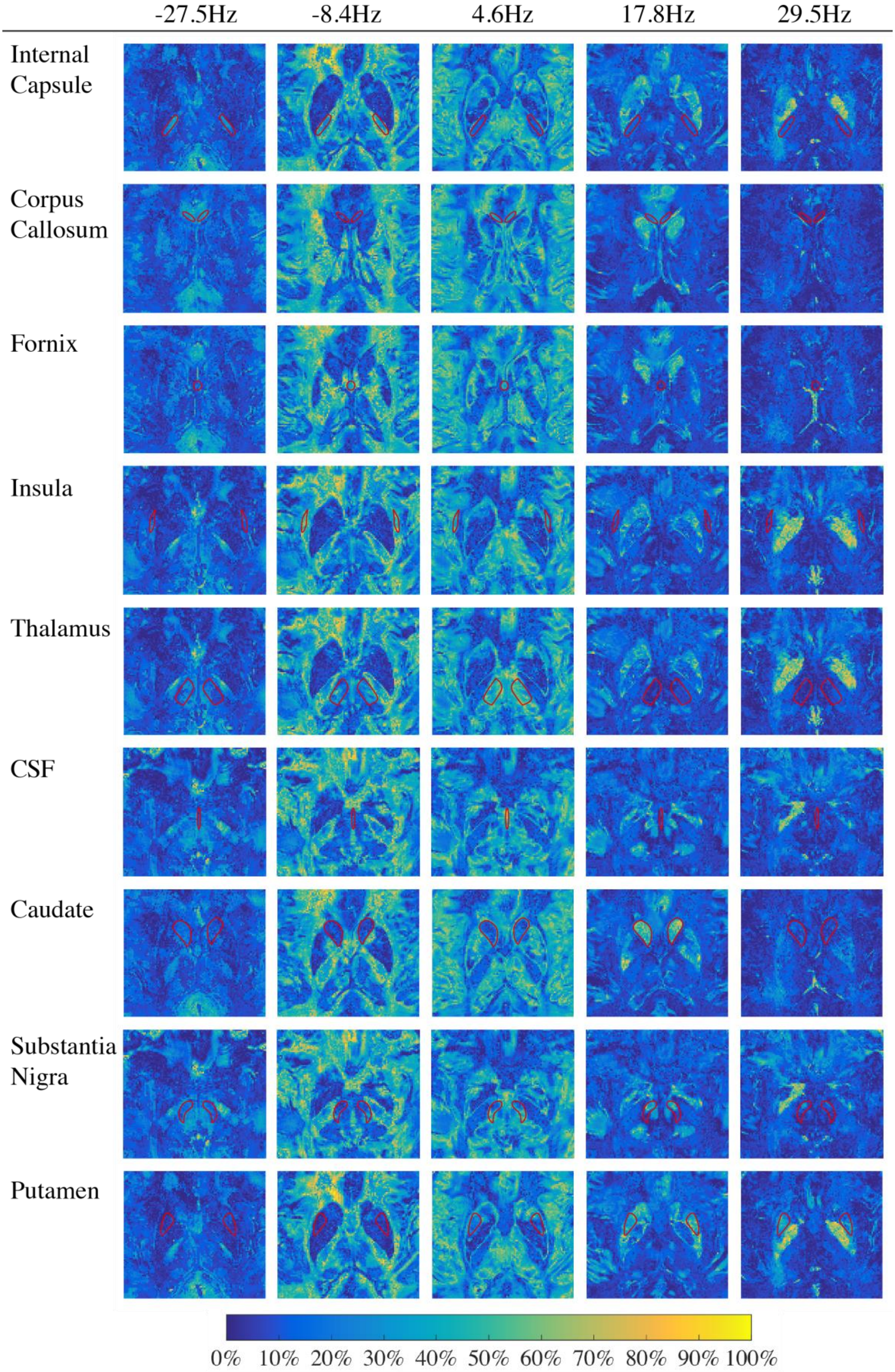

Fig. 5. Voxel-wise parametric mapping of dominant (AIC-selected) signal compartment volume fractions. Representative axial slices for each ROI, marked by the area inside the red outlines, were chosen for mapping based on best structural visibility. A gradient colour bar is displayed at the bottom for volume fraction quantification.

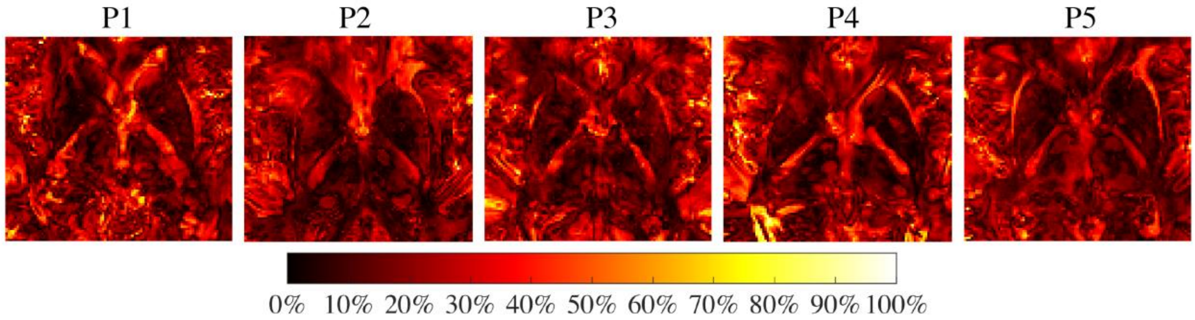

Fig. 6. Error distribution for volume fraction maps in five study participants (P1—P5). SER values for each voxel fit were normalized to the highest SER value within representative slices of similar anatomical location, and are presented as a percentage for interpretive benefits.

Fig. 5 shows spatially resolved volume fraction maps of the dominant signal compartments. Within each image slice, ROIs used in the region-wise analyses are delineated using a red outline (Fig. 5). Areas with a high volume fraction for individual signal compartments are represented by a yellow hue, while an absence of respective compartments can be discerned from the transition to a blue hue. For example, the -8.4Hz signal compartment appears to be a primary contributor across all the regions investigated, while the -27.5Hz compartment is the weakest contributor. We also observe a close correspondence of the analytically calculated within-region compartment model parameters (refer to Table 5) to the spatial distribution of signal compartments across gray and white matter regions (Fig. 5). For example, in the putamen, we observe three signal compartments with frequency shifts at 3.6Hz, 15.9Hz, and 29.5Hz; these signal compartments fall within the respective dominant signal frequency shift clusters of 4.6Hz, 17.8Hz, and 29.5Hz. When inspecting the volume fraction maps for this region, we observe a high degree of localization corresponding to the three dominant signal compartments (Fig. 5). A similar correspondence of model-based parameters to volume fraction maps can be observed in white matter regions, such as the internal capsule. The signal compartment with the highest volume fraction in this region falls within the -8.4Hz dominant frequency shift cluster (Fig. 4); this result corresponds to a high representation of the -8.4Hz dominant signal compartment, as displayed in Fig. 5. The other two signal compartments in this region, with frequency shifts of -24.1Hz (22%) and 17.8Hz (7%) corresponding to the -27.5Hz and 17.8Hz dominant frequency shifts, also display regional localization, but to a lesser degree than the highest volume fraction compartment (compare Table 5 and Fig. 5). This analytical-to-mapping correspondence can also be observed within the CSF. The largest within-region compartment frequency shift, resolved at 3.6Hz (87%) (Table 5), falls within the 4.6Hz dominant frequency shift cluster; this dominant frequency shift exhibits a notably high volume fraction within the CSF (Fig. 5).

Normalized SER distributions for voxel-wise volume fraction estimation are displayed in Fig. 6 for all five participants (P1—P5). Of note, the fitting error distributed similarly across all participants and a low fitting error was present within the corpus striatum (caudate, putamen, and globus palldius), whilst higher errors were present in surrounding structures. Interestingly, these surrounding structures are generally classified as white matter structures. Located anterior to the corpus striatum is the genu of the corpus callosum, while the internal capsule lies posterior to the corpus striatum. Furthermore, the external capsule lines the corpus striatum laterally, while the fornix joins them medially. Lastly, the error distribution within the cortical areas do not seem to obviate localization to any particular structure, but nonetheless remain higher than sub-cortical regions.

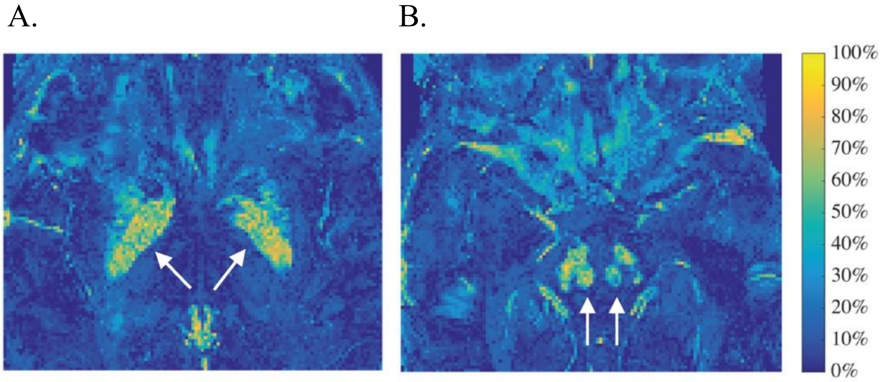

Fig. 7. Localization of high frequency (29.5Hz) signal compartment in the globus pallidus (A) and red nucleus (B), as indicated by the tailed arrows.

Through the voxel-wise volume fraction mapping method, we identified two sub-cortical areas which exhibited an apparent image contrast and remarkably high volume fraction of the 29.5Hz frequency shift compartment (Fig. 7). These areas delineate clearly (A) the globus pallidus and (B) the red nucleus, as indicated by the tailed white arrows. Interestingly, neither of structures were considered within our ROI selection.

2.4 Discussion

We explain temporal variations in mGRE-MRI data acquired at 7T using complex-valued signal compartments, and explore the utility of susceptibility-based signal compartments to probe tissue properties in the brain. By implementing information criteria and cluster analyses, we identified five dominant signal compartments shared across the mixture of gray (caudate, putamen, insula, thalamus, substantia nigra) and white (corpus callosum, internal capsule, and fornix) matter regions investigated and CSF. By fixing the frequency shift parameter for each dominant signal compartment in a voxel-wise fitting procedure, we (1) generate frequency-based volume fraction maps, and (2) demonstrate the generalizability of the dominant signal compartments across the healthy participant cohort.

2.4.1 *Observing trends in the temporal mGRE signal*

Upon plotting the temporal GRE complex signal, we observe a larger variance in the temporal frequency shift in comparison to the signal magnitude (refer to Fig. 2). These observations extend recent findings which suggest that echo-time dependent changes in magnetic susceptibility, sensitive to local shifts in the Larmor frequency, contain information on tissue properties. Furthermore, the enhanced sensitivity of signal phase to magnetic susceptibility effects at high field strengths underscores the importance of utilizing signal frequency shifts to characterize signal compartments and explore underlying tissue properties (Duyn et al., 2007; He and Yablonskiy, 2009; Marques et al., 2009; Schweser et al., 2011b, 2011a; Zhong et al., 2008).

2.4.2 *Evaluating signal compartments in a data driven framework*

The intricate system of influences which underlie the bulk susceptibility signal elucidates the necessity for a data-driven method of signal compartmentalization. Aside from an early study which implemented complex-valued signal compartmentalization to map water fat separation (Hernando et al., 2008), almost all subsequent compartmentalization studies implement the fitting procedure to suit the three-pool model (Li et al., 2015; Nam et al., 2015; Sati et al., 2013; Wu et al., 2017). The first notable limitation of this approach is the failure to consider the multitude of underlying signal effects (e.g. protein concentration, tissue iron, calcium, chemical exchange and diffusion), thus confining the utility of signal compartments to the investigation of tissue microstructure in white matter regions, primarily for myelin water fraction (MWF) imaging. Secondly, MWF studies that utilize signal compartmentalization introduce bias into the fitting procedure by applying conditional parameter constraints. For example, frequency shifts in the ‘extracellular’ tissue domain are commonly assumed to be zero (Alonso-Ortiz et al., 2017; Nam et al., 2015; van Gelderen et al., 2012; Wu et al., 2017); this approach is confounded due to a failure to consider the aforementioned signal influences. The magnetic properties of the extracellular space have been compared to CSF in other MWF studies (Li et al., 2015). The frequency shift we observe in CSF, alongside Straub et al.’s (2017) recent findings, further elucidate a discrepancy in the prior assumption ascribed to the null signal effects of extracellular tissue (refer to Table 5 and Fig. 5).

Conditional constraints on the transverse relaxation rate, as it relates to the separability of myelin and axonal compartments, have been utilized to resolve and characterize signal compartments (Lancaster et al., 2003; Nam et al., 2015; Wu et al., 2017); this would indeed bias the convergence of model parameters towards the given condition. For example, in an early study which adapted the three-pool model for myelin quantification, the authors calibrate relaxation rates for myelin and axonal compartments to align myelin fractions with previously published values and conditionalize a 10% increase for T_2 values assigned to extracellular water pools (Lancaster et al., 2003). Similar implementations have been adopted in more recent studies by including the effects of static magnetic field inhomogeneities (T_2^*) (Nam et al., 2015; Wu et al., 2017). Estimating model parameters and characterizing signal compartments based on highly variable prior information, such as the spin-spin relaxation properties of tissue, can lead to unreliability. For example, T_2 relaxation rates for myelin water and axonal water have been reported anywhere from 10ms to 70ms and 40ms to 80ms, respectively, wherein the static magnetic field strength across these studies varied only between 1.5T and 3T (Lancaster et al., 2003; Menon et al., 1992; Stewart et al., 1993; Wachowicz and Snyder, 2002; Whittall and MacKay, 1989).

Model selection plays an important role compartmentalizing the GRE signal, given the potential for Type I and Type II errors to influence the outcome of optimized model parameters. In the current study, we adopt a data driven approach to identify the number of signal compartments within each region. In previous studies, quality-of-fit for the three compartment model was assessed based on the coefficient of determination statistic (R^2) (Li et al., 2015; Sati et al., 2013; Sood et al., 2017). This metric, however, is inappropriate for non-linear models (such as the complex-valued plane-wave formulation), due to the underlying assumption regarding error distributions. The R^2 value is calculated as such:

$$R^2 = 1 - \frac{RSS}{TSS} = \frac{\sum(y - \hat{y})^2}{\sum(y - \bar{y})^2}$$

Thus, it follows that the total sum-of-squares (TSS) must equal the regression sum-of-squares (REGS) plus the residual sum-of-squares (RSS) (TSS = REGS + RSS); a condition only assured in regressing linear models (Spiess and Neumeyer, 2010). This condition is not a requirement for standard error estimations (e.g. the standard error of regression analysis (SER), mean squared error (MSE), or root mean squared error (RMSE) of the regression). However, standalone interpretations of standard error estimations for non-linear models and linearized non-linear models suffer from a high case-to-case variance with increasing model complexity (Peddada and Haseman, 2006; Ruckstuhl, 2010). The Akaike information criteria has been shown to identify parsimony accurately, without requiring prior information, when evaluating the bias-variance tradeoff between non-linear models (Hurvich and Tsai, 1989; Snipes and Taylor, 2014; Vandekerckhove et al., 2014). Though analyses of SER provided an approximate measure of signal fit (Table 2), the Akaike information criterion implementation consolidated the point of maximum information capture (Table 3). Furthermore, the silhouette analysis and k-means clustering methods extracted dominant signal influences across the gray-white matter regions in an unbiased manner. Aside from the plane-wave model itself, we incorporate no prior information with regards to the number of signal compartments, and avoid using any conditional parameter constraints during the optimization process. The number of signal compartments was extended to six in order to ensure model parsimony was achieved, but limited to this number after observing optimal information gain at approximately half the maximal number (near three compartments) (refer to Table 3). Results from the AIC analysis largely validate the presence of three signal compartments; five out of nine regions investigated contained three signal compartments (caudate, putamen, corpus callosum, internal capsule, and insula; see Table 3). However, the AIC values for the CSF, thalamus, and insula, indicate optimal information gain with merely two compartments. The data driven method was implemented further to evaluate inter-regional trends in signal compartments by way of k-means cluster analyses.

When brain regions are arranged by minimizing the path lengths of connections, as in Fig. 4, an underlying microstructural pattern emerges in which the thalamus is in the centre.

As the nervous system’s primary relay centre for ascending and descending pathways (Sherman, 2016), a diverse regional cytoarchitecture can be assumed; a combination of paramagnetic and diamagnetic inclusions, as well as multiple fiber orientations could result in the low number of signal compartments resolved (refer to Table 3). The insula, caudate, putamen and substantia nigra vary significantly at a microscopic level (e.g. < 0.1 mm—receptor topography, dendritic arborization, neurofilament distribution, etc.); at a mesoscopic level (0.1 mm —1.0mm) however, they share similar structural elements. Typically identified as gray matter structures, these regions contain densely packed neuronal cell bodies, synaptic terminals, and weakly myelinated regions of the axon hillock (Purves et al., 1997). As a whole, these gray matter structures exhibit multiple within-region compartment frequency shifts around the dominant 17.6Hz and 4.6Hz signal compartments, and are grouped adjacently on the right side of the compartment relationship map (see Fig. 4). In contrast, the three white matter regions investigated (internal capsule, corpus callosum, and fornix) are grouped uniformly on the left side of the relationship map, exhibiting frequency shifts around the -27.5Hz and -8.4Hz dominant signal compartments (Fig. 4). These results extend prior findings which report a bulk diamagnetic susceptibility effect, measured as a reduced resonant signal frequency, within white matter regions (Duyn et al., 2007; Fukunaga et al., 2010; Lee et al., 2012). There exists convergent evidence amidst NMR biophysics literature (Hong et al., 1971; Morell and Quarles, 1999; O’Brien and Sampson, 1965; Rosenblatt et al., 1987) and structural MRI studies (Baxan et al., 2010; Duyn and Schenck, 2017; Koenig, 1991; Lee et al., 2012; C. Liu et al., 2011) to ascribe diamagnetic properties to myelin lipids, a defining tissue constituent of white matter structures (Purves et al., 1997). The overarching trend observed within the signal compartment relationship map suggests an underlying link between mesoscopic tissue properties and signal compartment frequency shifts.

The dominant frequency shifts ascertained from our data driven analysis allowed us to resolve volume fractions of identified mGRE-MRI signal influences (Fig. 5). Representative image slices for one participant were mapped to allow a ROI-based analysis of spatial distributions of dominant signal compartments. The error distributions, provided in Fig. 6, demonstrate a similar quality of voxel-wise fitting across all participants. This result validates the generalizability of the extent to which these dominant signal compartments influence the mGRE-MRI signal. Furthermore, this exercise validated our analytical evaluation of inter-region signal compartment trends (Fig. 4), and elucidated the utility of providing new quantitative contrast mechanisms for clinical and empirical purposes.

2.4.3 *Considering the biophysical origins of signal compartments and respective frequency shifts*

The biophysical sources of Larmor frequency shifts are manifold, and the results from this study demonstrate a highly complex system of contributions to the GRE-MRI complex signal. This complexity resonates throughout the previous literature, and is manifest in the form of contradiction. For these reasons, accurately characterizing signal compartments within individual brain regions, and their respective frequency shifts, would be confounded. However, rationalizing inter-region signal compartment frequency shifts (illustrated in Fig. 4 and resolved in Fig. 5) may be more robust to nuisance effects (e.g. orientation and noise) and informative of the dominant underlying signal influences. At large, these influences can occur as a result of local tissue microstructure, or a wide array of dynamic processes (e.g. chemical exchange, diffusion, blood flow, and neural activity). Early works ascribe the effects of tissue microstructure to the density and arrangement of non-heme iron, proteins (e.g. transmembrane proteins, metalloprotein complexes, cytoskeletal fibers, etc.), lipids (e.g. from endoplasmic reticulum, cell membranes, endosomal membranes, etc.), and de-oxyhemoglobin; these inclusions create tissue specific, inhomogeneous magnetic fields that affect resonant frequency of water molecules (Duyn et al., 2007; He and Yablonskiy, 2009;

Yablonskiy and Haacke, 1994). A comprehensive summary table of the underlying influences discussed in the following paragraphs is provided in Appendix Table 2.

One of the most well-characterized influences underlying susceptibility contrast is the presence of non-heme iron (Deistung et al., 2013; Drayer et al., 1986; Fukunaga et al., 2010; Haacke et al., 2007, 2007; Schenck and Zimmerman, 2004; Schweser et al., 2011b, 2012). Non-heme iron is typically found in the tissue parenchyma bound to ferritin complexes, or as its metabolite hemosiderin (Schenck and Zimmerman, 2004; Schweser et al., 2011b). The unpaired orbital electrons in both ferric (Fe^{3+}) and ferrous (Fe^{2+}) ions assign paramagnetic properties to non-heme iron, albeit more so to the latter form (Harrison and Arosio, 1996; Ke and Qian, 2007; Taiwo, 2003). Some of the highest concentrations of tissue iron have been reported in the basal ganglia regions (e.g. caudate, putamen, globus pallidus, and substantia nigra) (Aquino et al., 2009; Drayer et al., 1986; Hallgren and Sourander, 1958; Schweser et al., 2011). The largest positive frequency shift (29.5Hz) assigned to a dominant signal compartment coincidentally displays a high degree of localization within the putamen, substantia nigra, and nominally in the caudate (Fig. 5). A notably large representation of this signal compartment can be observed within two brain regions that were not considered in this study, the globus pallidus and red nucleus (Fig. 7). Both of these regions are well characterized for high concentrations of non-heme iron during physiological conditions (Aoki et al., 1989; Aquino et al., 2009; Hallgren and Sourander, 1958; Schweser et al., 2011b; Zecca et al., 2004). These findings strongly suggest the 29.5Hz signal compartment reflects the paramagnetic influence of non-heme tissue iron.

Though non-heme iron in brain tissue is stored in the form of ferric iron, as the ferritin complex, the prevalent mechanism of iron translocation across the intracellular endosomal membrane requires the iron to be reduced into the ferrous form (Harrison and Arosio, 1996;

Ke and Qian, 2007; Qian and Shen, 2001; Zecca et al., 2004). In ferric iron, all electron orbitals contain unpaired electrons, whereas in ferrous iron, one electron orbital contains a full pair of electrons; due to the spatial occupancy of two like charges, a repulsive, or diamagnetic effect is created. This effect occurs only in one orbital; thus, the overall paramagnetic property is maintained, but slightly attenuated in ferrous iron. Interestingly, we observe a high volume fraction of the 17.6Hz signal compartment within and around the basal ganglia regions, namely the caudate, putamen, and substantia nigra (Fig. 5); these areas, as outlined earlier, are key regions for iron metabolism and storage. Taken together, the 17.6Hz could in fact reflect iron in its paramagnetically weaker, ferrous state. This observation is also analytically validated through the temporal fitting process; with respect to frequency shift maps, all three of the aforementioned regions (caudate, putamen, and substantia nigra) contain one compartment within the 17.6Hz cluster (refer to Fig. 4 and Table 3). Increasing densities of ferric iron, however, have been observed primarily within the context of ageing and disease. Since we are investigating brain images from healthy young adults (mean age: 34 years), we may be capturing the onset of oxidative ferric iron deposition, commencing in the corpus striatum.

Trace amounts of ferritin and transferrin bound iron have also been observed in the CSF (Khalil et al., 2014; Straub et al., 2017). We observe a minor signal compartment (13%) near the 17.6Hz cluster which could potentially reflect these iron complexes (see Fig. 5 and Table 3). However, upon close inspection of CSF's signal compartments, the bulk susceptibility signal is explained by one compartment with a substantially high volume fraction (3.6Hz; 87%). A recent study performed by Straub et al. (2017) found the CSF to be a stable and robust region for susceptibility referencing in healthy participants; the authors of this study report a volume susceptibility of 0.010ppm, corresponding to frequency shift of 3.0Hz at 7T.

The 3.6Hz frequency shift of the major signal compartment in CSF lies in close proximity to the 4.6Hz inter-regional frequency shift cluster (Fig. 4). When observing the volume fraction maps, the dominant signal compartment at 4.6Hz is localized to most gray matter regions, but is also sparsely distributed amidst white matter regions (Fig. 5). Distributed throughout CSF are dynamic quantities of salts, proteins and glucose; these ionic and macromolecular moieties could be captured collectively as a signal compartment, previously unobservable due to decreased sensitivity to susceptibility influences at lower field strengths (Alonso-Ortiz et al., 2017; Duyn et al., 2007; van Gelderen et al., 2012; Wharton and Bowtell, 2012). A lack of structural coherence amidst these inclusions, however, provide reason as to why this signal compartment exhibits the lowest magnitude of induced field change. It is important to note that this dominant signal compartment encompasses the largest number of within-region signal compartments (refer to Fig. 4). This comes to no surprise as water is the primary constituent of CSF (Sakka et al., 2011). Water, nutrients, electrolytes, and other vital constituents of CSF are absorbed into the brain by peri-cortical structures adjacent to the subarachnoid spaces, as well as the deep subcortical structures, such as the basal ganglia and limbic regions, adjacent to the first and second (or lateral) ventricles (Miyajima and Arai, 2015; Sakka et al., 2011). From the magnified volume fraction map of CSF, a high volume fraction of the 4.6Hz signal compartment can be observed within the medial ventricle; upon closer inspection, this compartment seems to emanate outside of the ventricular zone (Fig. 5).

Iron in the brain can also be bound to oxygen-containing metalloprotein complexes in the form of hemoglobin (Haacke et al., 2005; Lee et al., 2010a; Ogawa et al., 1990). The oxygenation state of hemoglobin plays a key role in hemoglobin’s susceptibility effect by changing from diamagnetic to paramagnetic upon the loss of bound oxygen to surrounding tissue (He and Yablonskiy, 2007; Ogawa et al., 1990). He and Yablonskiy (2009) incorporate this susceptibility difference into the Lorentzian sphere model and report values for de-oxyhemoglobin in the frontal lobe ranging from 0.21ppb to 0.90ppb (referenced to water); this corresponds to frequency shifts at 7T from 0.80Hz to 3.40Hz.

The presence of iron and myelin lipids in the brain are not entirely unrelated; oligodendrocytes, the principal cells that produce myelin in the CNS, stain for iron under normal conditions (Todorich et al., 2009). On average, 70-80% of myelin is composed of cholesterol, a principle lipid (Saher et al., 2005). In the presence of an external magnetic field, cylindrical tubules composed of radially oriented lipids exhibit a diamagnetic susceptibility in reference to de-ionized water (Hong et al., 1971; Rosenblatt et al., 1987). Under healthy conditions, a high density of neuronal fiber bundles in white matter regions makes these regions differentially sensitive to susceptibility effects originating from myelin lipids (Duyn and Schenck, 2017; Koenig, 1991; Lee et al., 2012; Luo et al., 2014). Numerous studies investigating susceptibility induced tissue contrast in the brain report negative signal frequency and signal phase in cortical and sub-cortical white matter regions containing heavily myelinated neuronal fiber bundles (Duyn et al., 2007; Duyn and Schenck, 2017; Langkammer et al., 2012; Lee et al., 2012; Szczepaniak et al., 2002). For example, Lee et al. (2012) validate the diamagnetic effects of myelin by reporting an observed reduction in tissue contrast, corresponding to an increased signal frequency, due to cuprizone induced myelin loss in the corpus callosum. The signal compartment frequency shifts we observe within the white matter regions investigated in our study further validate the diamagnetic property of myelin lipids; signal compartments in the internal capsule, corpus callosum and fornix exhibit heavy clustering around the -8.4Hz and -27.5Hz frequency shift centroids, with the volume fractions being weighted more to the former centroid (see Fig. 4). Furthermore, when observing the volume fraction maps, the -8.4Hz compartment exhibits high volume fractions within the internal capsule, corpus callosum and fornix, and also globally throughout all white matter regions (Fig. 5).

The presence of myelin is suggested to engender distinct microscopic water environments, each with unique signal relaxation properties, due to differences in within-pool exchange and between-pool proton exchange rates. This biophysical theory of tissue microstructure in white matter brain regions has resulted in the three-pool, or three-compartment model; namely myelin water, axonal water, and extracellular water compartments (Alonso-Ortiz et al., 2017; Du et al., 2007; Hwang et al., 2010; Lancaster et al., 2003; Nam et al., 2015; Sati et al., 2013; Wu et al., 2017). Concomitantly, two recent studies that implemented the three-pool model report frequency shifts for the compartment assigned to axonal water within a comparable range of the -8.4Hz dominant signal compartment. Sati et al. (2013) report axonal water frequency shifts at -6.0Hz in the optical radiatum and -4.1Hz in the splenium of the corpus callosum; frequency shifts in the same range -6.3Hz in the optical radiatum and -6.5Hz in the splenium of the corpus callosum) were observed in a following study performed by Li and colleagues (2015). Sati and colleagues (2013) also found that axonal water and myelin water frequency shifts are close when white matter fibers are oriented near parallel to the scanner field. They found the fast relaxing signal compartment associated with myelin water to have a frequency shift of -5.4Hz. For fibers oriented approximately perpendicular to the scanner field, axonal water frequency shifts ranged between -4.1Hz to -6.9Hz. Thereby, orientation of myelin microstructure with respect to the scanner field can result in changes in the axonal water frequency shift. In addition, our results align with previous studies which report negative echo-time dependent frequency differences in orientation dependent white matter structures (Duyn et al., 2007; Duyn and Schenck, 2017; Lee et al., 2012; C. Liu et al., 2011; Wharton and Bowtell, 2012). Overall, our results align with previous studies which report negative echo-time dependent frequency differences in orientation dependent white matter structures (Duyn et al., 2007; Duyn and Schenck, 2017; Lee et al., 2012; C. Liu et al., 2011; Wharton and Bowtell, 2012). 2012

Lipids and proteins play complementary roles in comprising the fundamental cytoarchitecture for neurons. Cerebrosides, cholesterol, and a host of other lipids embed diamagnetic proteins (e.g. surface receptors and ion channels) into cellular and sub-cellular biological membranes, while a lattice of polypeptide chains form the cytoskeletal fibers that provide the core structure for neurons (Morell and Quarles, 1999; Yuan et al., 2012). Akin to lipids, the two main factors which could influence protein related phase contrast stem from magnetic susceptibility and chemical exchange; the structured neurofilaments could contribute to the bulk susceptibility effect, while the membrane embedded proteins would undergo chemical exchange with the surrounding tissue parenchyma. In an early study by Hong et al., (1971), rhodopsin, a G-protein-coupled receptor (GPCR) was reported be the primary constituent for orientation dependent magnetic susceptibility effects in rod cells, in comparison to phospholipid molecules. Recent studies extend these findings by reporting diamagnetic susceptibility properties for proteins in gray and white matter brain regions (referenced to CSF), ranging on the order of parts per billion (ppb) in the susceptibility domain and Hertz (Hz) in the frequency domain, at 7T (He and Yablonskiy, 2009; Leutritz et al., 2013; Luo et al., 2010; Zhong et al., 2008). Taken together, the –25.9Hz dominant signal compartment could in fact reflect the bulk susceptibility effect arising from the microscopic arrangement of proteins the brain (Fig. 5). The bulk diamagnetic susceptibility effects of lipids and proteins, however, were reported to field effects of similar magnitude, but in the opposite direction, in comparison to chemical exchange effects (Leutritz et al., 2013). Thus, though the bulk susceptibility effect of proteins could be potentially observed via signal compartmentalization, however image contrast may be attenuated in the volume fraction maps due to field averaging chemical exchange effects.

2.4.4 *Methodological considerations*

A major challenge for studies which aim to investigate tissue microstructure is removing the confounds of non-local field effects. Quantitative susceptibility mapping has established itself in addressing this issue, and was consequently incorporated in our data processing pipeline (Haacke et al., 2015; Kee et al., 2017; Li et al., 2011; Reichenbach et al., 2015; Schweser et al., 2012; Wang and Liu, 2015). In addition to the general limitations posed to MRI image processing (e.g. motion correction, flow compensation, etc.), the current approach confers the confounds associated with the overall QSM process, as well as the specific susceptibility pipeline (e.g. STI Suite) utilized.

Contextualization of the biophysical effects of myelin on the measured signal can be confounded by the radial susceptibility anisotropy which results from the molecular arrangement of glyco— and phospholipids with respect to the static magnetic field (He and Yablonskiy, 2009; Lee et al., 2017; Li et al., 2012; Liu, 2010; Wharton and Bowtell, 2012; Xu et al., 2017). Both the anisotropy of tissue and susceptibility could explain the high fitting error observed in white matter structures surrounding the corpus striatum (Fig. 5). This result falls in line with previous reports of high structured errors in white matter regions, arising from the effects of tissue and susceptibility anisotropy on signal frequency dispersion (Alonso-Ortiz et al., 2017; Lee et al., 2017; van Gelderen et al., 2012; Wharton and Bowtell, 2012; Yablonskiy and Sukstanskii, 2017). The effects of susceptibility anisotropy in human white matter brain regions have been quantified within the range of 0.012ppm (Lee et al., 2012) to 0.022ppm (Li et al., 2012) yielding frequency shifts of 3.6Hz to 6.6Hz at 7T, respectively. Though multi-angle acquisitions were not implemented in our approach, our data-driven approach results in a distribution of frequency shifts around the dominant inter-region signal compartments (refer to Fig. 6).

The sign conventions utilized to characterize the signal phase during signal acquisition and post-processing steps also play an important role in characterizing susceptibility effects. Hagberg et al. (2010) demonstrate the dependence of signal phase sign conventions on the coordinate system in which phase information is mapped. For example, examining the signal frequency in the rotating frame of reference would yield a positive frequency shift for spins accelerated in the counter-clockwise direction, whereas in the complex frame of reference (also known as the Argand plane), acceleration in this direction would yield a negative frequency shift. Thus, analytical frame of reference should also be carefully considered when processing and modelling the complex mGRE signal, as well as interpreting the magnetic properties of resulting signal compartments.

The conversion of the temporal frequency shift from susceptibility values is also a question of debate. In the only other study implementing tissue susceptibility into the signal compartmentalization method, susceptibility values were converted to frequency shifts by way of the Lorentzian sphere approximation (Wu et al., 2017). In our study, we opted to calculate tissue frequency shifts from the apparent susceptibility effects observed at the voxel scale (Schweser et al., 2011b, 2016). This approach assumes no specific shape effect of the dipole field generated and internal frequency shift induced at a microscopic level; rather, the bulk susceptibility effects of all underlying signal influences are probed at the meso-macroscopic (0.5mm – 1 mm) interface and consequently discretized as individual signal compartments.

Modelling data over smaller echo times, with larger data points, and in a larger participant sample would assist in improving the accuracy and precision of model parameter estimation. Exploring ex-vivo histology and microscopy procedures would also be necessary validate the biophysical underpinnings of signal compartments. We invite future research to tackle the aforementioned issues and extend our findings to develop imaging biomarkers sensitive to micro-scale changes within an MRI voxel.

2.5 Conclusion

We explain variations in mGRE-MRI data using complex-valued signal compartments, and explore the utility of signal compartments to probe tissue properties in the brain. The overall results from this study suggest the presence of five dominant signal compartments distributed differentially across the mixture of gray and white matter regions investigated. Furthermore, the frequency shift signatures exhibited by these signal compartments inform tissue properties through parametric mapping of their respective voxel occupancy. Our approach highlights the importance of information based multi-compartment signal modelling, in comparison to the traditional three-compartment method, for unbiased extraction of features from temporal GRE-MRI data. Such an approach may be used to systematically investigate micro-scale influences on the GRE-MRI signal, and assist in identifying parametric biomarkers of neural tissue properties in physiological and pathological conditions.

Chapter 3: Exploring echo-time dependent trends in GRE-MRI at 3T and 7T

3.1 Introduction and Aims

Sood et al. (2017) previously found that QSM values change as a function of echo time in a manner that differs between brain regions. The non-linear relationship between QSM values and GRE-MRI echo time can be explained by compartmentalising the voxel signal (Chen et al., 2013; Sood et al., 2017; Wu et al., 2017). While QSM and signal compartmentalization can be performed and applied at 1.5T and 3T, significant gains in sensitivity to tissue related field effects (e.g. susceptibility, exchange, diffusion, etc.) can be achieved with the use of ultra-high field strength measurements, e.g. using 7T GRE-MRI data (Bilgic et al., 2012; Deistung et al., 2008; Duyn, 2012; Duyn et al., 2007). The increased availability of ultra-high field human scanners (e.g. 7T) make available increased levels of signal-to-noise ratio (SNR), yielding improved visualization of small anatomical regions (Bourekas et al., 1999; Cho et al., 2011; Dumoulin et al., 2017; Duyn et al., 2007; Lodygensky et al., 2012). Beyond SNR gains, static field increases enhance sensitivity to local magnetic field perturbations induced by variations in tissue composition and structure (Abduljalil et al., 2003; Deistung et al., 2008; Duyn, 2017; Reichenbach et al., 1997; Schenck and Zimmerman, 2004). This can be observed by referring to the Larmor equation, wherein the measured signal frequency, ω, is a function of the gyromagnetic ratio (γ) and the static magnetic field strength (B_0),

$$\omega = \gamma B_0.$$

Further, changes in the static magnetic field (ΔB_0) would be encoded as a shift in the measured signal frequency ($\Delta\omega$),

$$\Delta\omega = \gamma \Delta B_0.$$

Magnetic susceptibility (denoted as χ) induced perturbations in the static magnetic field could be expressed as,

$$\Delta B_0 = \chi B_0.$$

This allows shifts in the Larmor frequency to be expressed as function of magnetic susceptibility;

$$\Delta\omega = \gamma\chi B_0.$$

Consequently, at higher field strengths, the induced frequency shifts increase in magnitude and allow for improved encoding of tissue related field perturbations.

Though many aspects of ultra-high field imaging prove beneficial, the increased utility of 7T human scanners has engendered mixed reports in relation to temporal trends in the multi-echo GRE-MRI signal. In a recent study, for example, Cronin et al. (2017) ascribe echo time dependent variations in the GRE-MRI signal to a failure in phase unwrapping, particularly in areas of high susceptibility. However, this study was performed at 3T whereas Sood et al. (2017) used 7T data. Furthermore, an increasing number of studies within the domain of myelin water fraction imaging aim to characterize temporal trends in multi-echo GRE-MRI data through the use of multi-compartment signal models. What began as a magnitude-based fitting procedure on GRE-MRI data acquired at 3T (Du et al., 2007; Hwang et al., 2010) has evolved through the use of complex-valued model parameters to fit GRE-MRI complex data (magnitude and phase) in the 7T regime (Li et al., 2015; Sati et al., 2013; Wu et al., 2017). Signal compartments expressed in complex form have also been utilized in 3T GRE-MRI data (Nam et al., 2015). Consequently, relating parameter estimates, and subsequent mapping results (volume fraction, T_2^*, or Δf), across these studies remains confounded due to inherent signal differences in the field strength regimes.

To this end, we aimed to address two main questions. First, how are temporal trends in the GRE-MRI signal influenced by the static magnetic field strength; in particular, how comparable are 3T and 7T findings in different brain regions? Second, do GRE-MRI signal compartments reflect underlying variations in the GRE-MRI signal at different field strengths?

3.2 Methods

3.2.1 *Data acquisition*

The University of Queensland human ethics committee approved this study and written informed consent was given by six healthy participants (19, 30 and 60 year old males and 26, 33 and 47 year old females). 3D gradient recalled echo flow compensated scans were conducted on a 7T ultra-high field whole-body MRI research scanner (Siemens Healthcare, Erlangen, Germany) equipped with a single channel transmit and 32 channel receive head coil (Nova Medical, Wilmington, USA) using the following parameters: TE_1 = 4.98ms, echo spacing = 3.13ms, 9 echoes, TR = 52ms, flip angle = 15^o, voxel size = 0.75 × 0.75 × 0.75 mm, and matrix size = 242 × 280 × 160. The same participants were scanned using a 3T Siemens Magnetom Tim Trio scanner (Siemens Healthcare, Erlangen, Germany) using the product 32 channel receive head coil with TE_1 = 6.29ms, echo spacing = 5.26ms, 9 echoes, TR = 60ms, flip angle = 18^o, voxel size = 1 × 1 × 1 mm, and matrix size = 210 × 210 × 120. MP2RAGE data were acquired with the following parameters: TE = 3.44ms, TR = 4550ms, voxel size = 0.75 × 0.75 × 0.75 mm, and matrix size = 300 × 320 × 256 at 7T. We used monopolar readout for both 3T and 7T acquisitions. Echo times for the 3T and 7T GRE-MRI data took into account the reduction in T_2^* at 7T compared to 3T, thus resulting in different echo times for 3T and 7T acquisitions. The same number of echoes were acquired at both field strengths. To allow for direct comparison of temporal trends between both 3T and 7T data, we refer to echo points rather than echo times in our results.

3.2.2 *Signal processing*

The 32 channel 3T GRE-MRI data were combined on the scanner as a body transmit coil was used during the data acquisition. Since a 7T body coil is not available, the 32 channel 7T GRE-MRI magnitude and phase data were processed as previously described (Vegh et al., 2016). Magnitude images were used to create a mask using the brain extraction tool in FSL (FMRIB, University of Oxford) (Smith, 2002). Signal phase processing (unwrapping and background field removal), QSM calculations, and temporal frequency shift profiles were generated and performed as outlined in Ch. 2, Sections 2.2.2 – 2.2.4 (QSM pipeline summarized in Fig. 1).

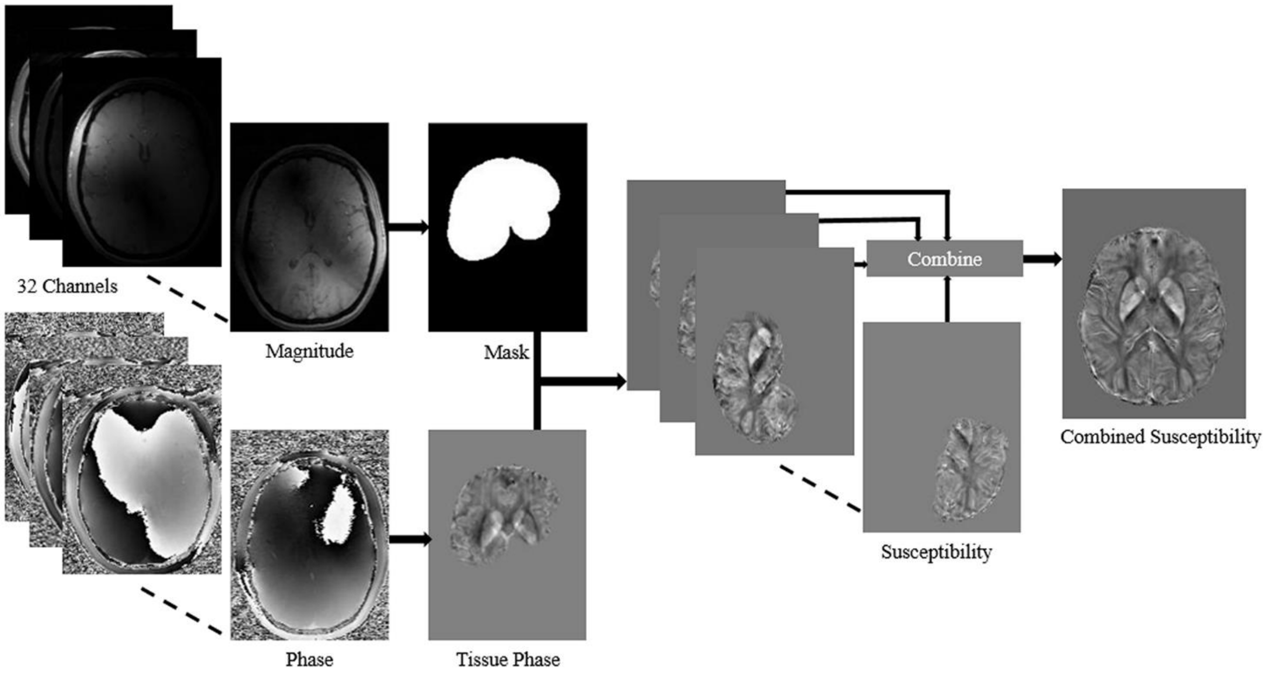

Fig. 1. The pipeline used to compute quantitative susceptibility maps. Individual channel data were processed using STI Suite and combined into a single image at the very end. Susceptibility was then converted to a frequency shift value.

3.2.3 *Regions-of-interest*

3T GRE-MRI data were registered to the 7T GRE-MRI data using MIPAV (McAuliffe et al., 2001). FreeSurfer (V6, 2017) was used to segment individual brain regions using the 7T MP2RAGE data (Dale et al., 1999). Regions-of-interest (ROI) were eroded (using the erode function in FSL with a threshold between 80% and 90%) to reduce partial volume effects due to adjacent brain regions. MATLAB® (The MathWorks, Natick, MA, USA) scripts were used to extract region-based values and to produce frequency shift plots. Three ROI, namely the corpus callosum, cerebrospinal fluid (CSF), and putamen were specifically chosen for their unique microstructural properties and influences on the GRE-MRI complex signal. From our analysis in Ch. 2, we identified the corpus callosum and putamen to lie on opposite sides of the frequency shift spectrum, with the CSF aligning approximately in the centre (Section 2.3.3, Fig. 4). In observing these differential effects on the signal frequency, we focused on characterizing the temporal frequency shift profiles between these regions, wherein respective regions broadly represent gray matter (putamen), white matter (corpus callosum), and CSF. The first echo time signal was subtracted from all other echo time signals for the purpose of standardising frequency shift plots.

3.2.4 *GRE-MRI signal compartmentalization*

The GRE-MRI complex data were fitted to signal compartments using the same model and methods as outlined in Ch. 2, Section 1.2.5. To avoid over-fitting, we used our results from the AIC analysis in Ch. 2 (Section 2.3.2) to determine the number of signal compartments for each ROI. The standard error (SER) was calculated for each multi-compartment fit by summing the normalized residual squared errors (nSER) across all echo times.

3.2.5 *Generation of temporal magnitude and frequency shift plots*

Echo-time dependent variations in the signal magnitude were linearized on to a log-scale to more readily visualize inter-regional differences in T_2^*decay rates. A single compartment mono-exponential model was used to fit signal magnitude as a function of echo time for the purpose of evaluating how T_2^* values change as a function of field strength. At each field strength we also computed the average T_2^* and a measure of variation through the coefficient of variation (CoV) metric (calculated as $\frac{\sigma}{\bar{x}}$). Frequency shifts have been plotted as a function of echo point, since echo times do not directly align between 3T and 7T GRE-MRI data. Because the Larmor frequency is a function of magnetic field strengh ($\omega = \gamma B_0$), subsquent shifts in the Larmor frequency will be larger at higher field strengths ($\Delta f = \frac{\gamma B_0}{2\pi}$). To allow for direct comparison of temporal curves, 7T frequency shifts were scaled (via a multiplication of 3/7) to 3T; the scaled 7T temporal frequency shifts were labelled as $7T^{\#}$.

After compartmentalizing the complex signal, resulting compartment frequency shifts in 7T data were also scaled down to 3T to allow for a direct comparison; scaled frequency shfits were labelled $\Delta f_{7T}^{\#}$.

3.3 Results

3.3.1 *Variations in signal magnitude*

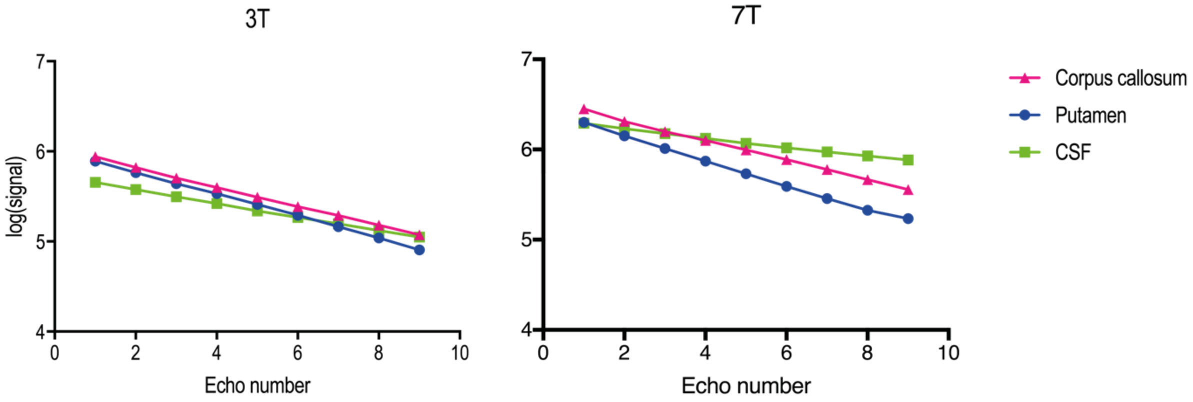

Fig. 2. Shown are the signal magnitudes at 3T and 7T plotted over a log scale for the three regions investigated. Temporal variations seem more pronounced in 7T data in comparison to 3T data.

Fig. 2 displays echo-time dependent variations in the signal magnitude plotted on a log scale. Upon visual inspection, the temporal plots highlight increased variation in the log of the signal magnitude of brain regions at 7T as a function of echo number, implying an increase in sensitivity to underling signal effects, and a subsequent deviation from mono-exponential decay. Values for the signal at time zero (S_0), relaxation time (T_2^*) and covariance metrics for the signal magnitude decay are summarised in Table 1. As expected, the initial signal magnitude at 7T is larger than at 3T and the T_2^* relaxation time decreases with an increase in field strength. Furthermore, we find T_2^* values to vary more at 7T than at 3T (CoV of 0.23 versus 0.37), suggesting an enhanced sensitivity to underlying field perturbations.

Table 1
Results of fitting the signal magnitude using a single compartment mono-exponential model. Shown are the signal magnitude at time zero (S_0), the relaxation time (T_2*) for both the 3T and 7T data. As

expected, the use of 7T leads to higher signal and lower relaxation times than 3T. 7T also leads to higher levels of variability in relaxation times as indicated by the CoV values.

Regions	S_0 (a.u.)		T_2^* (ms)	
	3T	7T	3T	7T
Corpus callosum	389	643	37	22
Putamen	372	552	36	23
CSF	295	551	62	45
Average/*CoV*	352	582	*0.23*	*0.37*

3.3.2 *Frequency shifts as a function of echo time*

Fig. 3 depicts frequency shift curves obtained at 3T and 7T for the three regions investigated. The solid line in each plot corresponds to the mean frequency shift after averaging voxel values in each region and across participants. The shaded area matched in colour with the solid line shows the standard deviation computed across subjects. Qualitative observations in variations due to field strength can be deduced from each plot, whilst quantitative differences are elucdiated by signal compartment parameters listed in the corresponding tables.

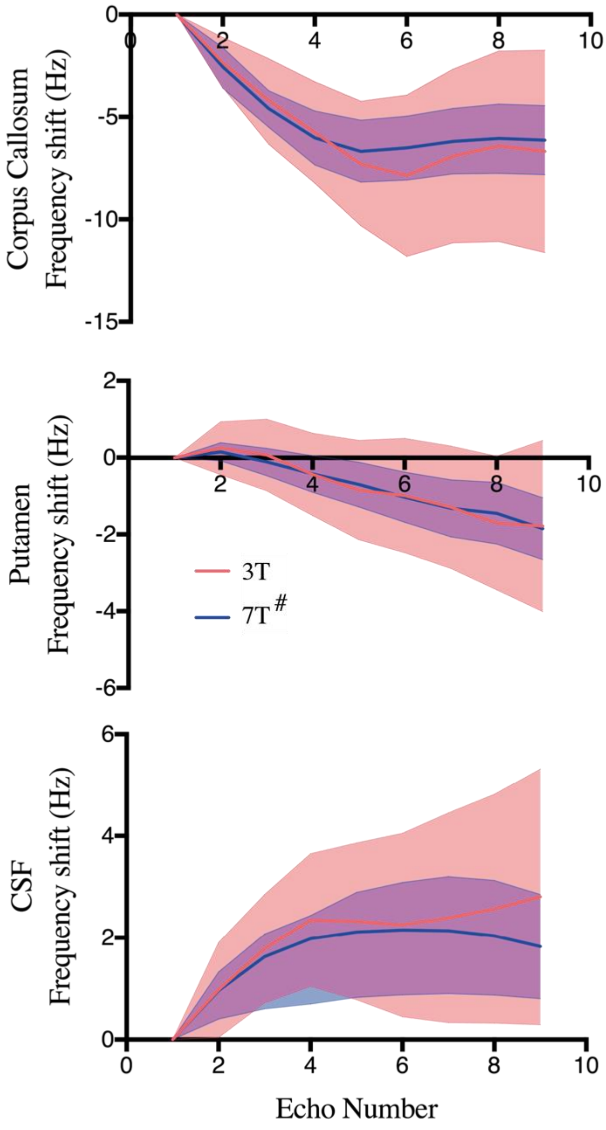

$\Delta f^{\#}_{7T}$ (Hz)	**-7.9**	**-2.6**	**10.1**	
Δf_{3T} (Hz)	**-9.5**	**-1.3**	**15.4**	SER
$VF^{\#}_{7T}$	34%	26%	40%	24.0
VF_{3T}	45%	31%	24%	19.5

$\Delta f^{\#}_{7T}$ (Hz)	**-6.0**	**5.1**	**5.5**	
Δf_{3T} (Hz)	**-3.6**	**1.7**	**4.9**	SER
$VF^{\#}_{7T}$	34%	33%	33%	8.4
VF_{3T}	36%	30%	34%	9.8

$\Delta f^{\#}_{7T}$ (Hz)	**-13.2**	**2.0**	
Δf_{3T} (Hz)	**-12.3**	**2.5**	SER
$VF^{\#}_{7T}$	26%	74%	9.8
VF_{3T}	22%	78%	11.3

Fig. 3. Frequency shift values at 3T and 7T plotted as a function of echo number for the three regions investigated. The mean (solid line) and standard deviation (corresponding shaded area) across the six participants are shown. Frequency shifts from 7T measurements were scaled to 3T values (a multiplication by 3/7), and are labelled $7T^{\#}$, to allow for direct comparison of temporal trends. Signal compartment frequency shifts and their respective volume fractions are provided in the tables corresponding to each region. The SER of complex signal fit was calculated for both 3T and 7T measurements.

Temporal variations in the 3T and 7T frequency shifts exhibit consistent trends within each ROI; in other words, the shape of the mean frequency shift curves appear similar between 3T and 7T measurements (refer to plots in Fig. 3). For example, frequency shifts in the corpus callosum trend in an exponentially decaying manner, while the putamen decays in a more linear fashion, and the CSF appears to increase logarithmically (refer to plots in Fig. 3). However, the trends in 7T measurements appear less temporally variable. For example, the 3T result in the corpus callosum and CSF exhibit a small oscillation after the fifth echo, whereas the 7T result is relatively smooth at all echo times.

Upon general inspection, variability at each echo number appears larger at 3T than at 7T. Table 2 summarises this observation quantitatively through the area spanned by the error bars over echo time. To generate this table the distance between the positive and negative error bars at each echo number was calculated and summed over echo numbers. In essence, this metric measures the change in the level of variation in the data (e.g. across participants) between 3T and 7T. Irrespective of the method, variability at 3T is always larger and by moving to 7T the inter-subject variability can approximately be halved.

Table 2
Measure of variability across participants. Areas spanned by variations in Fig. 3 plots, calculated by taking the difference between the upper and lower error bounds at each echo number and by summing over echo numbers. The areas reduce with increasing field strength, suggesting that inter-subject variability can be mitigated through field strength increases.

Regions	3T (Hz)	7T (Hz)
Corpus callosum	331	190
Putamen	162	87
CSF	211	95

3.3.3 *Explaining temporal frequency shifts using GRE-MRI signal compartments*

The tables beside each of the plots in Fig. 3 show the frequency shifts obtained by fitting a multi-compartment signal model. Model parameters were obtained using the 3T and 7T GRE-MRI data, and frequency shifts are presented alongside the normalized SER (nSER). The overall quality-of-fit, for both 3T and 7T trends, is the best for the putamen (9.8 and 8.4, respectively), then followed by the CSF (11.3 and 9.8), and corpus callosum (19.5 and 24.0). Furthermore, the nSER values for 3T and 7T fit are the closest to each other within the putamen (9.8 and 8.4; a difference of 1.4), then followed by the CSF (11.3 and 9.8; a difference of 1.5), and finally by the corpus callosum (19.5 and 24.0; a difference of 4.5). Expectedly, similarities in nSER values seem to correspond broadly to qualitative trends between 3T and 7T frequency shift curves. For example, when observing the plots in Fig. 3, the putamen exhibits the most similarity between 3T and 7T trends (featuring the lowest difference in nSER), whereas the corpus callosum, albeit arguably, exhibits the least coherence between 3T and 7T trends (featuring the highest difference in nSER). Additionally, a better quality-of-fit (indicated by a lower nSER) can be observed in the 7T data for the putamen and CSF (compare 3T and 7T nSER values within putamen and CSF in Fig. 3). In the corpus callosum, however, the 3T data exhibits a better quality-of-fit in comparison to 7T (compare 3T and 7T nSER within corpus callosum in Fig. 3). The signal compartments are arranged in the table by matching the $7T^{\#}$ frequency shifts to the closest corresponding 3T frequency shift; in doing so, respective compartment volume fractions within the putamen and CSF correspond well between 3T and 7T data (compare volume fractions in Fig. 3 tables for putamen and CSF). For example, in the CSF, the signal compartment with the highest volume fraction (~75%) at both 3T and $7T^{\#}$ exhibit frequency shifts within a close range (2.5Hz and 2.0Hz); the smaller volume fraction compartment (~25%) also correspond well (-12.3Hz and -13.2Hz). A similar, well-suited correspondence is also exhibited by the compartment frequency shifts and their respective volume fractions within the putamen. In the corpus callosum, the three compartment frequency shifts identified correspond to similar values between at 3T and 7T; however, their respective volume fractions do not correspond between the field strengths (Fig. 3).

3.4 Discussion

We studied echo time dependence of the GRE-MRI complex signal acquired at 3T and 7T in three human brain regions (corpus callosum, CSF, and putamen). Qualitatively, three primary effects were observed. First, temporal trends in signal magnitude and frequency shift as a function of echo time varied across brain regions studied. Second, non-linear trends in temporal frequency shift evolution were observed in both 3T and 7T measurements. Third, frequency shifts computed from 7T susceptibility data were less variable (for all regions investigated) across the participant cohort than those obtained using 3T data. Additionally, we found the signal compartments and their respective quality-of-fit measures to broadly reflect similar underlying influences in both 3T and 7T data.

The reduced inter-cohort variability for echo time trends in frequency shifts at 7T can be attributed to a higher SNR present at higher field strength measurements (Dumoulin et al., 2017; Duyn, 2017, 2012; Duyn et al., 2007; Zwanenburg et al., 2011). This in turn would yield improved sensitivity to underlying field effects arising from tissue microstructure, and would explain the deviations from mono-exponential decay in the temporal signal magnitude (van Gelderen et al., 2012). It is interesting to note that the broad shape of temporal frequency shift curves, at 3T and 7T, remain consistent within each ROI; however, subtle inter-field-strength differences do exist (refer to plots in Fig. 3). We speculate that the GRE-MRI signal exhibits a similar sensitivity to macroscopic (≥ 1 mm), voxel-scale field effects at both 3T and 7T. However, 7T measurements may be differentially sensitive to sub-voxel influences at the meso-macroscopic interface (0.5—1.0mm); this would engender gross similarities in the curve shape, but also result in subtle variations in field dependent temporal trends.

A favourable correspondence between the quality-of-fit for respective multi-compartment models and qualitative signal trends comes as no surprise. For example, the difference in SER values between the 3T and 7T fit is lower for the putamen when compared to the corpus callosum; correspondingly, mean frequency shift curves for the putamen are more coincident in comparison to the corpus callosum. When fitting to the same signal model, similar signal trends should yield similar fitting errors. When observing the SER measures within specific regions, we find improved fitting in 7T data when compared to 3T in the putamen and CSF; the opposite was observed in the corpus callosum. The putamen and

CSF are often characterized as isotropic in their biomolecular distribution (Purves et al., 1997; Sakka et al., 2011). Diffusion tensor imaging studies validate these observations by reporting fractional anisotropy (FA) values in these regions at ≤0.1, and within a range of 0.2—0.7 in white matter regions, such as the corpus callosum (Alexander et al., 2007); FA values fall with a range of 0 and 1, wherein values close to 0 indicate low anisotropy and those close to 1 exhibit high anisotropy (Huisman, 2010). Furthermore, recent studies demonstrate a strong influence of fibre orientation and susceptibility anisotropy within the corpus callosum, especially at higher field strengths, on GRE-MRI signal phase measurements (Alonso-Ortiz et al., 2017; Lee et al., 2017; W. Li et al., 2012; van Gelderen et al., 2012; Wharton and Bowtell, 2012; Yablonskiy and Sukstanskii, 2017). The anisotropic properties of tissue orientation and magnetic susceptibility have been shown to induce a broad range of shifts in the Larmor (Lee et al., 2010b; Wharton and Bowtell, 2012, 2013); thus, the frequency shift signature for an individual component of tissue microstructure could be interspersed across a range of frequency shifts due to anisotropic effects. Consequently, the effects of both tissue and susceptibility anisotropy would prove more difficult to explain as discrete signal compartments and yield higher fitting errors in 7T data when compared to 3T. This phenomenon could also explain a lack of coherence between the volume fractions assigned to the respective frequency shifts in 3T and 7T compartments within the corpus callosum (refer to tables in Fig. 3). In more isotropic medium (e.g. putamen and CSF), however, we observe a close correspondence between the individual frequency shifts and their respective volume fractions resolved at 3T and 7T (refer to tables in Fig. 3). Thus, comparing GRE-MRI signal compartments computed from 3T and 7T data would appear to be more robust when considering regions characterized by a more isotropic tissue microstructure (e.g. gray matter regions).

The multi-echo GRE-MRI signal was compartmentalized with the primary aim of generating a quantitative platform for comparing temporal signal evolution acquired at 3T and 7T. A detailed contextualization of the signal compartments, as they relate to tissue microstructure and underlying biophysical origins, has already been discussed (Section 2.4 Discussion).

3.5 Conclusions

We investigated the influence of the static magnetic field strength on temporal variations in the multi-echo GRE-MRI signal. Using 3T and 7T GRE-MRI data, we compared temporal trends in the signal magnitude and frequency shift as a function of echo time, and compartmentalized the GRE-MRI complex signal to identify quantitative differences in the temporal signal at different field strengths. Our results demonstrate (1) the persistence of non-linear variations in echo-time dependent frequency shifts at both 3T and 7T (exhibiting similar profiles at both field strengths), (2) a lower inter-participant variability in temporal frequency shifts in the 7T signal, when compared to 3T, and (3) a close correspondence of GRE-MRI signal compartment parameters, resolved at 3T and 7T, in areas of relative isotropic tissue composition (e.g. putamen and CSF) when compared to regions of high anisotropy (e.g. corpus callosum).

Chapter 4: Conclusion

4.1 Considerations for signal compartmentalization studies

The unique signal properties in MRI used to inform tissue properties are well established. Furthermore, the utility of tailored signal models to maximize the information gained from these unique signal properties is also prevalent (e.g. diffusion tensor imaging, myelin water fraction imaging, functional MRI, and dynamic contrast enhanced MRI). Regardless of the advances in hardware technology, image pre-processing techniques, and post-processing layers, multi-compartment signal modelling can be used to extract additional features from mGRE-MRI data. For example, we utilize the temporal GRE-MRI signal acquired at the highest available field strength for human imaging (7T), optimize signal pre-processing (e.g. selective channel combination and phase offset correction), and implement the latest post-processing techniques (e.g. background field removal and susceptibility estimation) to maximize the quantitative and visual information gained. However, there remains a large gap in characterizing and quantifying tissue information at the micro-scale. The utility of signal compartments lies herein.

4.2 Developing susceptibility-based signal compartments as a biomarker for tissue properties

Due to the simple formulation of the plane wave model utilized in our study, any tissue property which affects either the GRE-MRI signal magnitude or phase could be characterized using signal compartments which take this form. The immediate utility of susceptibility-based signal compartments would be used to quantify the micro-scale constituents, and characterize the spatial arrangement, in various tissues of interest. Within the context of structural neuroimaging, one use case would be to quantify tissue components that would influence the local magnetic field distribution, such as biometals (e.g. non-heme iron, manganese, copper, and zinc), de-oxyhemoglobin, and structured macromolecules (e.g.

lipids—myelin, proteins—neurofilaments, and carbohydrates—glucose) (Chen et al., 2013; Duyn et al., 2007; Duyn and Schenck, 2017; He and Yablonskiy, 2009; Schweser et al., 2011a). These moieties could be quantified in physiological (development and ageing) and pathological conditions (e.g. myelin integrity in multiple sclerosis, cell density characterization in glioblastoma, amyloid-beta quantification in Alzheimer's disease, etc.). Previous studies demonstrate the effect of fiber orientation on the measured GRE-MRI signal, both in the spatial (Liu, 2010; Wharton and Bowtell, 2012; Yablonskiy and Sukstanskii, 2017) and temporal (Lee et al., 2017; Nam et al., 2015; Sukstanskii and Yablonskiy, 2014) domains. Thus, compartmentalizing the GRE-MRI signal in data acquired using different orientations and analysing the changes in the compartment frequency shift would allow for quantitative estimation of underlying fiber orientation. This application could be systematically applied alongside diffusion tensor imaging to better characterize white matter structure, or to remove the confounds of fiber orientation when aiming to quantify myelin water fraction or any other underlying tissue susceptibility influence (e.g. iron and all other biometals). The benefits of signal compartmentalization should not be regarded as a supplantive tool, rather as a supplementary one, wherein additional information is gained towards characterization of underlying tissue properties or a convergent clinical diagnosis.

4.3 Final comments and future directions

Further benefits from GRE-MRI signal compartmentalization could be derived through the development of more informative biophysical models, robust parameter estimation algorithms, advances in scanner technology, and diversification of the applied domains. A recent study, for example, extends the traditional (Maxwellian) signal model to tease apart the effects of susceptibility anisotropy, on a cellular level, arising from myelin layering (Sukstanskii and Yablonskiy, 2014). This modification, however, notably increases model complexity in formulating the myelin signal compartment as a quadratic exponential as opposed to the traditional linear exponential. This work, alongside ours, further exemplifies the need for more sophisticated optimization algorithms to cope with evolving model complexity. For example, implementing global optimization methods (e.g differential evolution, particle swarm, CMAES, etc.) may improve the accuracy of parameter estimation (Zhigljavsky and Žilinskas, 2007) in comparison to the traditional deterministic approaches utilized for signal compartmentalization (Chen et al., 2013; Li et al., 2015; Nam et al., 2015). Another recent study by Alonso-Ortiz et al. (2017), reports the additional utility of including complex-valued GRE signal information to be gained at higher field strengths (7T vs. 3T). These results, akin to our findings in Ch. 3, demonstrate the benefits derived from improvements in magnet technology. In conclusion, our study is one of the first to systematically demonstrate the utility of GRE-MRI compartments outside of the context of MWF imaging. Further implementations to image and characterize tissue properties in this manner will precipitate additional improvements and applications for GRE-MRI signal compartments. We invite future research to tackle the aforementioned issues and extend our findings to develop imaging biomarkers, sensitive to microscale changes, by way of mGRE-MRI signal compartmentalization.

Appendix

Table 1

Parameter estimates for three different initialization values.

	A (a.u.)	T_2^* (ms)	Δf (Hz)
Initial value 1	$\frac{\lvert S(TE_1)\rvert}{N}$	30	0
Initial value 2	$\frac{\lvert S(TE_1)\rvert}{N}$	10	-10
Initial value 3	$\frac{\lvert S(TE_1)\rvert}{N}$	50	10

Parameters for AIC-selected models from initial values 1:

	A_1	ΔF_1 (Hz)	A_2	ΔF_2 (Hz)	A_3	ΔF_3 (Hz)
IC	71%	**-11.0**	22%	**-24.1**	7%	**17.6**
CC	37%	**1.0**	32%	**8.1**	31%	**-31.5**
Fornix	86%	**-5.9**	14%	**6.6**		
Insula	52%	**-8.4**	48%	**4.7**		
Thalamus	51%	**3.5**	49%	**-1.0**		
CSF	87%	**3.6**	13%	**16.1**		
Caudate	56%	**9.7**	25%	**22.1**	19%	**-26.8**
SN	36%	**3.4**	33%	**17.5**	32%	**7.2**
Putamen	48%	**3.9**	27%	**15.6**	25%	**29.5**

Parameters for AIC-selected models from initial values 2:

A_1	ΔF_1 (Hz)	A_2	ΔF_2 (Hz)	A_3	ΔF_3 (Hz)
71%	**-11.0**	22%	**-24.1**	7%	**17.6**
34%	**1.0**	34%	**8.1**	32%	**-31.6**
86%	**-5.9**	14%	**6.6**		
52%	**-8.4**	48%	**4.7**		
50%	**3.5**	50%	**-1.0**		
87%	**3.6**	13%	**16.1**		
56%	**9.7**	25%	**22.1**	19%	**-26.9**
44%	**2.9**	30%	**17.3**	24%	**7.1**
48%	**3.9**	27%	**15.6**	25%	**29.5**

Parameters for AIC-selected models from initial values 3:

A_1	ΔF_1 (Hz)	A_2	ΔF_2 (Hz)	A_3	ΔF_3 (Hz)
71%	**-11.0**	22%	**-24.1**	7%	**17.6**
34%	**1.0**	34%	**8.2**	32%	**-31.7**
83%	**-6.0**	17%	**6.1**		
52%	**-8.4**	48%	**4.7**		
50%	**3.5**	50%	**-1.0**		
87%	**3.6**	13%	**16.1**		
56%	**9.7**	25%	**22.1**	19%	**-26.9**
49%	**4.0**	30%	**17.3**	21%	**7.1**
48%	**3.9**	27%	**15.6**	25%	**29.5**

Table 2

Summary of tissue-based signal influences considered in explaining signal compartments.

Influence on measured signal			**Sample**	**Field strength of measurement**	**Region**	**Susceptibility (χ)**	**Δf at 7T**	**Remarks**	**Study**
Tissue susceptibility	Tissue Iron	Non-heme iron	In-vivo, human	3T	Frontal cortical WM Medial GM	0.041 ± 0.010ppm 0.066 ± 0.011ppm	12.22 ± 2.98Hz 19.67 ± 3.28Hz	Myelin corrected susceptibility values attributed to tissue iron. 0.0127 ppm *100 g/mg*cm3/gr*[Fe] (Hallgren and Sourander, 1960) Susceptibility calculated via Krylov-subspace solver (LSQR) with spherical constraints.	Schweser et al., 2011
			In-vivo, human	3T	GM (frontal lobe)	4.40 x 10^{-3} ppm (CGS)	16.48Hz (SI)	Susceptibility calculated using generalized Lorentzian approach (converted from CGS to SI)[a]	He and Yablonskiy, 2009
					WM (frontal lobe)	4.40 x 10^{-3} ppm (CGS)	16.48Hz (SI)		
					CSF (frontal lobe)	0.33 x 10^{-3}ppm (CGS)	1.12Hz (SI)		
			In-vitro (cell fractions), rat	Precision NMR	Cortex	f(molecular concentration, tissue density)	f(molecular concentration, tissue density)	Regression: -1.209 ppb/(mg/ml)	Leutritz et al., 2016
	Lipids	Myelin	In-vivo, rat	7T	Corpus Callosum	-0.089ppm	-26.52Hz	Susceptibility calculated using generalized Lorentzian approach.	Lee et al., 2012
		Other	In-vivo, human	3T	GM (frontal lobe)	2.37 x 10^{-3} ppm	8.88Hz	See description[a].	He and Yablonskiy, 2009
					WM (frontal lobe)	5.52 x 10^{-3} ppm	20.67Hz		
					CSF (frontal lobe)	0	0		
	Proteins	Non-specific	In-vivo, human	3T	GM (frontal lobe)	-4.17 x 10^{-3} ppm	-15.62Hz	See description[a].	He and Yablonskiy, 2009
					WM (frontal lobe)	-4.56 x 10^{-3} ppm	-17.08Hz		

					CSF (frontal lobe)	-0.0016×10^{-3} ppm	-0.006Hz		
		Synaptosomes	In-vitro (cell fractions), rat	Precision NMR	Cortex	f(molecular concentration, tissue density)	f(molecular concentration, tissue density)	0.368 ppb/(mg/ml)	Leutritz et al., 2016
	De-oxyhemoglobin		In-vivo, human	3T	GM (frontal lobe)	0.90×10^{-3} ppm	3.37Hz	See description[a].	He and Yablonskiy, 2009
					WM (frontal lobe)	0.21×10^{-3} ppm	0.79Hz		
					CSF (frontal lobe)	0	0		
			In-vitro, NMR	3T	Human blood	0.27 ± 0.03ppm	80.47 ± 8.94Hz	Susceptibility measured using SQUID magnetometer and analytically adjusted with signal modelling techniques.	Spees et al., 2001
Tissue properties	Relaxation of distinct water pools	Myelin water	In-vivo, human	7T	OR (⊥)	N/A	25Hz	Three compartment modelling of GRE-MRI complex signal.	Sati et al., 2013
					SCC (⊥)	N/A	31.8Hz		
					OR (||)	N/A	-5.4Hz		
					SCC (⊥)	N/A	25.8Hz		Li et al., 2015
					OR (⊥)	N/A	22.5Hz		
		Axonal water	In-vivo, human	7T	OR (⊥)	N/A	-6.0Hz		Sati et al., 2013
					SCC (⊥)	N/A	-4.1Hz		
					OR (||)	N/A	-2.5Hz		
					SCC (⊥)	N/A	-6.3Hz		Li et al., 2015
					OR (⊥)	N/A	-6.5Hz		
		Extra-cellular Water	In-vivo, human	7T	OR (⊥)	N/A	1.5Hz		Sati et al., 2013
					SCC (⊥)	N/A	2.0Hz		
					OR (||)	N/A	1.1Hz		
					SCC (⊥)	N/A	0		Li et al., 2015
					OR (⊥)	N/A	0		
	Fiber orientation/ Susceptibility anisotropy (sign negligible_		In-vivo, human + Simulations	7T	Sub-cortical WM	0.016ppm	4.76Hz	Implementation of hollow cylinder model in white matter.	Wharton and Bowtell, 2012
			In-vitro + Simulations	7T	Corpus Callosum	0.012ppm	3.58Hz	Difference between perpendicular and parallel fiber orientations using simulations.	Lee et al., 2010b

---

			In-vivo, human	7T	Sub-cortical WM & GM	0.004 - 0.029ppm	1.19 to 8.64Hz	Difference between perpendicular and parallel ROI-based susceptibility values.	Li et al., 2012a
			In-vivo, human	3T	Sub-cortical WM	0.019 ppm	5.67Hz		Li et al., 2012b
Chemical exchange	Non-specific protons		In-vivo, human	7T	Sub-cortical WM	0.010ppm	2.98Hz	Implementation of hollow cylinder model.	Wharton and Bowtell, 2012
			In-vivo, human	14T	GM	N/A	6.99Hz		Shmueli et al., 2011
					WM	N/A	11.03Hz		
			In-vivo	7T	GM & WM	0.010ppm	3Hz	Difference between GM and WM. Regression: 0.040 ppm/mM of BSA.	Zhong et al., 2008
		Myelin	In-vitro (cell fractions), rat	Precision NMR	Cortex	f(molecular concentration, tissue density)	f(molecular concentration, tissue density)	Regression: 1.283 ppb/(mg/ml)	Leutritz et al., 2016
		Synaptosomes				f(molecular concentration, tissue density)	f(molecular concentration, tissue density)	Regression: 0.775 ppb/(mg/ml)	
Diffusion	Fast Regime		Simulation		f(mesoscopic susceptibility arrangement, compartment volume fraction, and compartment packing)	N/A	N/A	Need to consider spin population interaction statistics.	Ruh et al., 2017

Ethics approval

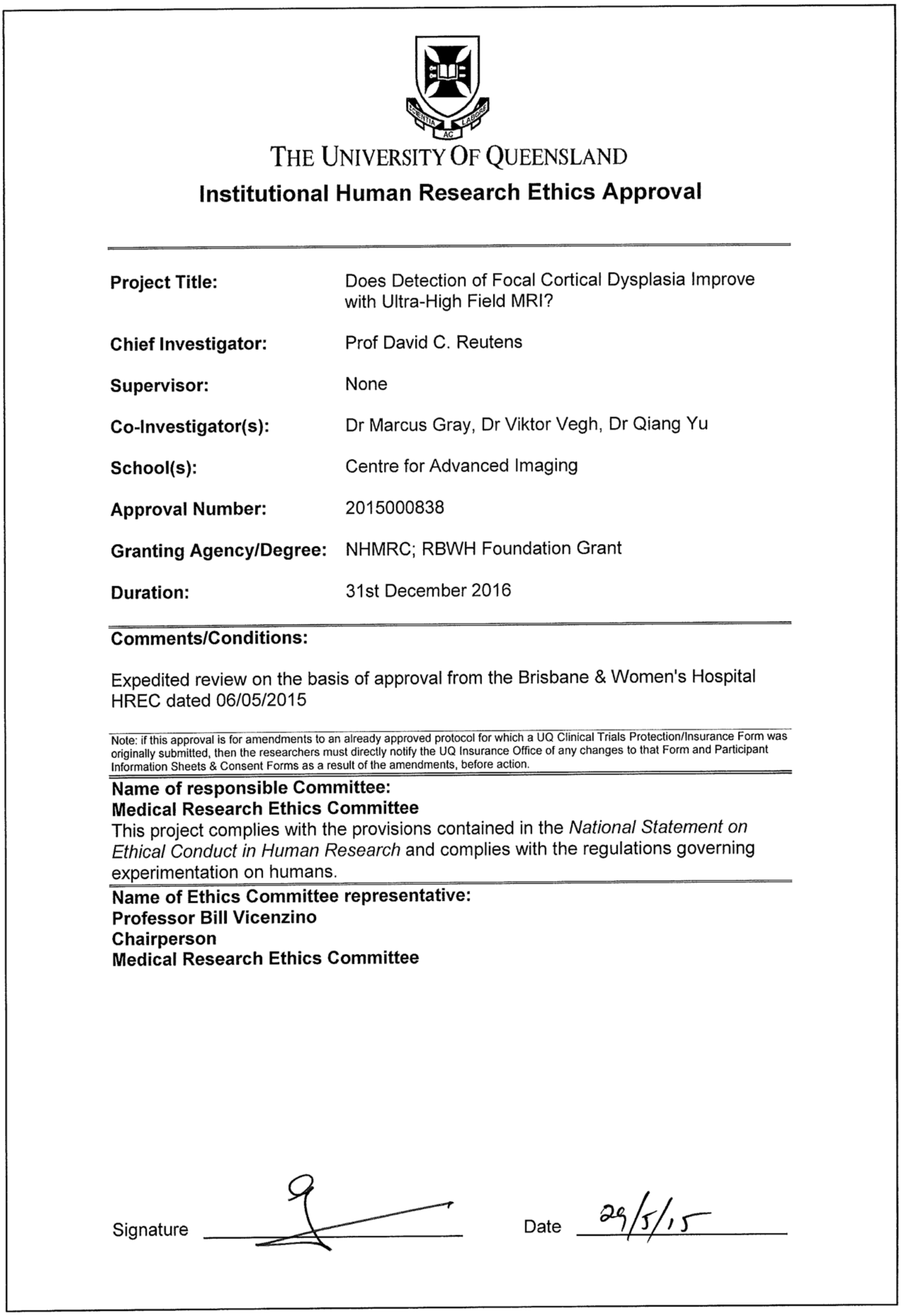

THE UNIVERSITY OF QUEENSLAND

Institutional Human Research Ethics Approval

Project Title: Does Detection of Focal Cortical Dysplasia Improve with Ultra-High Field MRI?

Chief Investigator: Prof David C. Reutens

Supervisor: None

Co-Investigator(s): Dr Marcus Gray, Dr Viktor Vegh, Dr Qiang Yu

School(s): Centre for Advanced Imaging

Approval Number: 2015000838

Granting Agency/Degree: NHMRC; RBWH Foundation Grant

Duration: 31st December 2016

Comments/Conditions:

Expedited review on the basis of approval from the Brisbane & Women's Hospital HREC dated 06/05/2015

Note: if this approval is for amendments to an already approved protocol for which a UQ Clinical Trials Protection/Insurance Form was originally submitted, then the researchers must directly notify the UQ Insurance Office of any changes to that Form and Participant Information Sheets & Consent Forms as a result of the amendments, before action.

Name of responsible Committee:
Medical Research Ethics Committee
This project complies with the provisions contained in the *National Statement on Ethical Conduct in Human Research* and complies with the regulations governing experimentation on humans.

Name of Ethics Committee representative:
Professor Bill Vicenzino
Chairperson
Medical Research Ethics Committee

Signature

Date 29/5/15

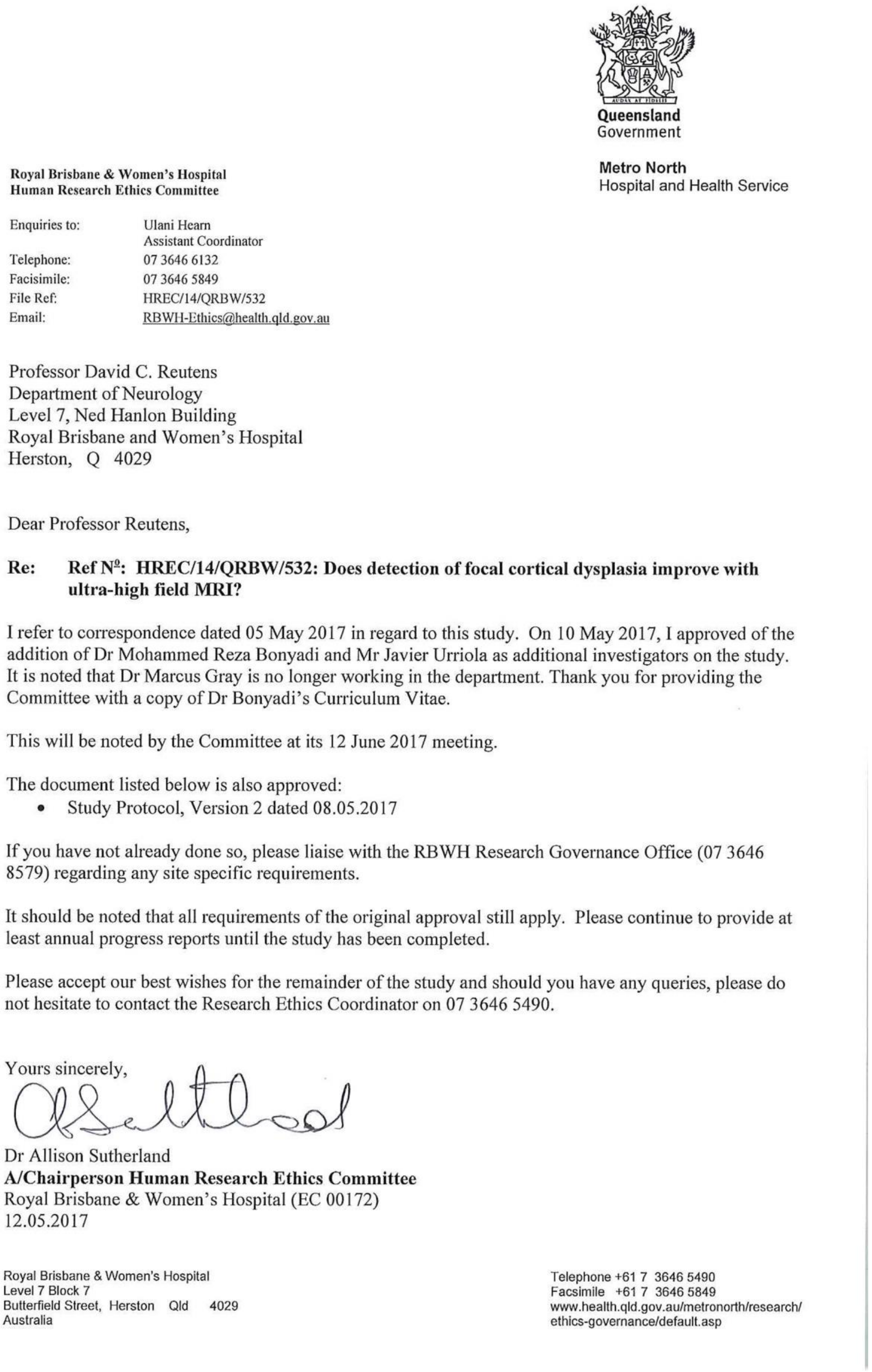

Queensland
Government

Metro North
Hospital and Health Service

Royal Brisbane & Women's Hospital
Human Research Ethics Committee

Enquiries to:	Ulani Hearn Assistant Coordinator
Telephone:	07 3646 6132
Facisimile:	07 3646 5849
File Ref:	HREC/14/QRBW/532
Email:	RBWH-Ethics@health.qld.gov.au

Professor David C. Reutens
Department of Neurology
Level 7, Ned Hanlon Building
Royal Brisbane and Women's Hospital
Herston, Q 4029

Dear Professor Reutens,

Re: Ref Nº: HREC/14/QRBW/532: Does detection of focal cortical dysplasia improve with ultra-high field MRI?

I refer to correspondence dated 05 May 2017 in regard to this study. On 10 May 2017, I approved of the addition of Dr Mohammed Reza Bonyadi and Mr Javier Urriola as additional investigators on the study. It is noted that Dr Marcus Gray is no longer working in the department. Thank you for providing the Committee with a copy of Dr Bonyadi's Curriculum Vitae.

This will be noted by the Committee at its 12 June 2017 meeting.

The document listed below is also approved:

- Study Protocol, Version 2 dated 08.05.2017

If you have not already done so, please liaise with the RBWH Research Governance Office (07 3646 8579) regarding any site specific requirements.

It should be noted that all requirements of the original approval still apply. Please continue to provide at least annual progress reports until the study has been completed.

Please accept our best wishes for the remainder of the study and should you have any queries, please do not hesitate to contact the Research Ethics Coordinator on 07 3646 5490.

Yours sincerely,

Dr Allison Sutherland
A/Chairperson Human Research Ethics Committee
Royal Brisbane & Women's Hospital (EC 00172)
12.05.2017

Royal Brisbane & Women's Hospital
Level 7 Block 7
Butterfield Street, Herston Qld 4029
Australia

Telephone +61 7 3646 5490
Facsimile +61 7 3646 5849
www.health.qld.gov.au/metronorth/research/ethics-governance/default.asp

References

Abduljalil, A.M., Schmalbrock, P., Novak, V., Chakeres, D.W., 2003. Enhanced gray and white matter contrast of phase susceptibility-weighted images in ultra-high-field magnetic resonance imaging. J. Magn. Reson. Imaging 18, 284–290. https://doi.org/10.1002/jmri.10362

Abragam, A., 1961. The Principles of Nuclear Magnetism. Clarendon Press.

Akaike, H., 2011. Akaike's information criterion, in: International Encyclopedia of Statistical Science. Springer, pp. 25–25.

Alexander, A.L., Lee, J.E., Lazar, M., Field, A.S., 2007. Diffusion Tensor Imaging of the Brain. Neurother. J. Am. Soc. Exp. Neurother. 4, 316–329. https://doi.org/10.1016/j.nurt.2007.05.011

Alonso-Ortiz, E., Levesque, I.R., Pike, G.B., 2017. Impact of magnetic susceptibility anisotropy at 3 T and 7 T on T2*-based myelin water fraction imaging. NeuroImage. https://doi.org/10.1016/j.neuroimage.2017.09.040

Aoki, S., Okada, Y., Nishimura, K., Barkovich, A.J., Kjos, B.O., Brasch, R.C., Norman, D., 1989. Normal deposition of brain iron in childhood and adolescence: MR imaging at 1.5 T. Radiology 172, 381–385. https://doi.org/10.1148/radiology.172.2.2748819

Aquino, D., Bizzi, A., Grisoli, M., Garavaglia, B., Bruzzone, M.G., Nardocci, N., Savoiardo, M., Chiapparini, L., 2009. Age-related Iron Deposition in the Basal Ganglia: Quantitative Analysis in Healthy Subjects. Radiology 252, 165–172. https://doi.org/10.1148/radiol.2522081399

Argyridis, I., Li, W., Johnson, G.A., Liu, C., 2014. Quantitative magnetic susceptibility of the developing mouse brain reveals microstructural changes in the white matter. NeuroImage 88, 134–142. https://doi.org/10.1016/j.neuroimage.2013.11.026

Arthur, D., Vassilvitskii, S., 2007. k-means++: The advantages of careful seeding, in: Proceedings of the Eighteenth Annual ACM-SIAM Symposium on Discrete Algorithms. Society for Industrial and Applied Mathematics, pp. 1027–1035.

Baxan, N., Harsan, L.A., Dragonu, I., Merkle, A., Hennig, J., von Elverfeldt, D., 2010. Myelin as a primary source of phase contrast demonstrated in vivo in the mouse brain, in: Proc., ISMRM, 19th Annual Meeting and Exhibition, Stockholm, Sweden. p. 3016.

Bedrick, E.J., Tsai, C.-L., 1994. Model Selection for Multivariate Regression in Small Samples. Biometrics 50, 226. https://doi.org/10.2307/2533213

Bilgic, B., Pfefferbaum, A., Rohlfing, T., Sullivan, E.V., Adalsteinsson, E., 2012. MRI estimates of brain iron concentration in normal aging using quantitative susceptibility mapping. NeuroImage 59, 2625–2635. https://doi.org/10.1016/j.neuroimage.2011.08.077

Bloch, F., 1957. Generalized Theory of Relaxation. Phys. Rev. 105, 1206–1222. https://doi.org/10.1103/PhysRev.105.1206

Bloch, F., 1946a. Nuclear Induction. Phys. Rev. 70, 460–474. https://doi.org/10.1103/PhysRev.70.460

Bloch, F., 1946b. Nuclear Induction. Phys. Rev. 70, 460–474. https://doi.org/10.1103/PhysRev.70.460

Bollmann, S., Zimmer, F., O'Brien, F., Vegh, V., Barth, M., 2015. When to perform channel combination in 7 Tesla quantitative susceptibility mapping?, in: Organization of the Human Brain Mapping.

Bourekas, E.C., Christoforidis, G.A., Abduljalil, A.M., Kangarlu, A., Chakeres, D.W., Spigos, D.G., Robitaille, P.M., 1999. High resolution MRI of the deep gray nuclei at 8 Tesla. J. Comput. Assist. Tomogr. 23, 867–874.

Burnham, K.P., Anderson, D.R., 2004. Multimodel Inference: Understanding AIC and BIC in Model Selection. Sociol. Methods Res. 33, 261–304. https://doi.org/10.1177/0049124104268644

Chen, W.C., Foxley, S., Miller, K.L., 2013. Detecting microstructural properties of white matter based on compartmentalization of magnetic susceptibility. NeuroImage 70, 1–9. https://doi.org/10.1016/j.neuroimage.2012.12.032

Cho, Z.-H., Oh, S.-H., Kim, J.-M., Park, S.-Y., Kwon, D.-H., Jeong, H.-J., Kim, Y.-B., Chi, J.-G., Park, C.-W., Huston, J., Lee, K.H., Jeon, B.S., 2011. Direct visualization of Parkinson's disease by in vivo human brain imaging using 7.0T magnetic resonance imaging. Mov. Disord. Off. J. Mov. Disord. Soc. 26, 713–718. https://doi.org/10.1002/mds.23465

Chu, S.C., Xu, Y., Balschi, J.A., Springer, C.S., 1990. Bulk magnetic susceptibility shifts in NMR studies of compartmentalized samples: use of paramagnetic reagents. Magn. Reson. Med. 13, 239–262.

Cronin, M.J., Wang, N., Decker, K.S., Wei, H., Zhu, W.-Z., Liu, C., 2017. Exploring the origins of echo-time-dependent quantitative susceptibility mapping (QSM) measurements in healthy tissue and cerebral microbleeds. NeuroImage 149, 98–113. https://doi.org/10.1016/j.neuroimage.2017.01.053

Dale, A.M., Fischl, B., Sereno, M.I., 1999. Cortical Surface-Based Analysis: I. Segmentation and Surface Reconstruction. NeuroImage 9, 179–194. https://doi.org/10.1006/nimg.1998.0395

Damadian, R., 1971. Tumor detection by nuclear magnetic resonance.

Deistung, A., Rauscher, A., Sedlacik, J., Stadler, J., Witoszynskyj, S., Reichenbach, J.R., 2008. Susceptibility weighted imaging at ultra high magnetic field strengths: Theoretical considerations and experimental results. Magn. Reson. Med. 60, 1155–1168. https://doi.org/10.1002/mrm.21754

Deistung, A., Schäfer, A., Schweser, F., Biedermann, U., Turner, R., Reichenbach, J.R., 2013. Toward in vivo histology: A comparison of quantitative susceptibility mapping (QSM) with magnitude-, phase-, and R2∗-imaging at ultra-high magnetic field strength. NeuroImage 65, 299–314. https://doi.org/10.1016/j.neuroimage.2012.09.055

Drayer, B., Burger, P., Darwin, R., Riederer, S., Herfkens, R., Johnson, G., 1986. MRI of brain iron. Am. J. Roentgenol. 147, 103–110. https://doi.org/10.2214/ajr.147.1.103

Driscoll, R.L., Bender, P.L., 1958. Proton Gyromagnetic Ratio. Phys. Rev. Lett. 1, 413–414. https://doi.org/10.1103/PhysRevLett.1.413

Du, Y.P., Chu, R., Hwang, D., Brown, M.S., Kleinschmidt-DeMasters, B.K., Singel, D., Simon, J.H., 2007. Fast multislice mapping of the myelin water fraction using multicompartment analysis ofT2* decay at 3T: A preliminary postmortem study. Magn. Reson. Med. 58, 865–870. https://doi.org/10.1002/mrm.21409

Dumoulin, S.O., Fracasso, A., van der Zwaag, W., Siero, J.C.W., Petridou, N., 2017. Ultra-high field MRI: Advancing systems neuroscience towards mesoscopic human brain function. NeuroImage. https://doi.org/10.1016/j.neuroimage.2017.01.028

Duyn, J.H., 2017. Studying brain microstructure with magnetic susceptibility contrast at high-field. NeuroImage. https://doi.org/10.1016/j.neuroimage.2017.02.046

Duyn, J.H., 2012. The future of ultra-high field MRI and fMRI for study of the human brain. NeuroImage 62, 1241–1248. https://doi.org/10.1016/j.neuroimage.2011.10.065

Duyn, J.H., Schenck, J., 2017. Contributions to magnetic susceptibility of brain tissue. NMR Biomed. 30, n/a-n/a. https://doi.org/10.1002/nbm.3546

Duyn, J.H., van Gelderen, P., Li, T.-Q., de Zwart, J.A., Koretsky, A.P., Fukunaga, M., 2007. High-field MRI of brain cortical substructure based on signal phase. Proc. Natl. Acad. Sci. 104, 11796–11801.

Ertöz, L., Steinbach, M., Kumar, V., 2003. Finding clusters of different sizes, shapes, and densities in noisy, high dimensional data, in: Proceedings of the 2003 SIAM International Conference on Data Mining. SIAM, pp. 47–58.

Fukunaga, M., Li, T.-Q., Gelderen, P. van, Zwart, J.A. de, Shmueli, K., Yao, B., Lee, J., Maric, D., Aronova, M.A., Zhang, G., Leapman, R.D., Schenck, J.F., Merkle, H., Duyn, J.H., 2010. Layer-specific variation of iron content in cerebral cortex as a source of MRI contrast. Proc. Natl. Acad. Sci. 107, 3834–3839. https://doi.org/10.1073/pnas.0911177107

Goldman, M., 2001. Formal Theory of Spin–Lattice Relaxation. J. Magn. Reson. 149, 160–187. https://doi.org/10.1006/jmre.2000.2239

Haacke, E.M., Ayaz, M., Khan, A., Manova, E.S., Krishnamurthy, B., Gollapalli, L., Ciulla, C., Kim, I., Petersen, F., Kirsch, W., 2007. Establishing a baseline phase behavior in magnetic resonance imaging to determine normal vs. abnormal iron content in the brain. J. Magn. Reson. Imaging 26, 256–264. https://doi.org/10.1002/jmri.22987

Haacke, E.M., Cheng, N.Y.C., House, M.J., Liu, Q., Neelavalli, J., Ogg, R.J., Khan, A., Ayaz, M., Kirsch, W., Obenaus, A., 2005. Imaging iron stores in the brain using magnetic resonance imaging. Magn. Reson. Imaging 23, 1–25. https://doi.org/10.1016/j.mri.2004.10.001

Haacke, E.M., Liu, S., Buch, S., Zheng, W., Wu, D., Ye, Y., 2015a. Quantitative susceptibility mapping: current status and future directions. Magn. Reson. Imaging 33, 1–25. https://doi.org/10.1016/j.mri.2014.09.004

Haacke, E.M., Liu, S., Buch, S., Zheng, W., Wu, D., Ye, Y., 2015b. Quantitative susceptibility mapping: current status and future directions. Magn. Reson. Imaging 33, 1–25.

Hagberg, G.E., Welch, E.B., Greiser, A., 2010. The sign convention for phase values on different vendor systems: definition and implications for susceptibility-weighted imaging. Magn. Reson. Imaging 28, 297–300.

Hahn, E.L., 1950. Nuclear Induction Due to Free Larmor Precession. Phys. Rev. 77, 297–298. https://doi.org/10.1103/PhysRev.77.297.2

Hahn, E.L., Abragam, A., 1992. Pulsed Magnetic Resonance: NMR, ESR, and Optics : a Recognition of E.L. Hahn. Clarendon Press.

Hallgren, B., Sourander, P., 1958. The Effect of Age on the Non-Haemin Iron in the Human Brain. J. Neurochem. 3, 41–51. https://doi.org/10.1111/j.1471-4159.1958.tb12607.x

Hammond, K.E., Lupo, J.M., Xu, D., Metcalf, M., Kelley, D.A.C., Pelletier, D., Chang, S.M., Mukherjee, P., Vigneron, D.B., Nelson, S.J., 2008. Development of a robust method for generating 7.0 T multichannel phase images of the brain with application to normal volunteers and patients with neurological diseases. NeuroImage 39, 1682–1692. https://doi.org/10.1016/j.neuroimage.2007.10.037

Harrison, P.M., Arosio, P., 1996. The ferritins: molecular properties, iron storage function and cellular regulation. Biochim. Biophys. Acta BBA - Bioenerg. 1275, 161–203. https://doi.org/10.1016/0005-2728(96)00022-9

He, X., Yablonskiy, D.A., 2009. Biophysical mechanisms of phase contrast in gradient echo MRI. Proc. Natl. Acad. Sci. 106, 13558–13563.

He, X., Yablonskiy, D.A., 2007. Quantitative BOLD: Mapping of Human Cerebral Deoxygenated Blood Volume and Oxygen Extraction Fraction: Default State. Magn. Reson. Med. Off. J. Soc. Magn. Reson. Med. Soc. Magn. Reson. Med. 57, 115–126. https://doi.org/10.1002/mrm.21108

Hernando, D., Haldar, J.P., Sutton, B.P., Ma, J., Kellman, P., Liang, Z.-P., 2008. Joint estimation of water/fat images and field inhomogeneity map. Magn. Reson. Med. 59, 571–580. https://doi.org/10.1002/mrm.21522

Hill, H.D.W., Richards, R.E., 1968. Limits of measurement in magnetic resonance. J. Phys. [E] 1, 977. https://doi.org/10.1088/0022-3735/1/10/202

Hong, F.T., Mauzerall, D., Mauro, A., 1971. Magnetic Anisotropy and the Orientation of Retinal Rods in a Homogeneous Magnetic Field. Proc. Natl. Acad. Sci. U. S. A. 68, 1283–1285.

Hopkins, J.A., Wehrli, F.W., 1997. Magnetic susceptibility measurement of insoluble solids by NMR: Magnetic susceptibility of bone. Magn. Reson. Med. 37, 494–500.

Huisman, T.A.G.M., 2010. Diffusion-weighted and diffusion tensor imaging of the brain, made easy. Cancer Imaging 10, S163–S171. https://doi.org/10.1102/1470-7330.2010.9023

Hurvich, C.M., Tsai, C.-L., 1989. Regression and time series model selection in small samples. Biometrika 76, 297–307.

Hwang, D., Kim, D.-H., Du, Y.P., 2010. In vivo multi-slice mapping of myelin water content using T2* decay. NeuroImage 52, 198–204. https://doi.org/10.1016/j.neuroimage.2010.04.023

Kaufman, L., Rousseeuw, P.J., 2009. Finding groups in data: an introduction to cluster analysis. John Wiley & Sons.

Ke, Y., Qian, Z.M., 2007. Brain iron metabolism: neurobiology and neurochemistry. Prog. Neurobiol. 83, 149–173. https://doi.org/10.1016/j.pneurobio.2007.07.009

Kee, Y., Liu, Z., Zhou, L., Dimov, A., Cho, J., Rochefort, L. de, Seo, J.K., Wang, Y., 2017. Quantitative Susceptibility Mapping (QSM) Algorithms: Mathematical Rationale and Computational Implementations. IEEE Trans. Biomed. Eng. PP, 1–1. https://doi.org/10.1109/TBME.2017.2749298

Khalil, M., Riedlbauer, B., Langkammer, C., Enzinger, C., Ropele, S., Stojakovic, T., Scharnagl, H., Culea, V., Petzold, A., Teunissen, C.E., others, 2014. Cerebrospinal fluid transferrin levels are reduced in patients with early multiple sclerosis. Mult. Scler. J. 20, 1569–1577.

Kim, H.-G., Park, S., Rhee, H.Y., Lee, K.M., Ryu, C.-W., Rhee, S.J., Lee, S.Y., Wang, Y., Jahng, G.-H., 2017. Quantitative susceptibility mapping to evaluate the early stage of Alzheimer’s disease. NeuroImage Clin. 16, 429–438. https://doi.org/10.1016/j.nicl.2017.08.019

Koenig, S.H., 1991. Cholesterol of myelin is the determinant of gray-white contrast in MRI of brain. Magn. Reson. Med. 20, 285–291. https://doi.org/10.1002/mrm.1910200210

Kozlowski, P., Liu, J., Yung, A.C., Tetzlaff, W., 2008. High-resolution myelin water measurements in rat spinal cord. Magn. Reson. Med. 59, 796–802. https://doi.org/10.1002/mrm.21527

Kubo, A., Spaniol, T.P., Terao, T., 1998. The Effect of Bulk Magnetic Susceptibility on Solid State NMR Spectra of Paramagnetic Compounds. J. Magn. Reson. 133, 330–340. https://doi.org/10.1006/jmre.1998.1473

Lancaster, J.L., Andrews, T., Hardies, L.J., Dodd, S., Fox, P.T., 2003. Three-pool model of white matter. J. Magn. Reson. Imaging 17, 1–10. https://doi.org/10.1002/jmri.10230

Langkammer, C., Krebs, N., Goessler, W., Scheurer, E., Yen, K., Fazekas, F., Ropele, S., 2012. Susceptibility induced gray–white matter MRI contrast in the human brain. NeuroImage 59, 1413–1419. https://doi.org/10.1016/j.neuroimage.2011.08.045

Laule, C., Kozlowski, P., Leung, E., Li, D.K.B., MacKay, A.L., Moore, G.R.W., 2008. Myelin water imaging of multiple sclerosis at 7 T: Correlations with histopathology. NeuroImage 40, 1575–1580. https://doi.org/10.1016/j.neuroimage.2007.12.008

Lauterbur, P.C., 1973. Image Formation by Induced Local Interactions: Examples Employing Nuclear Magnetic Resonance. Nature 242, 190–191. https://doi.org/10.1038/242190a0

Lee, J., Hirano, Y., Fukunaga, M., Silva, A.C., Duyn, J.H., 2010a. On the contribution of deoxy-hemoglobin to MRI gray–white matter phase contrast at high field. NeuroImage 49, 193–198. https://doi.org/10.1016/j.neuroimage.2009.07.017

Lee, J., Nam, Y., Choi, J.Y., Kim, E.Y., Oh, S.-H., Kim, D.-H., 2017. Mechanisms of T2* anisotropy and gradient echo myelin water imaging. NMR Biomed. 30, n/a-n/a. https://doi.org/10.1002/nbm.3513

Lee, J., Shmueli, K., Fukunaga, M., Gelderen, P. van, Merkle, H., Silva, A.C., Duyn, J.H., 2010b. Sensitivity of MRI resonance frequency to the orientation of brain tissue microstructure. Proc. Natl. Acad. Sci. 107, 5130–5135. https://doi.org/10.1073/pnas.0910222107

Lee, J., Shmueli, K., Kang, B.-T., Yao, B., Fukunaga, M., van Gelderen, P., Palumbo, S., Bosetti, F., Silva, A.C., Duyn, J.H., 2012. The contribution of myelin to magnetic susceptibility-weighted contrasts in high-field MRI of the brain. NeuroImage 59, 3967–3975. https://doi.org/10.1016/j.neuroimage.2011.10.076

Leutritz, T., Hilfert, L., Smalla, K.-H., Speck, O., Zhong, K., 2013. Accurate quantification of water-macromolecule exchange induced frequency shift: Effects of reference substance. Magn. Reson. Med. 69, 263–268. https://doi.org/10.1002/mrm.24223

Levitt, M.H., 2001. Spin Dynamics: Basics of Nuclear Magnetic Resonance. John Wiley & Sons.

Li, T.-Q., van Gelderen, P., Merkle, H., Talagala, L., Koretsky, A.P., Duyn, J., 2006. Extensive heterogeneity in white matter intensity in high-resolution T2*-weighted MRI of the human brain at 7.0 T. NeuroImage 32, 1032–1040. https://doi.org/10.1016/j.neuroimage.2006.05.053

Li, W., Avram, A.V., Wu, B., Xiao, X., Liu, C., 2014. Integrated Laplacian-based phase unwrapping and background phase removal for quantitative susceptibility mapping: HARPERELLA PHASE PROCESSING. NMR Biomed. 27, 219–227. https://doi.org/10.1002/nbm.3056

Li, W., Wu, B., Avram, A.V., Liu, C., 2012. Magnetic susceptibility anisotropy of human brain in vivo and its molecular underpinnings. NeuroImage 59, 2088–2097. https://doi.org/10.1016/j.neuroimage.2011.10.038

Li, W., Wu, B., Liu, C., 2011. Quantitative susceptibility mapping of human brain reflects spatial variation in tissue composition. NeuroImage 55, 1645–1656. https://doi.org/10.1016/j.neuroimage.2010.11.088

Li, X., van Gelderen, P., Sati, P., de Zwart, J.A., Reich, D.S., Duyn, J.H., 2015. Detection of demyelination in multiple sclerosis by analysis of T2* relaxation at 7T. NeuroImage Clin. 7, 709–714. https://doi.org/10.1016/j.nicl.2015.02.021

Li, X., Vikram, D.S., Lim, I.A.L., Jones, C.K., Farrell, J.A.D., van Zijl, P.C.M., 2012. Mapping magnetic susceptibility anisotropies of white matter in vivo in the human brain at 7T. NeuroImage 62, 314–330. https://doi.org/10.1016/j.neuroimage.2012.04.042

Lipton, M.L., 2010. Totally accessible MRI: a user's guide to principles, technology, and applications. Springer Science & Business Media.

Liu, C., 2010. Susceptibility tensor imaging. Magn. Reson. Med. 63, 1471–1477. https://doi.org/10.1002/mrm.22482

Liu, C., Li, W., Johnson, G.A., Wu, B., 2011. High-field (9.4T) MRI of brain dysmyelination by quantitative mapping of magnetic susceptibility. NeuroImage 56, 930–938. https://doi.org/10.1016/j.neuroimage.2011.02.024

Liu, C., Li, W., Tong, K.A., Yeom, K.W., Kuzminski, S., 2015. Susceptibility-weighted imaging and quantitative susceptibility mapping in the brain: Brain Susceptibility

Imaging and Mapping. J. Magn. Reson. Imaging 42, 23–41. https://doi.org/10.1002/jmri.24768

Liu, T., Khalidov, I., de Rochefort, L., Spincemaille, P., Liu, J., Tsiouris, A.J., Wang, Y., 2011. A novel background field removal method for MRI using projection onto dipole fields (PDF). NMR Biomed. 24, 1129–1136. https://doi.org/10.1002/nbm.1670

Liu, T., Spincemaille, P., de Rochefort, L., Kressler, B., Wang, Y., 2009. Calculation of susceptibility through multiple orientation sampling (COSMOS): A method for conditioning the inverse problem from measured magnetic field map to susceptibility source image in MRI. Magn. Reson. Med. 61, 196–204. https://doi.org/10.1002/mrm.21828

Lloyd, S., 1982. Least squares quantization in PCM. IEEE Trans. Inf. Theory 28, 129–137. https://doi.org/10.1109/TIT.1982.1056489

Lodge, S.O., 1897. The influence of a magnetic field on radiation frequency. Harrison and Sons.

Lodygensky, G.A., Marques, J.P., Maddage, R., Perroud, E., Sizonenko, S.V., Hüppi, P.S., Gruetter, R., 2012. In vivo assessment of myelination by phase imaging at high magnetic field. NeuroImage 59, 1979–1987. https://doi.org/10.1016/j.neuroimage.2011.09.057

Luo, J., He, X., d'Avignon, D.A., Ackerman, J.J.H., Yablonskiy, D.A., 2010. Protein-induced water 1H MR frequency shifts: Contributions from magnetic susceptibility and exchange effects. J. Magn. Reson. 202, 102–108. https://doi.org/10.1016/j.jmr.2009.10.005

Luo, J., He, X., Yablonskiy, D.A., 2014. Magnetic Susceptibility Induced White Matter MR Signal Frequency Shifts - Experimental Comparison between Lorentzian Sphere and Generalized Lorentzian Approaches. Magn. Reson. Med. Off. J. Soc. Magn. Reson. Med. Soc. Magn. Reson. Med. 71, 1251–1263. https://doi.org/10.1002/mrm.24762

Mackay, A., Whittall, K., Adler, J., Li, D., Paty, D., Graeb, D., 1994. In vivo visualization of myelin water in brain by magnetic resonance. Magn. Reson. Med. 31, 673–677. https://doi.org/10.1002/mrm.1910310614

Mangrum, W., Christianson, K., Duncan, S., Hoang, P., Song, A., Merkle, E., 2012. Duke Review of MRI Principles. 304. Mosby Phila. PA 304.

Markl, M., Leupold, J., 2012. Gradient echo imaging. J. Magn. Reson. Imaging 35, 1274–1289. https://doi.org/10.1002/jmri.23638

Marques, J. p., Bowtell, R., 2005. Application of a Fourier-based method for rapid calculation of field inhomogeneity due to spatial variation of magnetic susceptibility. Concepts Magn. Reson. Part B Magn. Reson. Eng. 25B, 65–78. https://doi.org/10.1002/cmr.b.20034

Marques, J.P., Maddage, R., Mlynarik, V., Gruetter, R., 2009. On the origin of the MR image phase contrast: An in vivo MR microscopy study of the rat brain at 14.1 T. NeuroImage 46, 345–352. https://doi.org/10.1016/j.neuroimage.2009.02.023

McAuliffe, M.J., Lalonde, F.M., McGarry, D., Gandler, W., Csaky, K., Trus, B.L., 2001. Medical Image Processing, Analysis and Visualization in clinical research, in: 14th IEEE Symposium on Computer-Based Medical Systems, 2001. CBMS 2001. Proceedings. Presented at the 14th IEEE Symposium on Computer-Based Medical Systems, 2001. CBMS 2001. Proceedings, pp. 381–386. https://doi.org/10.1109/CBMS.2001.941749

Menon, R.S., Rusinko, M.S., Allen, P.S., 1992. Proton Relaxation Studies of Water Compartmentalization in a Model Neurological System. Magn. Reson. Med. 28, 264–274. https://doi.org/10.1002/mrm.1910280208

Miyajima, M., Arai, H., 2015. Evaluation of the Production and Absorption of Cerebrospinal Fluid. Neurol. Med. Chir. (Tokyo) 55, 647–656. https://doi.org/10.2176/nmc.ra.2015-0003

Moore, G.R.W., Leung, E., MacKay, A.L., Vavasour, I.M., Whittall, K.P., Cover, K.S., Li, D.K.B., Hashimoto, S.A., Oger, J., Sprinkle, T.J., Paty, D.W., 2000. A pathology-MRI study of the short-T2 component in formalin-fixed multiple sclerosis brain. Neurology 55, 1506–1510. https://doi.org/10.1212/WNL.55.10.1506

Morell, P., Quarles, R.H., 1999. Characteristic Composition of Myelin.

Naik, P.A., Shi, P., Tsai, C.-L., 2007. Extending the Akaike Information Criterion to Mixture Regression Models. J. Am. Stat. Assoc. 102, 244–254. https://doi.org/10.1198/016214506000000861

Nam, Y., Lee, J., Hwang, D., Kim, D.-H., 2015. Improved estimation of myelin water fraction using complex model fitting. NeuroImage 116, 214–221. https://doi.org/10.1016/j.neuroimage.2015.03.081

O’Brien, J.S., Sampson, E.L., 1965. Lipid composition of the normal human brain: gray matter, white matter, and myelin. J. Lipid Res. 6, 537–544.

Ogawa, S., Lee, T.M., Kay, A.R., Tank, D.W., 1990. Brain magnetic resonance imaging with contrast dependent on blood oxygenation. Proc. Natl. Acad. Sci. U. S. A. 87, 9868–9872.

Peddada, S.D., Haseman, J.K., 2006. Analysis of Nonlinear Regression Models: A Cautionary Note. Dose-Response 3, 342–352. https://doi.org/10.2203/dose-response.003.03.005

Peters, A.M., Brookes, M.J., Hoogenraad, F.G., Gowland, P.A., Francis, S.T., Morris, P.G., Bowtell, R., 2007. T2* measurements in human brain at 1.5, 3 and 7 T. Magn. Reson. Imaging 25, 748–753. https://doi.org/10.1016/j.mri.2007.02.014

Poole, C.P.J., 2012. Relaxation in Magnetic Resonance: Dielectric and Mossbauer Applications. Elsevier.

Purves, D.E., Augustine, G.J., Fitzpatrick, D.E., Katz, L.C., others, 1997. Neuroscience.

Qian, Z.M., Shen, X., 2001. Brain iron transport and neurodegeneration. Trends Mol. Med. 7, 103–108.

Rabi, I.I., 1937. Space Quantization in a Gyrating Magnetic Field. Phys. Rev. 51, 652–654. https://doi.org/10.1103/PhysRev.51.652

Rabi, I.I., Kellogg, J.M.B., Zacharias, J.R., 1934. The Magnetic Moment of the Deuton. Phys. Rev. 46, 163–165. https://doi.org/10.1103/PhysRev.46.163

Reichenbach, J.R., 2012. The future of susceptibility contrast for assessment of anatomy and function. NeuroImage 62, 1311–1315. https://doi.org/10.1016/j.neuroimage.2012.01.004

Reichenbach, J.R., Schweser, F., Serres, B., Deistung, A., 2015. Quantitative Susceptibility Mapping: Concepts and Applications. Clin. Neuroradiol. 25, 225–230. https://doi.org/10.1007/s00062-015-0432-9

Reichenbach, J.R., Venkatesan, R., Yablonskiy, D.A., Thompson, M.R., Lai, S., Haacke, E.M., 1997. Theory and application of static field inhomogeneity effects in gradient-echo imaging. J. Magn. Reson. Imaging 7, 266–279.

Rosenblatt, C., Yager, P., Schoen, P.E., 1987. Orientation of lipid tubules by a magnetic field. Biophys. J. 52, 295–301. https://doi.org/10.1016/S0006-3495(87)83216-2

Ruckstuhl, A., 2010. Introduction to Nonlinear Regression.

Ruh, A., Scherer, H., Kiselev, V.G., 2017. The larmor frequency shift in magnetically heterogeneous media depends on their mesoscopic structure. Magn. Reson. Med. n/a-n/a. https://doi.org/10.1002/mrm.26753

Saher, G., Brügger, B., Lappe-Siefke, C., Möbius, W., Tozawa, R., Wehr, M.C., Wieland, F., Ishibashi, S., Nave, K.-A., 2005. High cholesterol level is essential for myelin membrane growth. Nat. Neurosci. https://doi.org/10.1038/nn1426

Sakka, L., Coll, G., Chazal, J., 2011. Anatomy and physiology of cerebrospinal fluid. Eur. Ann. Otorhinolaryngol. Head Neck Dis. 128, 309–316. https://doi.org/10.1016/j.anorl.2011.03.002

Sati, P., van Gelderen, P., Silva, A.C., Reich, D.S., Merkle, H., de Zwart, J.A., Duyn, J.H., 2013. Micro-compartment specific T2⁎ relaxation in the brain. NeuroImage 77, 268–278. https://doi.org/10.1016/j.neuroimage.2013.03.005

Schenck, J.F., Zimmerman, E.A., 2004. High-field magnetic resonance imaging of brain iron: birth of a biomarker? NMR Biomed. 17, 433–445. https://doi.org/10.1002/nbm.922

Schweser, Deistung, A., Gullmar, D., Atterbury, M., Lehr, B.W., Sommer, K., Reichenbach, J.R., 2011a. Non-linear evolution of GRE phase as a means to investigate tissue microstructure. Proc. 19th Int. Soc. Magn. Reson. Med. 4527.

Schweser, Deistung, A., Lehr, B.W., Reichenbach, J.R., 2011b. Quantitative imaging of intrinsic magnetic tissue properties using MRI signal phase: An approach to in vivo brain iron metabolism? NeuroImage 54, 2789–2807. https://doi.org/10.1016/j.neuroimage.2010.10.070

Schweser, F., Deistung, A., Reichenbach, J.R., 2016. Foundations of MRI phase imaging and processing for Quantitative Susceptibility Mapping (QSM). Z. Für Med. Phys. 26, 6–34. https://doi.org/10.1016/j.zemedi.2015.10.002

Schweser, F., Sommer, K., Deistung, A., Reichenbach, J.R., 2012. Quantitative susceptibility mapping for investigating subtle susceptibility variations in the human brain. NeuroImage 62, 2083–2100. https://doi.org/10.1016/j.neuroimage.2012.05.067

Sherman, S.M., 2016. Thalamus plays a central role in ongoing cortical functioning. Nat. Neurosci. 19, 533–541. https://doi.org/10.1038/nn.4269

Shmueli, K., de Zwart, J.A., van Gelderen, P., Li, T.-Q., Dodd, S.J., Duyn, J.H., 2009. Magnetic susceptibility mapping of brain tissue in vivo using MRI phase data. Magn. Reson. Med. 62, 1510–1522. https://doi.org/10.1002/mrm.22135

Shmueli, K., Dodd, S.J., Li, T.-Q., Duyn, J.H., 2011. The contribution of chemical exchange to MRI frequency shifts in brain tissue: Exchange-Induced Frequency Shifts in Brain Tissue. Magn. Reson. Med. 65, 35–43. https://doi.org/10.1002/mrm.22604

Shmueli, K., Dodd, S.J., van Gelderen, P., Duyn, J.H., 2017. Investigating lipids as a source of chemical exchange-induced MRI frequency shifts. NMR Biomed. 30, n/a-n/a. https://doi.org/10.1002/nbm.3525

Slichter, C.P., 2013. Principles of Magnetic Resonance. Springer Science & Business Media.

Smith, S.M., 2002. Fast robust automated brain extraction. Hum. Brain Mapp. 17, 143–155. https://doi.org/10.1002/hbm.10062

Snipes, M., Taylor, D.C., 2014. Model selection and Akaike Information Criteria: An example from wine ratings and prices. Wine Econ. Policy 3, 3–9. https://doi.org/10.1016/j.wep.2014.03.001

Sood, S., Urriola, J., Reutens, D., O’Brien, K., Bollmann, S., Barth, M., Vegh, V., 2017a. Echo time-dependent quantitative susceptibility mapping contains information on tissue properties. Magn. Reson. Med. 77, 1946–1958. https://doi.org/10.1002/mrm.26281

Sood, S., Urriola, J., Reutens, D., O’Brien, K., Bollmann, S., Barth, M., Vegh, V., 2017b. Echo time-dependent quantitative susceptibility mapping contains information on tissue properties. Magn. Reson. Med. 77, 1946–1958. https://doi.org/10.1002/mrm.26281

Spiess, A.-N., Neumeyer, N., 2010. Research article An evaluation of R2 as an inadequate measure for nonlinear models in pharmacological and biochemical research: a Monte Carlo approach.

Stewart, W.A., Mackay, A.L., Whittall, K.P., Moore, G.R.W., Paty, D.W., 1993. Spin-spin relaxation in experimental allergic Encephalomyelitis. Analysis of CPMG data using a non-linear least squares method and linear inverse theory. Magn. Reson. Med. 29, 767–775. https://doi.org/10.1002/mrm.1910290608

Straub, S., Schneider, T.M., Emmerich, J., Freitag, M.T., Ziener, C.H., Schlemmer, H.-P., Ladd, M.E., Laun, F.B., 2017. Suitable reference tissues for quantitative susceptibility mapping of the brain: Reference Tissues for QSM of the Brain. Magn. Reson. Med. 78, 204–214. https://doi.org/10.1002/mrm.26369

Sukstanskii, A.L., Yablonskiy, D.A., 2014. On the role of neuronal magnetic susceptibility and structure symmetry on gradient echo MR signal formation. Magn. Reson. Med. 71, 345–353. https://doi.org/10.1002/mrm.24629

Sun, H., Wilman, A.H., 2014. Background field removal using spherical mean value filtering and Tikhonov regularization. Magn. Reson. Med. 71, 1151–1157. https://doi.org/10.1002/mrm.24765

Szczepaniak, L.S., Dobbins, R.L., Stein, D.T., McGarry, J.D., 2002a. Bulk magnetic susceptibility effects on the assessment of intra- and extramyocellular lipids in vivo. Magn. Reson. Med. 47, 607–610. https://doi.org/10.1002/mrm.10086

Szczepaniak, L.S., Dobbins, R.L., Stein, D.T., McGarry, J.D., 2002b. Bulk magnetic susceptibility effects on the assessment of intra- and extramyocellular lipids in vivo. Magn. Reson. Med. 47, 607–610. https://doi.org/10.1002/mrm.10086

Taiwo, F.A., 2003. Electron paramagnetic resonance spectroscopic studies of iron and copper proteins. J. Spectrosc. 17, 53–63.

Todorich, B., Pasquini, J.M., Garcia, C.I., Paez, P.M., Connor, J.R., 2009. Oligodendrocytes and myelination: The role of iron. Glia 57, 467–478. https://doi.org/10.1002/glia.20784

van Gelderen, P., de Zwart, J.A., Lee, J., Sati, P., Reich, D.S., Duyn, J.H., 2012. Nonexponential T2* decay in white matter. Magn. Reson. Med. 67, 110–117. https://doi.org/10.1002/mrm.22990

van Zijl, P.C.M., Lam, W.W., Xu, J., Knutsson, L., Stanisz, G.J., 2017. Magnetization Transfer Contrast and Chemical Exchange Saturation Transfer MRI. Features and analysis of the field-dependent saturation spectrum. NeuroImage. https://doi.org/10.1016/j.neuroimage.2017.04.045

Vandekerckhove, J., Matzke, D., Wagenmakers, E.-J., 2014. Model comparison and the principle of parsimony.

Vegh, V., O'Brien, K., Barth, M., Reutens, D.C., 2016. Selective channel combination of MRI signal phase. Magn. Reson. Med. 76, 1469–1477. https://doi.org/10.1002/mrm.26057

Wachowicz, K., Snyder, R.E., 2002. Assignment of the T2 components of amphibian peripheral nerve to their microanatomical compartments. Magn. Reson. Med. 47, 239–245. https://doi.org/10.1002/mrm.10053

Wang, Y., Liu, T., 2015. Quantitative susceptibility mapping (QSM): Decoding MRI data for a tissue magnetic biomarker: QSM. Magn. Reson. Med. 73, 82–101. https://doi.org/10.1002/mrm.25358

Webb, S., Munro, C.A., Midha, R., Stanisz, G.J., 2003. Is multicomponent T2 a good measure of myelin content in peripheral nerve? Magn. Reson. Med. 49, 638–645. https://doi.org/10.1002/mrm.10411

Wharton, S., Bowtell, R., 2013. Gradient echo based fiber orientation mapping using R2* and frequency difference measurements. NeuroImage 83, 1011–1023. https://doi.org/10.1016/j.neuroimage.2013.07.054

Wharton, S., Bowtell, R., 2012. Fiber orientation-dependent white matter contrast in gradient echo MRI. Proc. Natl. Acad. Sci. 109, 18559–18564. https://doi.org/10.1073/pnas.1211075109

White, R.M., 2013. Quantum Theory of Magnetism: Magnetic Properties of Materials. Springer Science & Business Media.

Whittall, K.P., MacKay, A.L., 1989. Quantitative interpretation of NMR relaxation data. J. Magn. Reson. 1969 84, 134–152. https://doi.org/10.1016/0022-2364(89)90011-5

Wu, B., Li, W., Avram, A.V., Gho, S.-M., Liu, C., 2012. Fast and Tissue-Optimized Mapping of Magnetic Susceptibility and T2* with Multi-Echo and Multi-Shot Spirals. NeuroImage 59, 297–305. https://doi.org/10.1016/j.neuroimage.2011.07.019

Wu, Z., He, H., Sun, Y., Du, Y., Zhong, J., 2017. High resolution myelin water imaging incorporating local tissue susceptibility analysis. Magn. Reson. Imaging 42, 107–113. https://doi.org/10.1016/j.mri.2017.06.005

Xu, T., Foxley, S., Kleinnijenhuis, M., Chen, W.C., Miller, K.L., 2017. The effect of realistic geometries on the susceptibility-weighted MR signal in white matter. Magn. Reson. Med.

Xu, T., Foxley, S., Miller, K., 2015. Oligodendrocytes and the role of iron in magnetic susceptibility driven frequency shifts in white matter, in: Proceedings of the 23rd Annual Meeting of ISMRM, Toronto, Ontario, Canada.

Yablonskiy, D.A., Haacke, E.M., 1994. Theory of NMR signal behavior in magnetically inhomogeneous tissues: The static dephasing regime. Magn. Reson. Med. 32, 749–763. https://doi.org/10.1002/mrm.1910320610

Yablonskiy, D.A., Luo, J., Sukstanskii, A.L., Iyer, A., Cross, A.H., 2012. Biophysical mechanisms of MRI signal frequency contrast in multiple sclerosis. Proc. Natl. Acad. Sci. 109, 14212–14217. https://doi.org/10.1073/pnas.1206037109

Yablonskiy, D.A., Sukstanskii, A.L., 2017. Effects of biological tissue structural anisotropy and anisotropy of magnetic susceptibility on the gradient echo MRI signal phase: theoretical background: **Anisotropy of Magnetic Susceptibility**. NMR Biomed. 30, e3655. https://doi.org/10.1002/nbm.3655

Yuan, A., Rao, M.V., Veeranna, Nixon, R.A., 2012. Neurofilaments at a glance. J. Cell Sci. 125, 3257–3263. https://doi.org/10.1242/jcs.104729

Zecca, L., Youdim, M.B.H., Riederer, P., Connor, J.R., Crichton, R.R., 2004. Iron, brain ageing and neurodegenerative disorders. Nat. Rev. Neurosci. 5, 863–873. https://doi.org/10.1038/nrn1537

Zhong, K., Leupold, J., von Elverfeldt, D., Speck, O., 2008. The molecular basis for gray and white matter contrast in phase imaging. NeuroImage 40, 1561–1566. https://doi.org/10.1016/j.neuroimage.2008.01.061

Zwanenburg, J.J.M., Versluis, M.J., Luijten, P.R., Petridou, N., 2011. Fast high resolution whole brain T2* weighted imaging using echo planar imaging at 7T. NeuroImage 56, 1902–1907. https://doi.org/10.1016/j.neuroimage.2011.03.046